

Copyright

by

Charles Naim Baroud

2001

The Dissertation Committee for Charles Naim Baroud
Certifies that this is the approved version of the following Dissertation:

**Transitions from three- to two-dimensional turbulence
in a rotating system**

Committee:

Harry L. Swinney (Co-Supervisor)

Raul G. Longoria (Co-Supervisor)

Kenneth S. Ball

Joseph J. Beaman, Jr

David G. Bogard

**Transitions from three- to two-dimensional turbulence
in a rotating system**

by

Charles Naim Baroud, S.B., M.S.M.E.

Dissertation

Presented to the Faculty of the Graduate School of

The University of Texas at Austin

in Partial Fulfillment

of the Requirements

for the Degree of

Doctor of Philosophy

The University of Texas at Austin

December 2001

To the wind which carries with it
the jets and vortices above Fouwar.

Acknowledgments

Six years at the Center for Nonlinear Dynamics is a long time. During these years many people have crossed my path and taught me and contributed to this work. Those include administrators, post-docs, students, and even professors. They deserve many thanks for the exciting and fruitful times.

In particular, some made direct contributions to the experiment. Eric Weeks taught me which switches to switch. Eschel Faraggi helped with the hot-film probes. Jérôme Paret helped with the early stages of the PIV, Benoit-Joseph Gréa helped with the later stages. Jori Rupert-Felsot worked on the lighting system. Jason Wang wrote some of data acquisition code, and Mario Ragwitz introduced new data analysis techniques. Mainly however, Brendan Plapp, took most of the hot-film data used here and worked with me for three years.

Some people had a mentoring role; their contributions were personal, professional, and technical. In particular thanks is due to Josef Käs, Phil Marcus, Stephen Morris, Ron Panton, Zhen-Su She, and posthumously to David Tritton. Each of the above professors had a significant effect on my view of (physics/engineering) and academic life. My committee members, individually and as a group, were also a great source of wisdom.

Raul Longoria was always present when I needed academic or design or life advice. He was a great supporter of my cross-disciplinary path.

Harry Swinney was my daily mentor throughout the last few years; he pro-

vided the wonderful working environment and the sage advice that allowed me to carry this project along. His contributions were invaluable.

As always, many thanks go to my parents and my sisters who have supported me in so many ways for so many years.

CHARLES NAIM BAROUD

The University of Texas at Austin

December 2001

Transitions from three- to two-dimensional turbulence in a rotating system

Publication No. _____

Charles Naim Baroud, Ph.D.

The University of Texas at Austin, 2001

Supervisors: Harry L. Swinney and Raul G. Longoria

Motivated by the variation of Coriolis effects on planetary scale flows, we explore rotating turbulent flows in a 1 m diameter tank, as the rotation rate is varied. For fast rotation (Rossby number $Ro \simeq 0.1$), the flow becomes quasi-two-dimensional (2D) and leads to an inverse cascade of energy from the injection scale to the scale of the system. In the low-rotation case ($Ro \simeq 1$), the flow is three-dimensional (3D), and only small vortices are observed. A gradual transition is found in the intermediate cases, where structures of increasing size are formed for faster rotation.

The statistics of the velocity increments are compared for the different rotation rates. We observe a transition from typical intermittent behavior in the case of the 3D flow to scale-independent (self-similar) statistics for fast rotation. The self-similar 2D statistics match the predictions for 2D turbulence when using the relative (S_p vs. S_3) scaling, but the scaling of the p th order structure functions (S_p) with distance (ℓ) display an anomalous slope $S_p \sim \ell^{p/2}$. This scaling is further confirmed by the slope of the energy spectrum, where $E(k) \sim k^{-2}$.

The β - and γ - tests of the hierarchical symmetry model [She and L ev eque,

Phys. Rev. Lett., **72** p.336, (1994)] are also applied. β remains constant at $\beta \simeq 0.75$ for low and high rotation rates, indicating flows that are highly intermittent in both cases. The value for γ changes from $\gamma_{3D} = 0.18$ to $\gamma_{2D} = 0.34$ which is the expected value for self-similar turbulence. The combination of these statistics with quantitative visualization shows that the coherent structures which populate the flow produce intermittent statistics in all the cases above, but that the intermittency is scale-independent in the 2D case.

Finally, we apply the Beck-Tsallis nonextensive entropy [C. Beck, Physica, **277A** p.115 (2000)]. The model is slightly modified and used to fit the velocity difference histograms, yielding a value for the nonextensivity parameter q . The value of q is found to agree with other 3D flows for the low rotation rate. In the case of 2D flows, we find a value which is nearly constant at $q \simeq 1.32 \pm 0.03$, thus quantifying the departure from Gaussian scaling.

Contents

Acknowledgments	v
Abstract	vii
List of Tables	xiii
List of Figures	xiv
Chapter 1 Introduction	1
Chapter 2 Theory and Literature Review	7
2.1 Kolmogorov '41 and 3D turbulence	9
2.1.1 Length scales and the energy cascade	10
2.1.2 Similarity hypotheses and structure functions	13
2.1.3 Beyond K41	18
2.2 Two-dimensional turbulence	20
2.2.1 The inverse cascade	21
2.2.2 Self-Similarity and intermittency	31
2.3 Rotating flows	33
2.3.1 Taylor-Proudman theorem	34
2.3.2 Potential vorticity	37
2.4 Is rotating turbulence two-dimensional?	39

2.4.1	Experimental verifications	39
2.4.2	Theoretical and numerical studies of rotating flows	43
2.5	Summary	46
Chapter 3 Experimental Apparatus		48
3.1	The rotating tank	50
3.2	The pumping system	58
3.3	The hot-film system (The black art of hot-film anemometry)	60
3.3.1	Probes and general considerations	60
3.3.2	Probe calibration	63
3.4	Visualization system	65
3.4.1	PIV hardware	66
3.4.2	Algorithms	74
3.4.3	Error estimates and controlling errors	80
3.4.4	Specific algorithms	90
3.5	Summary	94
Chapter 4 Transition from 3D to 2D		96
4.1	Flow description	98
4.1.1	Velocity vectors: Mean jet	99
4.1.2	Stremfunctions: Jet and vortices	99
4.1.3	Vorticity and shear: Vortex interactions	103
4.1.4	Ejection events	106
4.2	Evidence of two-dimensionalization	111
4.2.1	Flow development	111
4.2.2	Lowest rotation 3D flow	113
4.2.3	Top-bottom cross correlation	115

4.3	Mean quantities	116
4.3.1	Radial profiles	117
4.3.2	RMS velocity	118
4.3.3	Reynolds and Rossby numbers	121
4.4	Time series	124
4.5	Structure functions	126
4.6	Hierarchical Symmetry	133
4.6.1	The β -test	134
4.6.2	The γ -test	136
4.7	Summary and discussion	138
Chapter 5 Anomalous scaling in 2D flows		141
5.1	Energy spectrum	144
5.2	Probability distribution functions	146
5.3	Structure functions	148
5.4	Summary	154
Chapter 6 Nonequilibrium statistical mechanics		156
6.1	Application to turbulent flows	159
6.2	Results	161
6.2.1	Fitting parameters	161
6.2.2	Probability Distribution Functions	165
6.2.3	Nonextensivity parameter	165
Chapter 7 Discussion		170
7.1	Contributions	171
7.2	Future work	174
Bibliography		176

List of Tables

3.1	The design parameters and their relative importance.	72
4.1	RMS velocities plotted in Fig. 4.13.	121
4.2	Maximum velocities for the same conditions as in Fig. 4.13.	122
4.3	Data conditions	123
4.4	Values of ζ_p	133
5.1	Values of ζ_p plotted in Fig. 5.7.	153

List of Figures

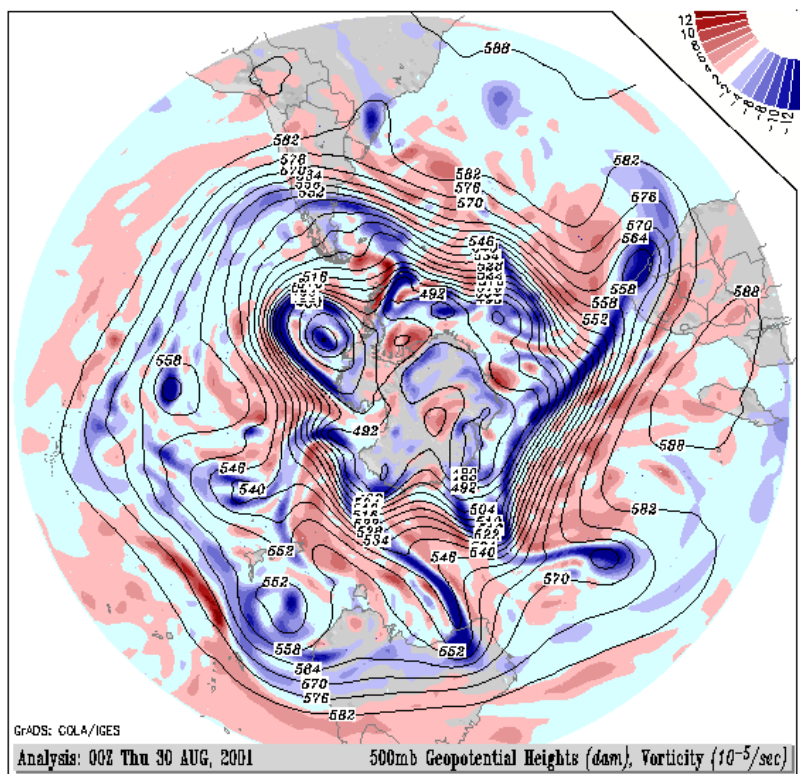
1.1	Atmospheric circulation.	3
2.1	3D turbulence spectra.	14
2.2	2D turbulence spectrum.	23
2.3	Time dependent inverse cascade, from Ref. [69].	29
2.4	Relative structure function exponents from Ref. [70].	32
2.5	High correlation velocities.	42
3.1	Schematic of the rotating tank.	49
3.2	General schema.	51
3.3	Block diagram.	52
3.4	Exploded view of the channel.	54
3.5	Bottom and top plates.	54
3.6	Frequency spectrum with peaks due to rotation.	57
3.7	Sample time series of the flow rate in cm^3/s	59
3.8	Hot film probe.	61
3.9	δv by stopping the tank.	64
3.10	Calibration example	64
3.11	LED ring schematic.	68
3.12	Intensity control.	69

3.13	Current source.	69
3.14	Rotating computer and camera.	71
3.15	Calibration of camera.	75
3.16	Particles	77
3.17	Standard PIV algorithm.	78
3.18	Slices of the peak.	79
3.19	Velocity and vorticity.	81
3.20	Frame straddling technique.	86
3.21	Peak locking fixed	89
3.22	The rectangular mapping.	93
3.23	Rectangular mapping in action.	94
4.1	Vortices and jet	98
4.2	Velocity field	100
4.3	Streamfunctions	101
4.4	Rotated streamfunctions	102
4.5	phase diagram	103
4.6	ω , σ and $\bar{\sigma}$	106
4.7	Two ejection closeups	109
4.8	Image of particles ejecting.	110
4.9	Initial flow setup.	113
4.10	3D slow-rotation flow.	114
4.11	Correlation curves.	116
4.12	Radial quantities.	119
4.13	RMS azimuthal velocity.	120
4.14	Rossby numbers.	123
4.15	Azimuthal velocity in ejection.	125
4.16	Example time series.	127

4.17	2D and 3D histograms of $\delta v(\ell)$.	130
4.18	Example ESS fit.	131
4.19	Structure function exponents.	132
4.20	β test.	135
4.21	γ -test	138
5.1	Two high rotation flows.	143
5.2	High rotation anomalous spectra.	145
5.3	Spiral ejection.	147
5.4	Normalized PDF of δv .	149
5.5	Structure functions.	151
5.6	S_3 for high pumping.	152
5.7	Scaling exponents.	153
6.1	Example entropic vector.	157
6.2	Dependence on κ , 2D.	162
6.3	Dependence on κ , 3D.	163
6.4	Skewness 2D and 3D.	164
6.5	2D fits	167
6.6	3D fits.	168
6.7	Nonextensivity parameter q .	169

Chapter 1

Introduction



This thesis addresses the effect of rotation on turbulent flows. Rotating flows are often of interest in turbo-machinery and other engineering applications (e.g. rotating satellites), but the main motivation for the work described here is the large-scale motion in the atmosphere and oceans, or on other rotating planets. These rotating flows constitute very complicated systems where many parameters can be of major importance, such as stratification or geometry. Complicated models attempting to produce detailed predictions on short time scales have been developed, but their predictive power is often limited. In the case of weather predictions for example, one is often faced with a compromise between accuracy and detail; detailed predictions can be made for times on the order of a day, whereas only general predictions can be made for times up to one week¹.

In this work, we will follow the standard technique of simplifying the problem to a minimal set of parameters, in order to make it tractable. A simplified experiment such as ours cannot make detailed predictions, but it can provide deeper insight into the significance of the few components under study. Of the many variables that change in geophysical flows, we will concentrate on the effects of rotation.

On planetary flows, the effect of rotation can undergo significant changes as a function of several parameters. Let us consider a few example flows to explore this variation:

First, let us compare atmospheric flows on the Earth and on Venus. The size of the two planets is comparable, but while the Earth makes a full revolution once a day, Venus rotates with a period of 243 terrestrial days. Therefore flows with similar length and velocity scales on the two planets would feel the rotation 200 times more on Earth than on Venus! The effects of this difference are visible in the motion of the Venusian atmosphere, which rotates almost as a solid body in the same direction of rotation as the planet, but much faster than the solid core [34].

¹Forecasters in Austin are known to predict a “50% chance of rain tomorrow”: It might rain, or it might not.

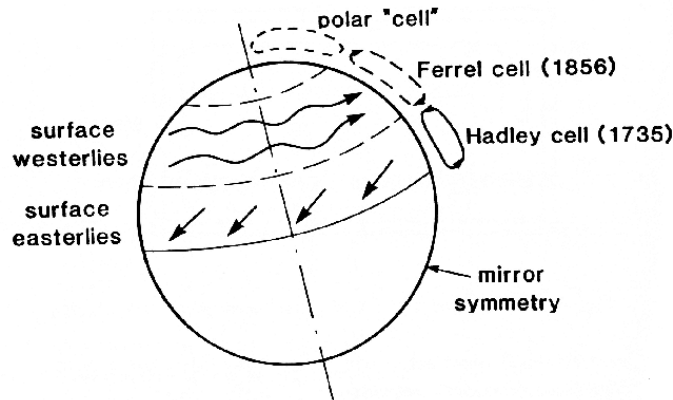


Figure 1.1: Schematic representation of the circulation cells due to convection in the atmosphere, and their dependence on the local rotation component (from Ref. [34]).

Another way that the importance of rotation might vary is due to the planet's curvature. We are interested in the Coriolis force on the flow, and since that force depends on a cross product of the rotation vector with the velocity, only the local vertical component of the rotation vector is important. For this reason, the significance of rotation is maximum at the pole, while the Coriolis effects vanish at the equator. This variation has a significant effect on the motion in the atmosphere, as sketched by Ghil and Childress [34] in Fig. 1.1.

The importance of the rotation is measured by the Rossby number (Ro), which can be thought of as the ratio of two time scales: The first scale is the time scale associated with the rotation ($1/\Omega$, where Ω is the rotation rate in rad/s). The second time scale is the one associated with the flow, e.g. the ratio of a typical length to a typical velocity (L/U). The significance of the Rossby number will become evident in later chapters, but for now let us say that by defining $Ro = U/2L\Omega$, a small Rossby number indicates a flow where Coriolis effects from the rotation of the system are dominant.

The other important parameter is the Reynolds number, which compares the inertial forces to the viscous forces in the flows. The large size of the geophysical flows implies that the Reynolds numbers are usually very large. Therefore the dependence of the flow characteristics on the Reynolds number is weak, since we are always in the high-turbulence regime. However, the dependence on the rotation rate is significant.

As a final example, consider a river of width 100 m and with typical flow velocity 1 m/s. The corresponding Reynolds number is 10^8 . Now consider an atmospheric flow, e.g. a wind, extending 10 km in width, and flowing at 10 cm/s (36 km/h). This wind also has a Reynolds number of 10^8 . To the uninitiated, the Reynolds number similarity would suggest similar flows to the extent that we can ignore the boundaries and the stratification in the atmosphere. Owing however to the Rossby number difference, these flows are extremely different! Assuming that we are at 45° latitude, the local rotation is $[\Omega_e \cos(45^\circ)]$ where $\Omega_e = 7 \times 10^{-5} \text{ s}^{-1}$ is the rotation rate of the earth, so $Ro_{\text{river}} \simeq 100$ while $Ro_{\text{wind}} \simeq 0.1$. This indicates that while the effect of the earth's rotation is 100 times smaller than the inertial forces in the case of the river, Coriolis effects on the wind are 10 times greater than inertial effects². The variation in Rossby number means that even for a fixed Re , the two flows will have very different "character".

It is this change in the character of the turbulence that we are interested in examining in the course of this thesis. We will examine the switch by visually observing the coherent structures in the flows, and by recording long Eulerian time series which will shed light on the relationship between the structures of different intensities that make up the wide spectrum of the turbulence.

To explore these changes, one would like to keep all parameters constant and only vary the Rossby number. Numerical simulations are sometimes used to

²The Rossby number can be extracted from the Navier-Stokes momentum equation by taking the ratio of the nonlinear inertial term to the coriolis term

achieve such control, but simulations are limited in several ways. They cannot reach the high Reynolds numbers that experiments can reach. They also suffer from numerical instabilities when the separation of scales is very high, as is the case with the important boundary layers in rotating flows. The alternative controlled way to vary a single parameter is experimental work that is sometimes referred to as “analog computing”. In our experiments, we keep the geometry and the forcing method fixed, and vary only the rotation and forcing rates in order to keep all parameters fixed and isolate the effects of Rossby number on the flows under study.

In a laboratory experiment, Reynolds numbers of 10^8 are very difficult to reach, but one can typically obtain $Re \simeq 10^5$. On the other hand, we are able to achieve $Ro < 0.1$ by rotating the experiment rapidly, or we can rotate very slowly and obtain Rossby numbers larger than 1. Since it is the Rossby number dependence that we are interested in studying, our apparatus is uniquely positioned to look at the questions raised above.

In particular, one effect of rotation is to force the flow to become two-dimensional (2D). Since this is true for turbulent as well as laminar flows (Chapter 2), it is important to understand the theory of turbulence for 2D turbulence, and in particular how it relates to the traditional three-dimensional (3D) turbulence theory. Chapter 2 starts by outlining the theory of 3D turbulence as developed by Kolmogorov in 1941, after which Kraichnan and Batchelor’s analyses for 2D turbulence are described. The effect of rotation on fluid flows is discussed in the second half of the chapter (Sections 2.3 and 2.4) from a theoretical, experimental, and numerical points of view. What is known (or believed) about the effect of rotation on turbulence is also described.

Probing the effects of rotation variations on flows is therefore analogous to exploring the difference between 3D and 2D turbulence. The two regimes of turbulent flow are different enough that there is some controversy about whether 2D

flows can be considered turbulent at all! However, we are able to switch continuously between 3D and 2D flows in our apparatus by varying the rotation rate. The experiment and its subsystems used to produce and measure the flow are described in Chapter 3.

The main difference between 2D and 3D turbulence is the absence of vortex stretching in the 2D case. This stretching corresponds to the nonlinear term in the Navier-Stokes equation, i.e. the term responsible for the transfer of energy among different scales in the system. We achieve the 2D flow by inhibiting the vortex stretching to varying degrees by controlling the rotation rate. This transition and the associated dynamical and statistical changes in the flow will be the subject of Chapter 4.

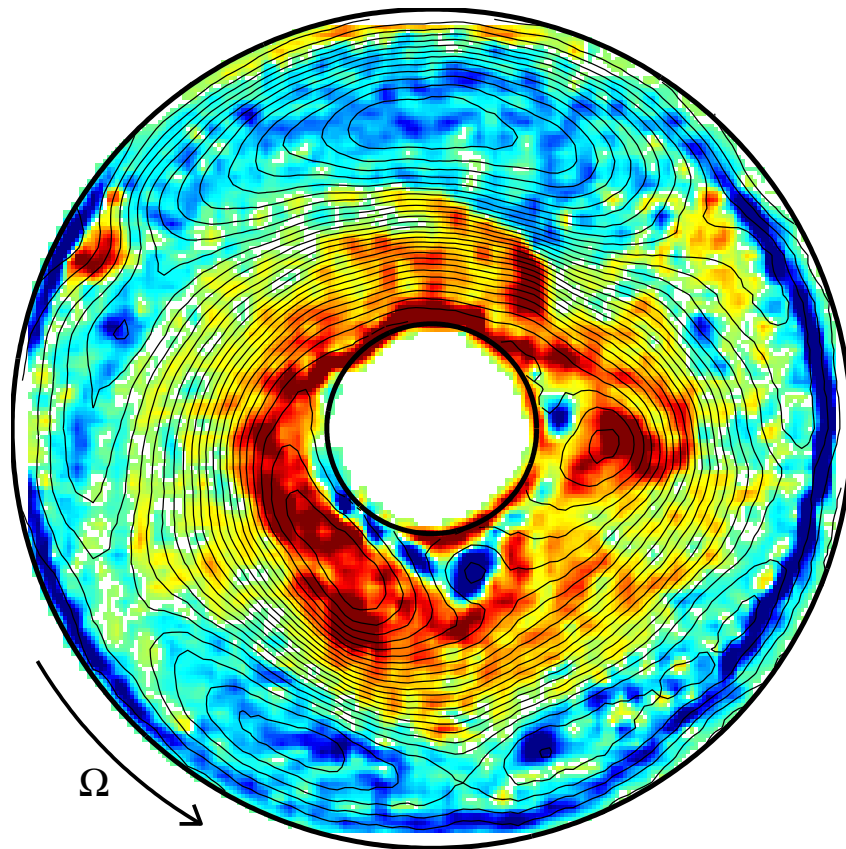
The dynamics of the 2D flow are also interesting as a model of geophysically relevant turbulent flows, and also as a model for plasma turbulence. They are explored in Chapter 5 where some surprising results are shown. These results, previously unpredicted, point to a flow which fails to obey some of the most solid predictions of Kolmogorov's 1941 theory of turbulence, namely the 4/5th law. A possible reason is given for this discrepancy, which involves the strong anisotropic shear experienced by the vortices.

Finally, Chapter 6 explores the connection between turbulence and non-equilibrium statistical mechanics. In particular, the difference between 2D and 3D turbulence is explored from the standpoint of the *Tsallis non-extensive entropy* (big words which will be explained in due time).

The discussion chapter then summarizes the results in this thesis and gives a brief list of interesting subjects that can be pursued as extensions of this work, or using this apparatus.

Chapter 2

Theory and Literature Review



Is the three dimensional structure of turbulence really important? Is the stretching of vortex lines crucial? a *sine qua non* feature of the evolution of turbulence?

(Phillip Saffman, *The Global Geometry of Turbulence, Impact of Non-linear Dynamics*)

This thesis deals with switching between three-dimensional (3D) and two-dimensional (2D) high Reynolds number flows in a rotating system. While much work has been done on the 2D and 3D regimes separately, the relation between these two kinds of turbulent flow is complicated and badly understood. Rotating systems offer an ideal framework to explore the transition from 3D to 2D, since the fast rotation forces the flow to become quasi-two-dimensional, and the 2D approximation depends strongly on the rotation rate. We can therefore inhibit the motion in the third dimension to varying degrees by rotating more or less rapidly. As these questions begin to be studied numerically, precise experimental measurements are needed to compare with numerical results. No experiments have explicitly addressed the 3D-2D transition since the late 1980's, and our experiment should fill this void, and provide the first quantitative measurements of the transition.

This chapter starts by introducing some essential concepts in turbulence theory through a discussion of the 1941 Kolmogorov (K41) theory. This theory provides a statistical approach to the description of turbulent flow, by searching for scalings of variables such as the energy or the moments of the velocity differences. We begin by introducing the lengths which bound the applicability of Kolmogorov's theory in the context of the energy cascade in Section 2.1.1. In Section 2.1.2, we look at the processes in the cascade in more detail, by introducing the fundamental hypotheses that the theory is based on, namely the self-similarity of the cascade. Finally, deviations from K41 (usually in the form of intermittent bursts) in experimental measurements of 3D flows are discussed. These deviations will be compared in

future chapters with the behavior of 2D flows.

After 3D turbulence, the theory and concepts of 2D turbulence are developed in Section 2.2, as introduced by Kraichnan and Batchelor and others. Here, the 3D forward energy cascade is replaced with an inverse cascade of energy to the large scales, and the questions of self-similarity and intermittency are raised in the context of a turbulent flow populated by long-lived coherent vortices. These initial theory sections can be skipped by readers who are already familiar with the basic ideas of turbulence.

With these concepts in hand, we then survey the effect of rotation on fluid flows, and derive the geostrophic equation by introducing the important dimensionless parameters of rotating flows. Section 2.3 shows the classic argument of the Taylor-Proudman theorem which predicts that a rotating flow becomes two-dimensional. Finally, Section 2.4 addresses the applicability of this theorem to turbulent flows, and surveys experimental, numerical and theoretical work that has gone into checking whether rotating turbulent flows are two-dimensional.

2.1 Kolmogorov '41 and 3D turbulence

In a broad sense, the engineering approach to turbulence is different from a physicist's approach. Engineers are usually interested in flows interacting with engineering structures, such as wall bounded flows (aerodynamics) or pipe flows. They are also typically concerned with the large, energy-containing scales [66]. In contrast, physicists are more inclined to study the aspects of turbulence that are universal, and this typically involves moving away from any boundaries, often considering the idealized case of isotropic homogeneous turbulence which occurs at the smaller scales. However, both the physicist and the engineer use as their basis the formalism introduced in Kolmogorov's 1941 (abbreviated as K41) theory of turbulence, and the later corrections to it.

The physicist’s approach is adopted in this thesis. In other words, we use statistical tools to look for deviations from K41, in a way that can shed light on the detailed mechanisms at play in the bulk of the fluid. Since we are interested in the differences between turbulence in 3D and 2D, we need to first develop an understanding of full 3D turbulence. This is done in this section where the most relevant aspects of Kolmogorov’s theory are introduced. Some of the known results in 3D flows, including deviations from K41 are also discussed, in anticipation of comparing to 2D flows.

2.1.1 Length scales and the energy cascade

Two length scales are important in K41: they describe respectively the largest and smallest scales at which the theory is applicable. We proceed in this section following the description of Monin and Yaglom [65].

Let us imagine a flow in a wind tunnel at very high Reynolds number, Re_0 ; let us also suppose, for simplicity, that there exists a critical Reynolds number Re_{cr} at which turbulence starts¹. Our wind tunnel flow contains eddies that are about the size of the tunnel. The relevant Reynolds number for these large eddies (Re_1) is slightly smaller than Re for the mean flow, but if Re_0 is large enough, then Re_1 is still far above the Re_{cr} . If these large eddies can transfer their energy to smaller sizes, then the flow will contain eddies at scale l_2 , smaller than the scale of the largest eddies. The Reynolds number for that scale, Re_2 , is again smaller than Re_1 but is still larger than Re_{cr} . One can imagine the process repeating over and over, until we reach a length scale l_n at which the Reynolds number is around the same order as Re_{cr} .

Kolmogorov used a similar argument to predict the existence of a scale at which viscous effects become important [65]. He argued that at these small scales,

¹While this critical value might not be well defined in the sense of dynamical systems, there exists a range of values above which the flow is clearly turbulent.

only length (η), viscosity (ν), and the mean rate of energy transfer ($\langle \varepsilon \rangle$) are important quantities; this is known as the *first universality hypothesis*, since it should apply regardless of the large scale flows in the system [33]. By dimensional analysis, the only length that can be extracted from the above three quantities is the *Kolmogorov length scale*,

$$\eta = \left(\frac{\nu^3}{\langle \varepsilon \rangle} \right)^{1/4}. \quad (2.1)$$

The “dissipation scale” at which most of the transfer of kinetic energy into heat occurs is related to η , as noted by Libby who quotes the value $10 \times 2\pi\eta$ as the length where viscous effects become important [55]². Nonetheless, η is a useful number characterizing the scale above which the turbulent fluctuations can be safely interpolated, for example in numerical simulations [55].

In calculating η in an experimental situation, a major hurdle is to estimate $\langle \varepsilon \rangle$. This is often done by using the formula for a shear flow [55],

$$\langle \varepsilon \rangle \simeq 15 \frac{\nu}{U^2} \left\langle \left(\frac{\partial u}{\partial t} \right)^2 \right\rangle, \quad (2.2)$$

where U is the mean velocity and u is the fluctuating velocity in the direction of U . This equation is based on the assumption of local isotropy and on the Taylor frozen turbulence hypothesis. The $\langle \cdot \rangle$ denotes an appropriate average, usually ensemble or time average.

Next, we turn our attention to length scales much larger than η . The flow is bounded at the largest scales by the system size L , but the largest energy containing structures are typically slightly smaller than L . The *integral scale*, L_i , is a measure of these large scales, and it is defined as the integral of the two-point correlation

²Frisch gives the value 30η [33].

function. For a stationary time series $u(t)$, we can define the two-point correlation as

$$R(\tau) = \langle u(t) \cdot u(t + \tau) \rangle. \quad (2.3)$$

The integral of R with respect to τ , which converges if the correlation decays fast enough, defines a time scale τ_i , by equating

$$\int_0^{\tau_i} d\tau = \int_0^{\infty} R d\tau, \quad (2.4)$$

and solving for τ_i . By using Taylor’s frozen turbulence hypothesis, τ_i can be transformed into a length scale by using the identity $L_i = U\tau_i$. This length scale is a useful measure describing the large, energy-containing scales in the flow.

The scalings of K41 apply in the range bounded by the two lengths η and L_i , or the length scales where both viscosity and boundary effects can be ignored. Energy must be conserved in this range, since viscosity is unimportant, and we assume that no energy is being injected at these scales. This implies that in the steady state, at a given wavenumber k , the amount of energy added to $E(k)$ from smaller wavenumbers (larger lengths) must equal the amount of energy “cascaded” down to larger k (smaller lengths). This spectral range is known as the inertial subrange, and it is characterized by the presence of the energy cascade which transfers energy, without loss, from larger to smaller length scales.

The dependence of energy on wavenumber was predicted by Kolmogorov, using dimensional arguments again, to scale as

$$E(k) \sim C_k \langle \varepsilon \rangle^{2/3} k^{-5/3}. \quad (2.5)$$

Here, $C_k \simeq 0.5$ is the (elusive) Kolmogorov constant which is believed to be universal for 3D turbulence [91]. This energy cascade has been verified over many decades of

scaling, for a wide variety of open and closed flows, as shown in Fig. 2.1. The slope of the energy spectrum is found to be very close to $-5/3$.

2.1.2 Similarity hypotheses and structure functions

Kolmogorov's 1941 theory of turbulence involves three assumptions regarding isotropic homogeneous flows; by using these assumptions and dimensional analysis arguments, Kolmogorov was able to make quantitative predictions about the scaling of certain quantities such as energy $E(k)$, or the moments of the velocity differences (see below). Since the publication of the 1941 paper, a large part of turbulence research has consisted of verifying the predictions and then refining the assumptions by looking for deviations from theoretically predicted results. In this sense, Kolmogorov's assumptions can be viewed as hypotheses which can be tested and refined. Frisch [33] presents the K41 theory using the three main hypotheses, quoted here and discussed below:

- **H1** In the limit of infinite Reynolds number, all the possible symmetries of the Navier-Stokes equation, usually broken by the mechanisms producing the turbulent flow, are restored in a statistical sense at small scales and away from boundaries.
- **H2** Under the same assumptions as H1, the turbulent flow is self-similar at small scales.
- **H3** Under the same assumptions as H1, the turbulent flow has a finite non-vanishing mean rate of dissipation $\langle \varepsilon \rangle$ per unit mass

Starting with the third hypothesis, we note that it is readily verified in 3D flows. This is the reason why even very fast airplanes still experience a large drag, even though viscous effects are minimal at such high Reynolds numbers. In 2D flows, it is not known whether this assumption applies, and this is a current research

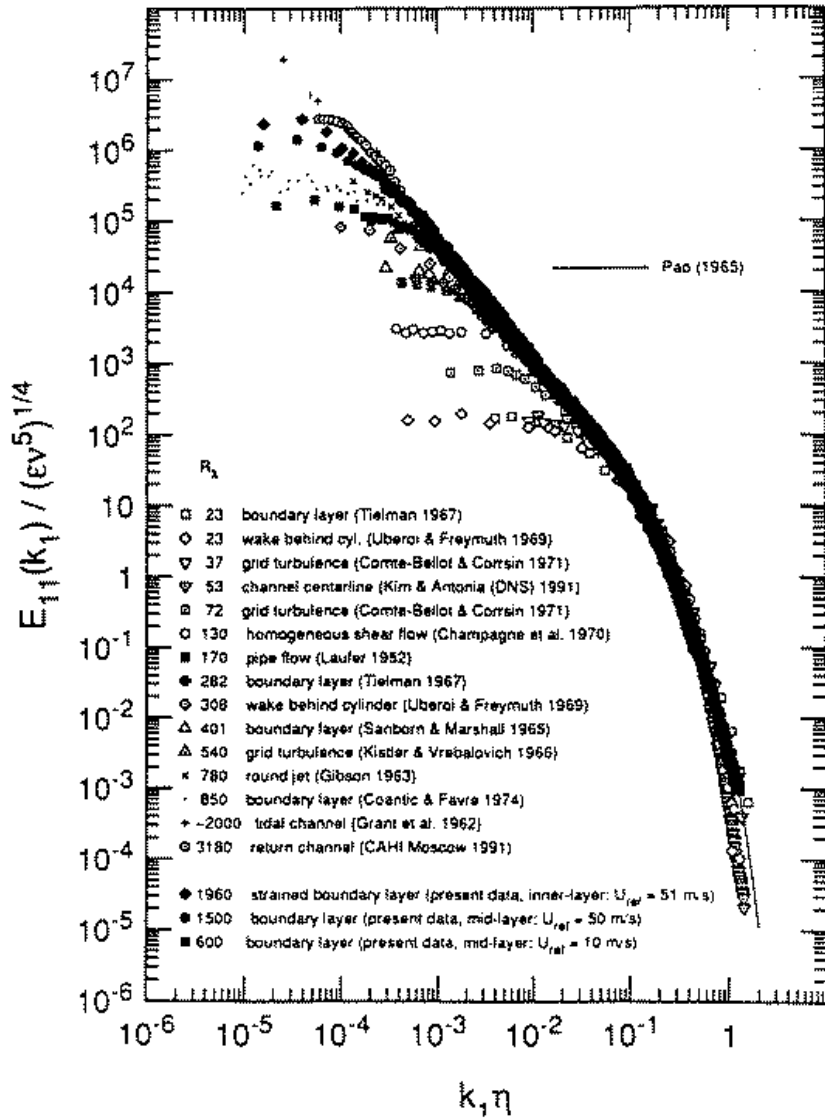


Figure 2.1: Compilation of measurements of the energy spectrum, $E(k)$, from many different sources. Copied from Libby [55], originally appeared in Saddoughy, 1992.

question. There is also some controversy about its validity in the true limit of $Re \rightarrow \infty$, but this question is outside the scope of the current study.

In the first hypothesis, by *small scales* we mean those much smaller than the integral length, yet larger than the dissipation scale. The *symmetries* in question are symmetries of time and space translation, rotations, Galilean transformations, etc. These appear as a result of the symmetries in the equations and the boundary conditions, are might be system specific (e.g. in our rotating tank, we find an “angular translation” symmetry). It is intuitively obvious that these symmetries are broken by turbulence, for example by consider the time-translation of a velocity time series. While a laminar time series might be invariant under time translation (at least for an integer number of the period, for a periodic flow), a turbulent time series never repeats itself, and therefore the translational symmetry is broken for any time step.

In order to proceed with length scales, let us transform the time series to a spatial record using Taylor’s frozen turbulence hypothesis, and define the velocity increment over a distance ℓ as

$$\delta v(x, \ell) = v(x + \ell) - v(x).$$

By lack of translation symmetry, it is clear that $\delta v \neq 0$ in general. These velocity increments are a useful tool to consider, because they contain all the statistical information about the flow structure at the small scales [65]. The study of the statistics of these velocity differences and their high-order moments has become a standard approach to the study of turbulence in recent years. The p th order moment or δv , or structure function, is defined as $S_p(\ell) = \langle [\delta v(\ell)]^p \rangle$. The statistics of these structure functions allow us to test the recovery of the symmetries in a statistical sense.

Symmetry with respect to rotation is more commonly referred to as *isotropy*; K41 assumes that isotropy is recovered at small scales, even in a flow which is anisotropic at large scales such as a boundary layer flow or a jet. Departures from this assumption are the subject of some current research, and small corrections have been found [50]. Translation symmetry implies that the statistics are stationary, since it implies that the results obtained do not depend on the starting point. This allows us to use the statistics of the structure functions and to replace time averages with ensemble averages.

It is the second hypothesis which will concern us the most in this thesis. Self similarity implies that the velocity increments must possess the scaling

$$\langle \delta v(\lambda \ell) \rangle \sim \lambda^h \langle \delta v(\ell) \rangle \quad (2.6)$$

for any³ λ , where h is constant scaling exponent independent of ℓ or λ . The symbol ‘ \sim ’ is used in the sense of scaling.

Scale-invariance also implies a power law scaling of the structure functions. It can be shown that Eq. 2.6 implies that the structure functions $S_p(\ell)$ have a power-law dependence on the distance; if we use the notation $\ell = \lambda \ell_0$,

$$\langle \delta v(\lambda \ell_0) \rangle \sim \lambda^h \frac{\ell_0^h}{\ell_0^h} \langle \delta v(\ell_0) \rangle \quad (2.7)$$

which can be written as

$$\langle \delta v(\lambda \ell_0) \rangle \sim \ell^h \langle \delta v(\ell_0) \rangle \ell_0^{-h}. \quad (2.8)$$

Since $\langle \delta v(\ell_0) \rangle \ell_0^{-h}$ is a constant, we raise the equation above to the power p and drop the proportionality constants, to obtain

³as long as $\lambda \ell$ is smaller than the integral length L_i .

$$S_p = \langle [\delta v(\ell)]^p \rangle \sim \ell^{hp}. \quad (2.9)$$

A departure from the scaling above can therefore be interpreted as a violation of one or both of the hypotheses H1 or H2.

In order to obtain the value of h , we invoke the so-called *four-fifths law*. The importance of this law comes from the fact that it is a rather rigorous result (few assumptions), and that it contains important information about the mean energy transfer rate, $\langle \varepsilon \rangle$. The law can be stated as follows [33]:

Four-fifths law [33]. In the limit of infinite Reynolds number, the third order structure function of homogeneous isotropic turbulence, evaluated for increments ℓ small compared to the integral scale, is given in terms of the mean energy dissipation per unit mass $\langle \varepsilon \rangle$ (assumed to remain finite and non-vanishing) by

$$S_3(\ell) = \langle (\delta v)^3 \rangle = -\frac{4}{5} \langle \varepsilon \rangle \ell. \quad (2.10)$$

This relation immediately allows us to determine the value of the scaling exponent $h = 1/3$. This leads to one of the fundamental and widely tested results of the 1941 Kolmogorov theory, namely that

$$S_p \sim \ell^{\zeta_p}, \quad (2.11)$$

and

$$\zeta_p = p/3. \quad (2.12)$$

This is a very important result which we will return to in Section 2.1.3 in discussing 3D flows, and also in later chapters when we test the applicability of this scaling in the 2D and 3D flows in our experiment.

2.1.3 Beyond K41

The general picture of Kolmogorov's theory of three dimensional turbulence is as follows: If energy is injected into the flow at some scale k_i , it will cascade without loss to larger k through the nonlinearities in the Navier-Stokes equation, i.e. through the stretching and folding of vortex tubes. The energy scaling of this cascade goes as $E(k) \sim k^{-5/3}$ in the inertial range, until the Kolmogorov length is η reached, beyond which point the energy is dissipated through the action of viscosity. The cascade is self-similar, meaning that the rate of energy transfer is constant for all length scales, and one cannot distinguish the dynamics at any length in the inertial subrange from other lengths. Furthermore, a point which has been glossed over is that the dynamics in the cascade are assumed to be *local* in k space, meaning that eddies interact with other eddies of similar size.

Soon after 1941, Kolmogorov and others realized some shortcomings of K41, leading to corrections to the theory, as well as new approaches to the modeling of turbulence. Recently, the issue of self-similarity of the energy cascade and the related question of intermittency have been the subject of much attention. Structure function exponents have been measured with increasingly higher precision [3, 9, 54]. While they show a scaling range $S_p \sim \ell^{\zeta_p}$, the measured values of ζ_p are clearly different from the prediction $\zeta_p = p/3$; in fact, the ζ_p dependence on p is not linear. This is typically referred to as intermittency [66], and it is a sign of scale dependent flow statistics. In other words, the departure of the structure function scaling is direct evidence that one or more of the K41 hypotheses is incorrect, and it is H2 that is viewed as the culprit. One of the concerns of this thesis will be to discuss intermittency and scale-dependence in more precise ways, by making the distinction between the two. In particular, we will study the effects of two-dimensionalization on both the intermittent behavior of the flow and on the scale-dependence of the statistics.

Several theories attempt to explain the departures from the K41 scaling of the structure functions. Kolmogorov himself suggested the “refined similarity hypothesis” in 1962, which replaced the mean energy transfer $\langle \varepsilon \rangle$ with a local energy transfer function ε_ℓ as a function of the length scale. Other models have also been suggested such as the *fractal* or *multi-fractal* models. These models assume that the eddies of size ℓ do not fill the whole space at that scale, but a fractal subset of it. The details of all these models are rather complex, and do not relate to the results described in this thesis; the reader is referred to Chapter 8 in Frisch [33] for a review of intermittency models.

One model that will be used to compare with our experimental results is the She-L  v  que model [80], which gives a physical argument for the lack of self-similarity. The authors reason that as a vortex continually stretches and folds, it eventually collapses onto a singular line where the velocity gradients are very large (infinite for zero viscosity). These collapsed vortices were observed in simulations [79] and experiments [27]. However, the She-L  v  que theory predicts that the rate of energy transfer as a function of scale has a hierarchical symmetry, whereby intense “more intermittent” structures are related to weaker, “less intermittent” structures. The details of this model will be discussed in Chap. 4. For now, we will simply quote the scalings that are derived in Ref. [80], namely for the structure function exponents

$$\zeta_p = \frac{p}{9} + 2 \left[1 - (2/3)^{p/3} \right], \quad (2.13)$$

and the energy spectrum

$$E(k) \sim k^{-5/3-0.03}. \quad (2.14)$$

Naturally, a deviation of 0.03 in the energy spectrum is very difficult to

measure experimentally. However, the values of the structure function exponents of Eq. (2.13) match the experimentally obtained values very well.

2.2 Two-dimensional turbulence

Theorists have found in 2D turbulence a simplified system in which to test the ingredients of full 3D turbulence theories. Even though the two flow regimes are quite different, understanding the differences between them and the mechanisms at work in the 2D case can shed light on the importance of the 3D motions. In particular, vortex stretching is a purely 3D phenomenon which is not allowed in 2D and as seen above, vortex stretching is believed to be the main source of scale-dependent intermittency in 3D flows. By comparing 2D and 3D flows, the effects of the stretching and folding of vortices can be isolated and understood better.

The difference between 2D and 3D turbulence was first addressed by Kraichnan in 1967 [49], followed shortly by Batchelor [6]. These authors realized that the 2D and 3D regimes were significantly different, but Kraichnan cautioned that “2D turbulence is nowhere realizable in nature”, other than as an approximation to the large scale processes in the atmosphere. Nevertheless, the application of 2D turbulence ideas to geophysical flows has been a major motivation for workers in the field. Since Kraichnan’s early work, experiments and numerical simulations have been used to verify the theory, and sometimes motivate further theoretical study. Recently, many papers dealing with the subject of 2D turbulence have been published and this is an area of significant current interest in the physics literature.

A few aspects of 2D turbulence have attracted the most attention. This section exposes the most important discoveries, as well as the ones most pertinent to the rest of the dissertation. First, we discuss the existence of the inverse energy cascade, by citing theoretical, experimental and numerical work. Then we turn our attention to issues of self-similarity and scale-dependence, and how they compare in

2D with the 3D case discussed above.

2.2.1 The inverse cascade

Kraichnan’s 1967 paper [49] uses arguments similar to Kolmogorov’s 1941 theory, with the added constraint of two-dimensionality, to derive the new energy transfer mechanisms: In the 2D inertial range, not only must we conserve energy, we also have to conserve enstrophy and all powers of it⁴. We define the enstrophy, Ω , as

$$\Omega = \int \omega^2 dk. \tag{2.15}$$

This conservation is due to the fact that vortex stretching is not allowed in 2D flows, and viscosity is not important at moderate length scales ($L_i \ll \ell \ll \eta$) so a patch of fluid must conserve its vorticity. It is interesting to note, furthermore, that high Reynolds number 2D flows are a good approximation to *ideal flow*, where vorticity is a passive scalar that follows material motion [67].

The direct consequence of energy and enstrophy conservation is the existence of an inverse energy cascade rather than the forward cascade of 3D turbulence. A reasoning for the inverse cascade is given succinctly by Lesieur [53] as sketched below, with the original theorem being due to Fjortoft [32]: Consider the two-dimensional Euler equation in Fourier space, retaining only three representative modes, $k_2 = 2k_1$ and $k_3 = 3k_1$. The energy content of a given Fourier mode can be written as $E(k_i, t)$, and the energy transfer between times t_1 and t_2 can be written as $\delta E_i = E(k_i, t_2) - E(k_i, t_1)$. Using this notation, energy conservation implies that

$$\delta E_1 + \delta E_2 + \delta E_3 = 0 \tag{2.16}$$

⁴Enstrophy is a measure of vorticity. The relationship between enstrophy and vorticity is the same as the relationship between energy and velocity.

while enstrophy conservation can be written as

$$k_1^2 \delta E_1 + k_2^2 \delta E_2 + k_3^2 \delta E_3 = 0. \quad (2.17)$$

These two equations can be solved simultaneously to give

$$\delta E_1 = -\frac{5}{8} \delta E_2 \quad ; \quad \delta E_3 = -\frac{3}{8} \delta E_2 \quad (2.18)$$

and

$$k_1^2 \delta E_1 = -\frac{5}{32} k_2^2 \delta E_2 \quad ; \quad k_3^2 \delta E_3 = -\frac{27}{32} k_2^2 \delta E_2. \quad (2.19)$$

If $\delta E_2 < 0$, meaning that the middle wavenumber is losing energy, more energy will transfer to k_1 than to k_3 and more enstrophy will transfer to k_3 than to k_1 . This indicates that the sign of the energy transfer is mostly from k_3 (large wavenumber) towards k_1 (small wavenumber), indicating a cascade of energy of opposite sign to the Kolmogorov cascade in 3D. In practice, this means that when small eddies form, they continually grow in size until they reach the size of the system they are in. This also means that the sign of $\langle \varepsilon \rangle$, assumed to be positive for 3D flows, will be negative in the 2D cascade. However, the dynamical details of the inverse cascade were not discussed by Kraichnan: He did not propose a mechanism for the energy to transfer to large scales. This is still a point of debate, and might well depend on the specific system.

If a flow is forced at a wavenumber k_i , Kraichnan's theory predicts that most of the energy will transfer to smaller wavenumbers, or larger length scales. By assuming constant energy flux and random vortex interactions, one can show that the energy in the inverse cascade range, $k < k_i$, must scale as $E \sim k^{-5/3}$, similarly to the 3D case (see Fig 2.2). Conversely, enstrophy cascades from k_i to larger

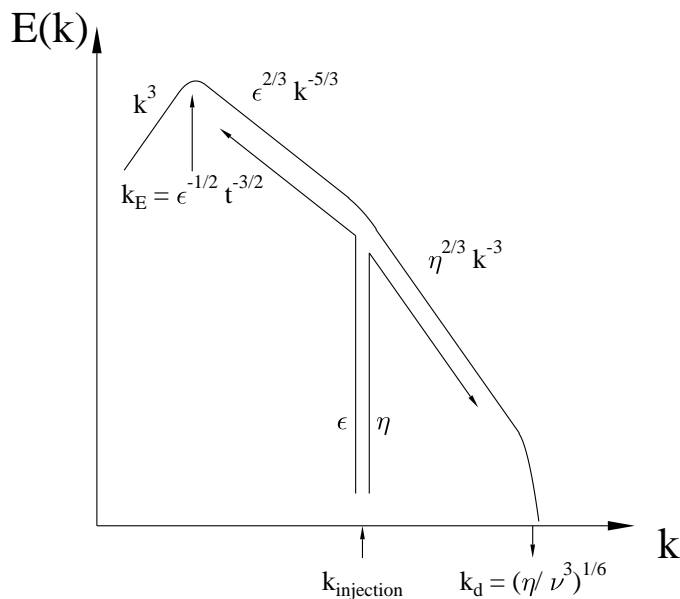


Figure 2.2: Sketch of the 2D energy cascade. The inverse cascade moves energy from the injection scale to low k , while the enstrophy cascades to high k . Figure by E. Weeks [101], after Lesieur [53].

wavenumbers, where it is dissipated by viscosity. The slope of the energy spectrum in this range was predicted by Batchelor to be $E \sim k^{-3}$ [6], although corrections to this result exist and will be discussed below.

Note that the inverse cascade is time-dependent; the scale of the largest eddies (k_E) continues to grow indefinitely with time in an unbounded system. In a real system, the cascade must stop once it has reached the size of the container. At that stage, energy must be dissipated through some mechanism, or otherwise it will condense and the slope of the spectrum will increase. Kraichnan recognized this piling up of energy, and noted that it is “*analogous to the Einstein-Bose condensation of a finite two-dimensional quantum gas* [49].”

We will now turn to numerical and experimental verifications of the 2D cascade as presented in the theory above. These verifications came many years after the original publication of the theory, due to the difficulty of setting up 2D exper-

iments. We will concentrate here on the forced turbulence case; contrary to 3D turbulence, where decaying and forced flows are similar, the inverse cascade of 2D turbulence is time-dependent. In the forced case, the cascade will continue to reach lower wavenumbers until the system size is reached, while this cannot occur in the decaying case, since no energy is being introduced in the system [66].

Numerical verification

Several factors make numerical simulations of 2D turbulence much easier than 3D simulations. While achieving a given resolution in a 3D simulation requires n^3 grid points, 2D simulations only require n^2 . This allows n to be as high as 2048 in 2D simulations on current computers, higher than in the 3D case [12]. However, other important factors also affect the ability to simulate large Reynolds number flows; since energy cascades to larger scales in 2D, one does not face the same limitations as in 3D simulations where a higher Reynolds number means the need for finer resolution. In fact, most of the energy in a 2D turbulent flow is contained in length scales larger than the injection scale, which means that the necessary resolution of the calculation is almost fixed regardless of the Reynolds number. The temporal resolution is still affected by the typical flow velocities, but this is a less important constraint. For this reason, even early simulations of 2D turbulence (e.g. [83]) provided important insight into the nature of high-Reynolds number 2D flows.

Siggia and Aref [83] used vortex methods to simulate a 2D flow and were able to reproduce the inverse cascade of energy, as early as 1981. More recently, Smith and Yakhot [86] studied the details of the inverse cascade, and they found that vortices grew to reach the size of the system. These vortices were found to cause a steeper energy spectrum, consistent with the “condensation of energy” suggested by Kraichnan. Finally, Boffetta et al. [12] also obtained the expected energy

spectrum for the inverse energy cascade range, before the vortices reached the size of the system. The authors in [12] also checked the validity of the 2D equivalent to Kolmogorov’s four-fifths law (see derivation in [10]), which states that

$$S_3(\ell) = +\frac{3}{2}\langle\varepsilon\rangle\ell. \quad (2.20)$$

The agreement between the simulations and the value of S_3 was quite good over almost a decade of scaling.

The papers above concentrate on what the authors term “the inverse cascade regime”, or the transient regime before the energy buildup has reached the largest scales in the system. At long times, Boffetta et al note that they never see any vortices of size larger than the injection scale, confirming earlier experimental observations [69] that “*the inverse cascade does not proceed by vortex merging*”, but rather by the formation of clusters of small vortices [12].

Most other simulations in the literature were interested in decaying 2D turbulent flows (e.g. [20, 22, 60]). While the details of decaying turbulence are quite different from those of forced turbulence, we note that the authors do find the expected slope of the energy spectrum, namely $E(k) \sim k^{-5/3}$.

In the enstrophy (forward) cascade regime, the scaling is much less certain. Soon after the publication of the Kraichnan-Batchelor theory, Saffman proposed the scaling $E(k) \sim k^{-4}$ for flows with coherent vortices present [76]. Saffman’s physical argument is that the coherent structures can trap the energy and keep it from escaping to small scales, and thus they inhibit the forward cascade further.

Resolving the enstrophy cascade in simulations has proved difficult, due in part to the fact that simulations that resolve the large (energetic) scales typically have a limited scaling region for the enstrophy cascade range, making it more difficult to obtain a clear scaling exponent. Recently however, Laval *et al.* [51] found that the dynamics of the small scales in the flow are nearly passive, meaning that the small

scale structures are simply advected by the large scale motions. This corresponds to a non-local interaction, since large and small vortices are interacting directly [51]. They measured an exponent close to -3.5 in the enstrophy cascade, in the presence of large and small scale structures.

Experimental verification

Experimentally, the situation is reversed from simulations. Turbulent flows naturally tend to become 3D, making 2D turbulence experiments challenging to design and to run. In order to achieve a quasi-2D flow in an experiment, one of three major techniques is used:

- *Stratification*, in a broad sense. These experiments can be motivated by geophysical continuous stratification [30], but soap films [24, 14] and thin layer [70] experiments also fall under this category. These experiments favor structures and vortices which are thin in the direction of the stratification gradient and wide in the plane of constant density, sometimes referred to as “pancake” vortices. There is some evidence to suggest that spots such as the Great Red Spot on Jupiter are indeed wide and thin due to stratification.
- *Rotation*, as used in our case, and as discussed in depth below.
- A *magnetic field* is used in conjunction with conducting fluids, in magneto-hydro-dynamics (MHD) experiments [88]. Here, the 2D approximation improves with the strength of the magnetic field, similarly to the rotating flows discussed below. The forcing can be electrical or thermal.

Before we describe the experiments, an important distinction needs to be made about 2D flows as they are studied theoretically or numerically, versus quasi-2D turbulence produced in experiments and in nature. While the theoretical and

numerical studies focus on the Navier-Stokes equations in two dimensions, experimental realizations of 2D flows are done by removing (or reducing) the dependence on the third dimension. In rotating flows, as we will see below, this is done by aligning the vortices with the axis of rotation. Therefore we are left with a flow which extends in the third direction, but where the derivatives vanish along the axis of rotation due to the so called geostrophic constraint. This is a different mathematical limit than the problem of 2D Navier-Stokes, and there are no fundamental reasons to expect that they should reduce to the same one. The two limits are similar in several respects such as the lack of vortex stretching, but it is not necessary for columnar vortices to interact with each other in the same way as purely 2D vortices. This distinction is especially important in the quasi-2D cases for intermediate rotation rates.

Some landmark experiments have been performed over the years providing support for Kraichnan's theory, and possibly motivating some corrections to it. Of these experiments, Sommeria's 1986 measurement of the scaling in the inverse cascade region was the first [88]. This experiment was performed in a magnetically confined mercury square, and though the scaling region was rather small, it provided the first experimental observation of a scaling region at length scales larger than the injection length, and his scaling was consistent with the $k^{-5/3}$ scaling of the Kraichnan theory.

It took 12 years before the next important experimental work came out testing Kraichnan's theory. Advances in imaging techniques, Particle Image Velocimetry in particular, provided the opportunity to obtain instantaneous velocity fields on a plane slice. This is a limitation for 3D turbulence, but in the case of 2D flows, the technique provides all the necessary information to analyze the flows. This technique was used by Tabeling and his co-workers in a series of papers that studied the turbulent motions in a thin layer of electrically conducting brine (see e.g. [70]).

The experiment consisted of two stably stratified layers of salt-water, the top layer being quasi-two-dimensional because of the high aspect ratio and because of the lack of direct wall friction. They used fixed magnets below the electrolyte and a fluctuating electrical current to force the flow. The location of the magnets was used to determine the forcing length.

Paret and Tabeling measured a time-dependent inverse cascade of energy from the injection scale to the largest scale in the system [69], shown in Fig. 2.3. They showed a time-dependent buildup of the energy from the start of the experiment, starting from the injection length and extending to the size of the trough. The intermediate-time spectrum had a profile consistent with $E \sim k^{-5/3}$. In some cases, at long times after the forcing was started, the authors found a piling up of energy at the low wave numbers, further supporting Kraichnan’s theory. They also noted that the individual vortices did not merge together to form a larger vortex, but that small vortices of the same sign orbited each other in groups of vortices.

Later, the same group studied the forward enstrophy cascade, by rearranging their forcing length so that it was comparable to the size of the system [68]. Their energy spectrum in the enstrophy cascade range showed a scaling close to $E(k) \sim k^{-3}$. However, they were not able to obtain an inverse and a forward cascade simultaneously, due to the limited size of their experiment compared to the size of the forcing magnets.

Studies of 2D turbulence in soap films have also recovered the inverse and forward cascades. Rutgers showed that a soap film that was stretched between two wires flowed through a grid, it produced the expected shape of the energy spectrum shown in Fig. 2.2 [75]. This 2D “soap tunnel” is gravity driven, where the driving strength can be varied by changing the vertical tilt of the wires. This setup has been used in other experiments to study the dynamics of 2D turbulence [100, 25], although the validity of the 2D approximation in soap films is questionable. Some

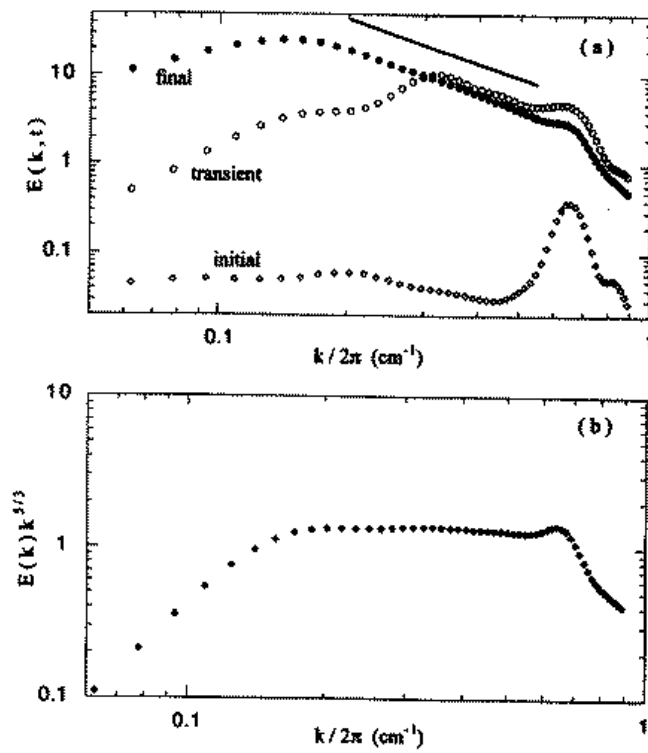


Figure 2.3: Time dependent inverse cascade, from Ref. [69].

critics of soap films claim that thickness variations are too important, while others note that the drag from the air cannot be ignored [14]; hence the problem is really three-dimensional. However, soap films do display many of the features of 2D flows, such as an inverse cascade and the stability of large coherent vortices.

Alternative approaches to the Kraichnan-Batchelor theory do exist for 2D turbulence. In 1971, Saffman [76] proposed an alternative scaling for the forward enstrophy cascade early on. Another notable addition is the work of Gilbert [36, 35] who extended the theory of Lundgren spiral vortices for a 2D flow. The spiral vortex model was introduced by Lundgren in 1982, and refined in 1993 [57]. It models a turbulent flow as a collection of isolated vortices of different ages and sizes which interact with each other. Focusing on one vortex in an initially random field of vortices, the shear experienced by this vortex from the rest of the flow will cause it to stretch, at which point the vorticity from the vortex itself will fold the stretched lobes back in, thus creating a spiral. By using conservation of mass and other physical arguments, Lundgren was able to predict the rate at which the vortex should stretch, and he was able to recover the energy spectrum of 3D turbulence predicted by Kolmogorov.

Gilbert [36] used the same model but forced the vortices to have a zero stretching rate in the axial direction, which is the case for a 2D columnar flow. In this case, the energy spectrum should vary significantly over different parts of the flow and might show discontinuities in k . However, the energy spectrum averaged over many realizations and for sizes much larger than individual spiral vortices should scale as $E(k) \sim k^{-2}$, in contrast with Kraichnan's predicted scaling. No experiments or simulations have yet reported flows consistent with the 2D spiral vortex model, although as we shall see in future chapters, our flows display some of the scaling characteristics.

2.2.2 Self-Similarity and intermittency

We have seen above that 3D turbulence is not self-similar. This is measured by the scaling of the structure function exponents which show a clear departure from the K41 scaling $\zeta_p = p/3$. Another sign of the scale dependence is the shape of the Probability Distribution Functions (PDFs) of the velocity increments $\delta v(\ell)$, which change shape from a stretched exponential at small scales (small ℓ), to Gaussian at large scales [3]. In a velocity time series record, this scale dependence is related to intermittent bursts of high velocity differences. These jumps in velocity are thought to be due to the sweeping by of intense structures by the mean flow, such as thin vortex cores. However, direct simultaneous measurements of the velocity differences and the structures sweeping-by are not yet available.

Since vortices in 2D turbulence cannot stretch in the axial direction, one does not expect 2D turbulence to show scale dependence (or intermittency) in the way that 3D turbulence does. This fact has been verified experimentally by Paret and Tabeling [70] in the inverse cascade regime, by using their stratified flow experiment. Although the error bars in their experiments are large, they measure structure function exponents which scale with p consistently with the K41 prediction $\zeta_p = p/3$ as shown in Fig. 2.4. However, the authors here take care in pointing out that the small vortices in their flows do not merge to create larger vortices, but that instead they orbit each other and form clusters of small structures.

Numerical simulations also support the view of self-similarity in the inverse cascade regime. Early simulations by Siggia and Aref [83] suggested the fact, but later Smith and Yakhot [87] found that intermittency was absent in the initial stages of the flow evolution. Boffetta et al. [12] also studied the scale dependence of the flow in the “inverse cascade regime”, before the onset of large-scale condensation, and found results in agreement with the view that 2D flows are self-similar. Their results show velocity difference statistics that are nearly Gaussian at all scales in

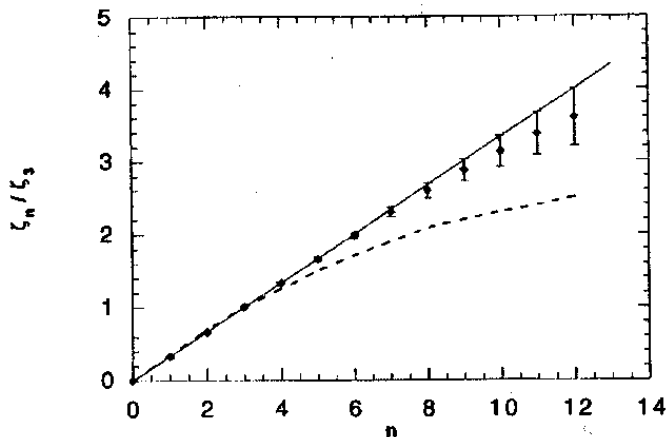


Figure 2.4: Relative structure function exponents from Ref. [70].

the inertial range.

However, the question is not yet settled in the presence of coherent vortices. As we have seen above, 2D turbulence is naturally conducive to the formation of large structures through the inverse cascade. The lack of efficient dissipation at these large scales means that the vortices that form tend to be long-lived, and their presence affects the flow statistics significantly. In addition to affecting the slope of the energy spectrum in the enstrophy-cascade range, the onset of the vortices was found to produce intermittent statistics in Ref. [87]. Furthermore, soap film experiments have measured intermittent statistics, i.e. scaling exponents ζ_p varying nonlinearly with p [100, 25].

The effect of the coherent vortices can be thought of as follows: The turbulent background flow is made up of small scale random fluctuations. Superposed on this background are the coherent structures which contain most of the energy in the system, and which drift around and interact with each other by merging or breaking up. A small vortex in such a flow can get sheared by the circulation of the larger vortices, and such a vorticity patch would be deformed and folded in the plane to add to the small scale, “high frequency”, vorticity background. This has led to the

coining of the expression “laminar drops in a turbulent background” as a way to think of the long-lived vortices [77]. If we imagine placing a hot film probe in the flow and measuring a velocity time series, we would see a switching between the coherent structures and the turbulent background in the time record as the fluid sweeps by. This switching might be scale-dependent, since the statistics in the vortices can be very different from those in the background.

Some numerical simulations support the above picture of coherent structures in 2D turbulence [47, 61, 87]. The issue of self-similarity and intermittency has not been addressed for a flow which has a clear distinction between long-lived large structures and small scale turbulence. The study of such a system will be one of the main contributions of this thesis.

2.3 Rotating flows

At this point, we take a step away from turbulence to look at the necessary background on rotating flows. Over the years, several experiments have studied rotating fluids, some looking to understand specific geophysical situations, while others attempting to answer basic questions about the fluid dynamics. A famous example of the first type is the large (14 m diameter) rotating Coriolis-tank in Grenoble (France), which was originally built in the late 1960s to model tidal flows in the English channel⁵. Below, we will concentrate on the experiments investigating basic fluid dynamics questions.

Perhaps the most intriguing principle in rotating fluid dynamics can be summarized by the Taylor-Proudman theorem. This theorem states that in a rotating flow, the velocity derivatives vanish in the direction parallel to the axis of rotation for fast rotation. We sketch the derivation of the theorem in the next section, followed in Subsection 2.3.2 by a discussion of other aspects of rotating flow experiments.

⁵see <http://www.Coriolis-legi.org/default.htm> for more information on this experiment.

Specially, we introduce the Beta-plane approximation used in many geophysically-motivated experiments.

2.3.1 Taylor-Proudman theorem

The Taylor-Proudman theorem is described in detail in many textbooks (see e.g. [38, 71, 96, 53]) and can be derived as follows. We start with the Navier-Stokes equations in a rotating frame, which includes the Coriolis ($-2\boldsymbol{\Omega} \times \mathbf{u}$) and centripetal ($-\boldsymbol{\Omega} \times (\boldsymbol{\Omega} \times \mathbf{r})$) force terms,

$$\frac{\partial \mathbf{u}}{\partial t} + \mathbf{u} \cdot \nabla \mathbf{u} = -\frac{1}{\rho} \nabla p + \nu \nabla^2 \mathbf{u} - 2\boldsymbol{\Omega} \times \mathbf{u} - \boldsymbol{\Omega} \times (\boldsymbol{\Omega} \times \mathbf{r}). \quad (2.21)$$

The centripetal force term can be rewritten as a potential, $\boldsymbol{\Omega} \times (\boldsymbol{\Omega} \times \mathbf{r}) = (1/2)\nabla|\Omega^2 r^2|$, thus allowing us to combined it with the pressure term, yielding an *effective* pressure ($p_{eff} = p + |\Omega^2 r^2|$).

Next, we non-dimensionalize Eq. 2.21. By using characteristic dimensions L for length, U for velocity, L/U for time, and a characteristic pressure P , we obtain

$$\frac{U}{2\Omega L} \frac{D\mathbf{u}^*}{Dt^*} = \frac{-P}{2\rho UL\Omega} \nabla^* p^* + \frac{\nu}{2\Omega L^2} \nabla^{*2} \mathbf{u}^* - \hat{z} \times \mathbf{u}^*, \quad (2.22)$$

where the starred variables are dimensionless. Here, the standard notation is used for $\frac{D}{Dt}$ for the material derivative [67].

It is useful to define the following dimensionless numbers, taken from the above equation. First, the Rossby number is defined as $Ro = U/(2\Omega L)$; it compares the importance of inertial effects to Coriolis effects. $Ro \gg 1$ means that the rotation is not important, while $Ro \ll 1$ means that the flow is rotation-dominated. For example, even though at one revolution per day the earth is turning slowly, the characteristic lengths in the atmosphere make the Coriolis effects important; the Rossby number is approximately 0.1 in both the atmospheric jet stream and the

Gulf stream. In our experiment, we compensate for the small size of our setup by rotating rapidly, up to three revolutions per second.

The Ekman number, defined as $Ek = \frac{\nu}{2L^2\Omega}$, compares the effect of viscosity to that of rotation. A small Ek means that viscous effects are not important in the flow. On a typical geophysical scale, the Ekman number is often smaller than 10^{-9} , which is not achievable in a laboratory experiment. However, an Ekman number of 10^{-5} is typical in the lab, meaning that the viscous effects are indeed negligible.

Related to the Ekman number is the Ekman spin-down time, defined as $\tau_{Ek} = h_0/2(\nu\Omega)^{1/2} = Ek^{-1/2}\Omega^{-1}$. If the tank rotation rate is varied with no other forcing, the flow would exponentially reach solid body rotation with characteristic time τ_{Ek} . More generally, the Ekman spin-down time is a measure of how soon the bulk of the flow will feel a change in the top and bottom boundary conditions. For a rapidly rotating tank, this time scale is typically orders of magnitude faster than the diffusive time, due to the advection of bulk fluid through the Ekman boundary layer. This mixing between the boundary layer and the bulk is known as Ekman pumping.

In the limit of small Ro and Ek , Eq. 2.22 simplifies to

$$2\Omega \times \mathbf{u} = -\frac{1}{\rho}\nabla p \quad (2.23)$$

which is known as the geostrophic equation. From this equation, we can show that a rotating flow becomes 2D as follows: First, take the curl of both sides of the equation, which yields

$$\nabla \times (\Omega \times \mathbf{u}) = 0. \quad (2.24)$$

By expanding the above equation and invoking incompressibility and continuity ($\nabla \cdot \mathbf{u} = 0$), the different terms can be discarded, and we are left with

$$\Omega \cdot \nabla \mathbf{u} = 0 \tag{2.25}$$

which says that the derivative of the velocity vanishes in the direction of Ω . In other words, if $\Omega = \Omega \cdot \hat{z}$, then $\partial \mathbf{u} / \partial z = 0$. This is the Taylor-Proudman result, which states that *in the limit of high rotation, the velocity derivatives vanish in the direction of the rotation axis*. If in addition we have solid boundaries, then the velocity in the \hat{z} -direction vanishes everywhere. Note that Eq. (2.25) is a constraint on the motion, not an evolution equation. The flow solution $\mathbf{u}(\mathbf{r}, \mathbf{t})$ is still given by the solving the full 3D equation of Eq. (2.21).

The applicability of the Taylor-Proudman theorem is questionable for the case of turbulent flow, since the theorem's derivation ignores both the time derivative and the nonlinear terms in the Navier-Stokes equation. In other words, the geostrophic equation (Eq. 2.23) is simply a balance between the Coriolis and pressure terms, and cannot describe the evolution of the flow field in time, or the turbulent energy cascade which is due explicitly to the nonlinear terms. However, the two-dimensionalization of a turbulent flow through rotation has been demonstrated experimentally and numerically as discussed below.

Finally, we introduce one more parameter that is relevant to rotating flows. The Rossby number, as defined above, is a macroscopic measure of the importance of rotation on the flow; we will refer to it as the global Rossby number, Ro_g . An alternative definition is the local Rossby number, $Ro_l = \omega / 2\Omega$, which is a function of the local vorticity ω . For a given vortex in a rotating flow, this number tests the strength of the vortex rotation rate compared to the rotation rate of the system. In other words, will the Coriolis effects from the vortex rotation be stronger or weaker than those from the rotation of the system?

The local Rossby number can also be thought of as a ratio of time scales, where the rotation period Ω^{-1} is compared with the vortex turnover time ω^{-1} . With

the availability of complete vorticity fields through computer advances in simulations and experiments, one can make use of the local Rossby number which does not involve the subjective choice of a length and velocity scales.

Therefore, three time scales are important in characterizing a rotating flow. They are the rotation rate of the system, the vortex turnover time, and the Ekman time. For flow to be 2D, these time scales need to be strongly separated, with the relation

$$\tau_{Ek} \gg \omega^{-1} \gg \Omega^{-1}. \quad (2.26)$$

This relation is satisfied in our experiment by design. The height of the tank was designed such that the Ekman time is around 80 s, always large compared to the period of rotation of the tank, which is on the order of 1 s. Finally, a Rossby number of 0.1 means that the turnover time for the vortices is around 10 s, well separated from both τ_{Ek} and Ω^{-1} .

2.3.2 Potential vorticity

We now turn our attention to a different aspect of rotating flow experiments, especially those that model geophysical flows. In a geophysical context, the potential vorticity is a conserved quantity that plays a central role [71]. This quantity consists of the local vorticity of the flow plus the local Coriolis effect from the planetary rotation, which varies with latitude. The potential vorticity q on a spherical planet can be written as

$$q = \omega + f = \omega + 2\Omega \sin \theta, \quad (2.27)$$

where ω is the local vorticity of the fluid, Ω is the rotation rate of the planet, and θ is the latitude. The parameter $f = 2\Omega \sin \theta$ is called the Coriolis parameter.

In many geophysical experiments, one is interested in modeling the flow near a certain latitude. By Taylor expanding Eq. 2.27 near a latitude θ_0 , and recalling that $\sin \theta \simeq \sin \theta_0 + (\cos \theta_0)y/R$, where $y = (\theta - \theta_0)/R$ is the distance north of the reference latitude and R is the radius of the planet, The equation for the potential vorticity then becomes

$$q = \omega + 2\Omega.\theta_0 + \beta y + H.O.T., \quad (2.28)$$

where $\beta = 2\Omega \cos \theta_0/R$ is a constant. From Eq. (2.28), it can be shown that the variation of the Coriolis parameter f with latitude can be modeled to first order by a linear variation of the height of the rotating system, with a slope β [71]. This approximation is known as the “Beta-plane” approximation. Conservation of potential vorticity then implies that a vortex which travels in the direction of increasing y must reduce its vorticity in order to conserve its potential vorticity, and vice versa.

A sloped bottom has been used in many experiments to model the variation of Coriolis parameter with latitude. This beta plane also introduces a new length scale into the problem, the Rhines length [74],

$$\lambda_\beta = (Uh_0/s\Omega)^{1/2}, \quad (2.29)$$

where h_0 is the mean height of the tank. For laminar flows, this is the length at which the sloped bottom effects become important, causing the existence of the so-called “barotropic instability” in the flow [89]. In turbulent flows, the significance of the Rhines length is a matter of some controversy. Shepherd [82] states the generally accepted view that the inverse cascade in a rotating flow stops at the Rhines length, and energy that builds up at this length is radiated in the form of inertial Rossby waves, rather than continuing to cascade up in the traditional manner.

2.4 Is rotating turbulence two-dimensional?

In this section, we start by giving an overview of the rotating turbulence experiments, of which none have been reported recently. Afterwards, we turn our attention to forced 3D rotating flow simulations. In all of the discussion below, we avoid studies of decaying turbulence, for the reasons discussed above for 2D turbulence. Furthermore, experiments on decaying turbulence are mainly concerned with rates of decay and the emergence of anisotropy, issues that do not concern us in the forced case.

2.4.1 Experimental verifications

Two review articles [95, 39] discuss laboratory experiments on rotating turbulent flows that were conducted up to the mid-1980's. The focus in both articles is largely on the two-dimensionalization of 3D turbulence, and on experiments aimed at understanding the basic dynamics of turbulent motion, rather than modeling complex geophysical or engineering applications. Hopfinger reverts to the Taylor-Proudman theorem to argue that *any fluid motion will tend towards a two-dimensional state* in the limit of small Rossby and Ekman numbers [39]. He notes further that for rotation-dominated (low Ro) turbulence to survive, the vortex turnover time must be much faster than the Ekman time τ_{Ek} , which is equivalent to saying that

$$Ek^{1/2} \ll Ro_g. \tag{2.30}$$

Note however that the turnover time for vortices must still be slow compared to the rotation rate of the tank, which is equivalent to requiring a low Rossby number (Ro_l).

The experiments reported in these review articles can be divided into several

types: decaying turbulence experiments [44, 46], oscillating grid turbulence [41, 26], homogeneous source-sink flows [59, 23], and rotating shear flows [95].

In the decaying experiments, Ibbetson and Tritton [44] did not satisfy the inequality in 2.30, and found the turbulence to decay much faster under rotation. On the other hand, Jacquin *et al.* [46] found a slowdown of the energy dissipation due to rotation, and strong anisotropic effects where longitudinal scales are nearly unaffected by the rotation while the transverse scales grow significantly [45].

Oscillating grid experiments aim to study the effects of rotation on otherwise homogeneous turbulence. Dickinson and Long [26] concentrated on the propagation of the turbulent front after the grid oscillation was started, as a function of the rotation rate of the tank. Hopfinger and his co-workers [42, 40, 41] looked at the dynamics of the turbulence in the steady state, long after the grid was set in motion. Both groups found a region near the grid that was fully 3D, unaffected by the tank rotation, and a region far from the grid that was populated by long-lived 2D vortices. The main result of these experiments in the current context is that far from the grid, the flow becomes 2D even in the highly disordered (turbulent) case. The vortices that are formed in these flows are columnar with a much larger length scale in the direction of rotation than in the perpendicular plane.

The vortex dynamics in a plane perpendicular to the rotation are discussed in Hopfinger *et al.* [41]. The authors note the presence of long-lived columnar vortices, contrary to 3D turbulence where vortices typically decay after one turnover time. Furthermore, they note the predominance of cyclonic structures, pointing to a significant effect of the rotation. The size distribution of vortices is related to the forcing and rotation rates, with the higher rotation rate vortices being smaller, displaying a certain “locking” to the size of the forcing grid. This suggests that the effect of rotation reaches the area near the grid as the rotation rate is increased. Finally, the authors also present flow visualizations along a vertical cross section,

using small bubbles to track the vortex cores. These cores are found to be extremely thin (1-2 mm) compared to their length (~ 30 cm).

The source-sink flows of McEwan [59] and Colin de Verdière [23] use an array of sources and sinks in the bottom of a rotating cylinder to generate geostrophic vortices. The two experiments differ in their operating Reynolds and Rossby numbers, with the latter corresponding more closely to the range of our experiments. McEwan [59] includes streak photos which show very clearly the difference between the rotating and non-rotating cases: The non-rotating case consists of a random motion of particles, while the rotating flow displays well defined coherent vortices. These coherent structures persist in Colin de Verdière’s paper, which notes that small scale vortices are initially formed which then merge to create larger ones, in an inverse cascade similar to Hopfinger’s experiments. Reference [23] also includes an extensive discussion of the effect of different beta-planes (sloped bottoms) on the flow, in the forced and decaying cases. The author finds the formation of a broad counter-rotating zonal jet, surrounded by cyclonic vortices, in the case of a “polar” beta-plane.

Finally, a free shear flow under rotation was discussed by Tritton [95]. The rotation was found to stabilize (destabilize) vortical structures if the sign of the shear is the same (opposite) as the sign of rotation. Vortices created in “cyclonic” shear would have a 2D structure and survive over long times, whereas anti-cyclonic vortices would decay and display 3D motions.

The above experiments have shown that rotation can two-dimensionalize a 3D turbulent flow as the Rossby number becomes small. They show that even with forcing in the third direction, the rotation aligns the vortex tubes with the axis of rotation. The shortcoming of the previous work is that much of it is qualitative, using methods such as streak photography or dye injection to characterize the flow large coherent structures in the flow. The computerization of our experiment allows

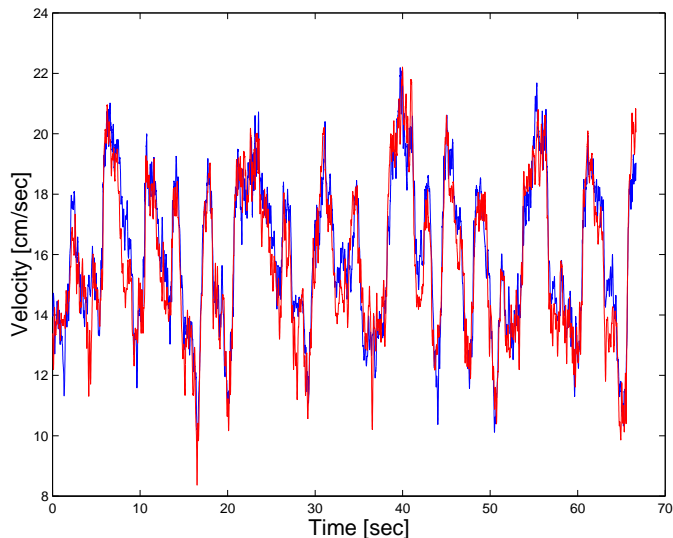


Figure 2.5: Velocity signal from two vertically separated probes, showing a correlation of 0.9 across a distance of 18 cm. $\Omega/2\pi = 2.5$ Hz, $Q = 150\text{cm}^3/\text{s}$.

us to explore the details of the turbulent motion in ways that were not accessible previously.

In particular, we are able to obtain very long time series of the turbulent flow, as well as quantitative instantaneous velocity fields. We see evidence of two-dimensionalization in our flow by comparing the signals from two simultaneous probes, the first one near the top of the tank and the second near the bottom (Fig. 2.5). The two probes are separated vertically by approximately 18 cm, but they are at the same radial and azimuthal location. The time series from the two probes match up very well, especially in the large scale fluctuations. Even some of the detailed small scales are found to correspond in the top and bottom probes, giving the two series of Fig. 2.5 a cross-correlation coefficient of 0.9.

2.4.2 Theoretical and numerical studies of rotating flows

Strong interest in rotating forced turbulence has resurfaced recently in numerical simulations and theory. Below are some of the most relevant publications, starting with numerical simulations:

Hossain [43] started with a fully 3D turbulent flow in a triply periodic box. Using this computed field as the initial value, he “switched on” the rotation and observed a transition to an quasi-2D state: Slices at different axial positions showed high correlation with each other, and the energy spectrum showed a quenching of the forward cascade.

Cambon, Mansour and Godeferd [15] and Godeferd and Lollini [37] simulated a system very similar to Hopfinger’s experiments, with emphasis on Eddy-Dominated-Quasi-Normal-Markovian (E.D.Q.N.M.) closure theory. They were limited to low Reynolds numbers however, due to computational costs of simulating a 3D flow. Within that limitation, they largely reproduced Hopfinger’s results in terms of length scales as a function of rotation rate and forcing rate. In [15], the authors make a distinction between the Local vs. global Rossby numbers defined above. They find that in order for the fluid to become two-dimensional, the flow must simultaneously satisfy $Ro_g < 1$ and $Ro_l > 1$. They argue that the mechanism for two-dimensionalization is due to the propagation of internal waves in the flow, and those waves are damped out when the Ro_l becomes smaller than one, i.e. when the rotation becomes too strong.

Smith and Waleffe [85] (see also [84]) studied the effect of rotation on turbulent flow with 3D forcing. Their simulations are in a triply-periodic rotating box, but with 3D forcing (it is not clear from the paper what the exact forcing is). The rotation forces the initially 3D flow to become *2-dimensional, 2-component*: Not only do the velocity derivatives vanish in the direction parallel to the rotation axis, so do the actual velocities. They note that the energy does flow in an inverse cas-

cade to larger scales even from 3D forcing. However, they find the large scale energy spectrum to scale like k^{-3} rather than $k^{-5/3}$, suggesting that the slope of the energy spectrum might not be universal.

Finally, Lesieur *et al.* (see e.g. Bartello, Métais and Lesieur [4]) have run DNS and LES simulations of flow in a doubly-periodic rotating channel with side-walls. They find that the rotation does two-dimensionalize the 3D flow, although the time required for the two-dimensionalization is very long, scaling as Ro^{-1} .

As for theoretical work, two recent lines of work are notable. First, Zhou [105] notes the need for new length and time scales in the spectral analysis once rotation is introduced. In particular, he notes the need for a rotation time scale $\tau_\Omega \equiv 1/\Omega$ where Ω is the rotation rate. That time scale is to be compared with the scale for nonlinear interactions, $\tau_{nl}(k) \equiv [k^3 E(k)]^{-1/2}$. This ratio of times scales τ_{nl}/τ_Ω is essentially a Rossby number equivalent to Ro_l in our notation, though Zhou does not state it explicitly. The author obtains a new scaling of the energy spectrum for low Ro , $E(k) \sim C_\Omega(\Omega\langle\varepsilon\rangle)^{1/2}k^{-2}$, where C_Ω is a constant. Later, Yeung and Zhou [104] recover a k^{-2} spectrum for some (but not all) rotation rates in numerical simulations.

The second theoretical line is from Canuto and Dubovikov [16], who developed a set of equations describing fully developed turbulence based on Renormalization Group Theory, then applied these equations to series of “standard” problems. In particular, they applied their theory to rotating 3D flows by introducing Coriolis effects. Their conclusions, best summarized in [18] (see also [17]), are similar in spirit to those of Cambon *et al.* [15]. They too make the distinction between the global and local Rossby numbers, and they propose a new number ($N = K/\nu\Omega$ where K is the kinetic energy, $K \sim \frac{1}{2}u^2$), for determining whether rotation will two-dimensionalize a 3D flow. In our notation, this “new” number can be re-written as $N = Ro_g^2/Ek$, and their condition $N < 1$ can be re-written as $Ek < Ro_g^2$. This

condition was already stated in 1989 by Hopfinger [39], when he said that *“for turbulence with high rotation effects to survive, the Ekman spin-down time [...] must be considerably larger than the turn-over time of the energy containing eddies [...], giving the requirement $Ek^{1/2} \ll Ro.$ ”*

We will see in the next chapter that this condition is always satisfied in our experiment by design [89]. Our Ekman time is always large compared with the turnover time of the vortices (ω^{-1}), and we never reach the very high rotation rates necessary for the nonlinear two-dimensionalization mechanisms to disappear.

Canuto and Dubovikov also obtain a steeper slope for the energy spectrum of rotating turbulence. They predict that as the flow becomes 2D, the Kolmogorov energy cascade is inhibited and the energy scales as $E(k) \sim k^{-2}$ instead of the Kolmogorov scaling of $k^{-5/3}$. The relationship between this result and Zhou’s very similar result is not clear; the authors have submitted comments attacking each other’s work, and pointing differences and similarities. However, it is important to note here that these authors are interested in the energy cascade from low k to high k , i.e. the forward cascade, contrary to the typical numerical simulations where authors were specifically searching for an inverse energy cascade.

The current consensus among theorists and numericists appears to be that rotating turbulence becomes quasi-2D due to the effect of nonlinear inertial waves, and not by the Taylor-Proudman theorem. This is important in cases where the rotation is so strong that it suppresses all nonlinearities, such that an initially 3D flow would remain 3D. However, these rotation rates are well beyond the operating range of our experiment, meaning that we should expect a quasi-2D flow to form at the highest rotation rates achievable.

The relation between rotating quasi-2D turbulence and the idealized case in Kraichnan’s theory is complicated. For instance, the scaling of the energy spectrum often shows different slopes in simulations from the expected $k^{-5/3}$ as discussed

above. However, it is widely accepted that the rotation aligns the vortical structures and prevents vortex stretching and folding from occurring. The dynamics of the vortex interactions are therefore well described by 2D hydrodynamics, supporting previous experimental work. In most of the simulations quoted above, the authors deal with idealized conditions such as homogeneous isotropic flow, or flows where boundary effects are ignored. The lack of Ekman pumping in these simulations makes the relation with experimental rotating flows tenuous, since the Ekman layer and Ekman pumping are the main mechanisms through which energy is dissipated in a system such as ours. Therefore, one should be careful when comparing the above simulations with experimental studies.

For these reasons, it is difficult to draw a direct comparison between our experiments and the theoretical work previously done. However, there is strong experimental and theoretical evidence that in the range of parameters of interest to us, rotation does two-dimensionalize an initially 3D flow.

I will end the literature review with a quote from the first chapter of Batchelor's 1953 monograph [5]. He states: "*There are very many isolated papers and incomplete lines of research which cannot appropriately be mentioned here but will find a place in later chapters.*" Since the publication of Batchelor's book, many more papers have appeared on turbulence and rotating flows; this chapter does not attempt to cover the whole subject, but the main relevant ideas have been presented. Other works will be cited in future chapters as they become relevant to our study.

2.5 Summary

In this chapter, we started by establishing the basic ideas of the 1941 Kolmogorov theory. These ideas can be summarized by the scale-independent energy cascade, which transfers energy without loss from the injection scale to the dissipation scale. The steady state energy spectrum is predicted to follow the form

$E(k) \sim k^{-5/3}$. The self-similarity of the cascade gives rise to a power-law scaling of the structure functions $S_p = \langle [\delta v(\ell)]^p \rangle \sim \ell^{\zeta_p}$, where $\zeta_p = p/3$ in the case of a Kolmogorov-type flow. Measurements in 3D turbulence experiments recover the energy scaling, but display significant deviations in the case of the structure function scaling exponent ζ_p , with the experimentally measured values of ζ_p displaying nonlinear dependence on p . In future chapters, we will test these scalings to show that our low-rotation flows correspond to 3D turbulent flows.

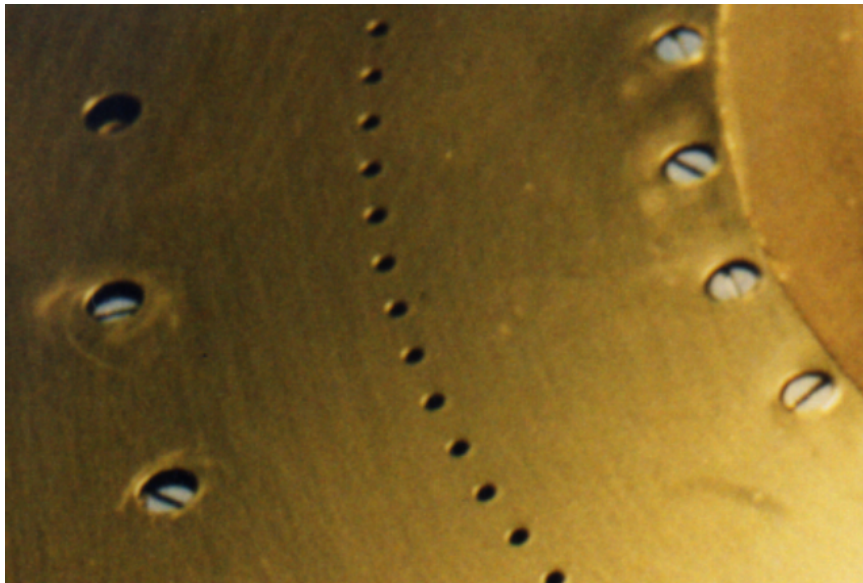
Two-dimensional turbulence is expected to have a self-similar inverse cascade, where energy is transferred to larger scales from the injection scale. This cascade has been verified numerically and experimentally, and is found in some cases to lead to the formation of large stable vortices which contain most of the energy in the flow. The self-similarity has been verified in the transient case, before the cascade has reached the largest scale allowable by the system size. However, no measurements have been made on the scaling of the structure functions in the steady state case. We will fill this void in our study of the 2D flows in Chapter 5.

Finally, we show that rotation produces quasi-2D flows in laminar as well as turbulent flows. The two-dimensionality depends on the rotation rate, as measured by the Rossby number. This section mainly justifies our expectation that our flows will be two-dimensional, but also shows that much remains to be explored in studying rotating 2D turbulence.

The next chapter describes the experimental apparatus. The automation of our setup, which sets this experiment apart from previous rotating experiments, will also be described with its advantages and limitations. Once the theory and the experimental capabilities are introduced, we will then be able to address the scientific questions in the later chapters.

Chapter 3

Experimental Apparatus



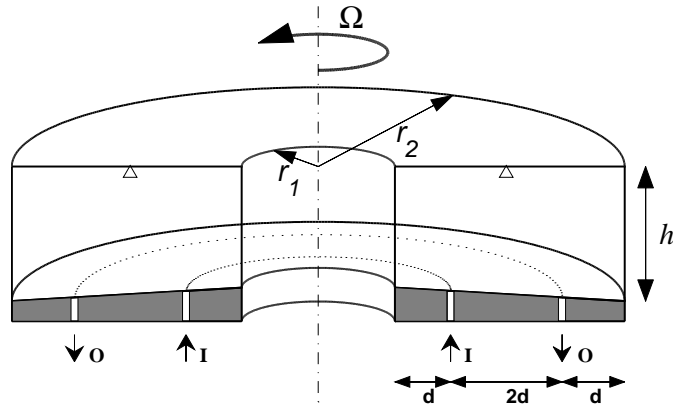


Figure 3.1: Schematic representation of the experiment. $r_1 = 10.8$ cm, $r_2 = 43.2$ cm, $d = 8.1$ cm, and $h = 20.3$ cm at r_2 and 17.8 cm at r_1 . I marks the flow into the tank, and O is the outflow. The hot-film probes are marked with the \triangle .

With the theory of rotating turbulence now in hand, we will proceed to test some of the theoretical and numerical predictions experimentally. The experiments described in the upcoming chapters are run in a rotating tank filled with distilled water, with a flat rigid lid and a sloping bottom. The tank, shown schematically in Fig. 3.1, can rotate at rates upwards of 20 rad/s. An azimuthal jet is generated by pumping water in a closed circuit through two rings of holes at the bottom of the annular channel. Pumping into the tank through an inner ring and out through an outer ring produces a net outward flux. This flux couples with the Coriolis force to generate a counter-rotating jet; it is the dynamics of this jet as a function of rotation and pumping rates that will be of interest to us.

One of the contributions of this work is to combine the use of the two types of measurements to explain the dynamics of the strong coherent structures in turbulent flows. The first type is hot-film (hot-film) anemometry, which provides an Eulerian velocity measurement. The second is Particle Image Velocimetry (PIV)

which provides snapshots of the complete 2D velocity field.

There are therefore two **control parameters**:

- Rotation rate
- Pumping rate

and two **measurement methods**:

- hot-film anemometry
- Visualization system.

A schematic of the different components (to scale) is shown in Fig. 3.2. All the rotating parts can be seen in this figure, including the rotating computer and camera system. A more functional view can be seen in the graphical block diagram of Fig. 3.3, which shows the interactions of the different subsystems. As noted in the previous chapter, the level of instrumentation and the use of computers on this experiment are what set it apart from the previous experimental works on rotating turbulence (e.g. Hopfinger et al. [39]). This is partly due to the computing power available to us today, but also to the emergence of new, more quantitative ideas in turbulence theory that can be tested experimentally.

This chapter introduces each of the above subsystems, starting with an overview of the rotating tank and the rotation control. In Section 3.2, the pumping and pump control systems are described. The bulk of the chapter will be spent on the measurement techniques, starting with the hot-film system and calibration issues in section 3.3, and ending with the PIV system. We end with a summary.

3.1 The rotating tank

This apparatus is the product of many years and several generations of researchers' efforts. It was originally built with the specific purpose of reproducing

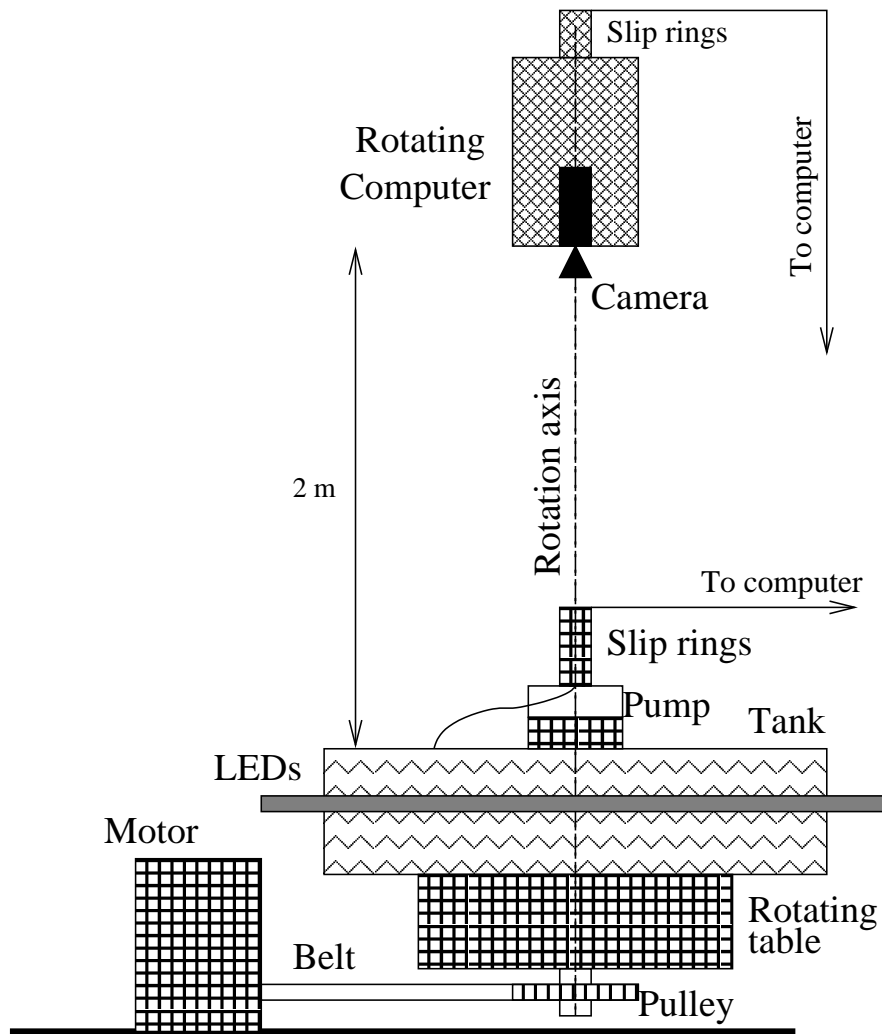


Figure 3.2: Schematic of the different instrumentation components.

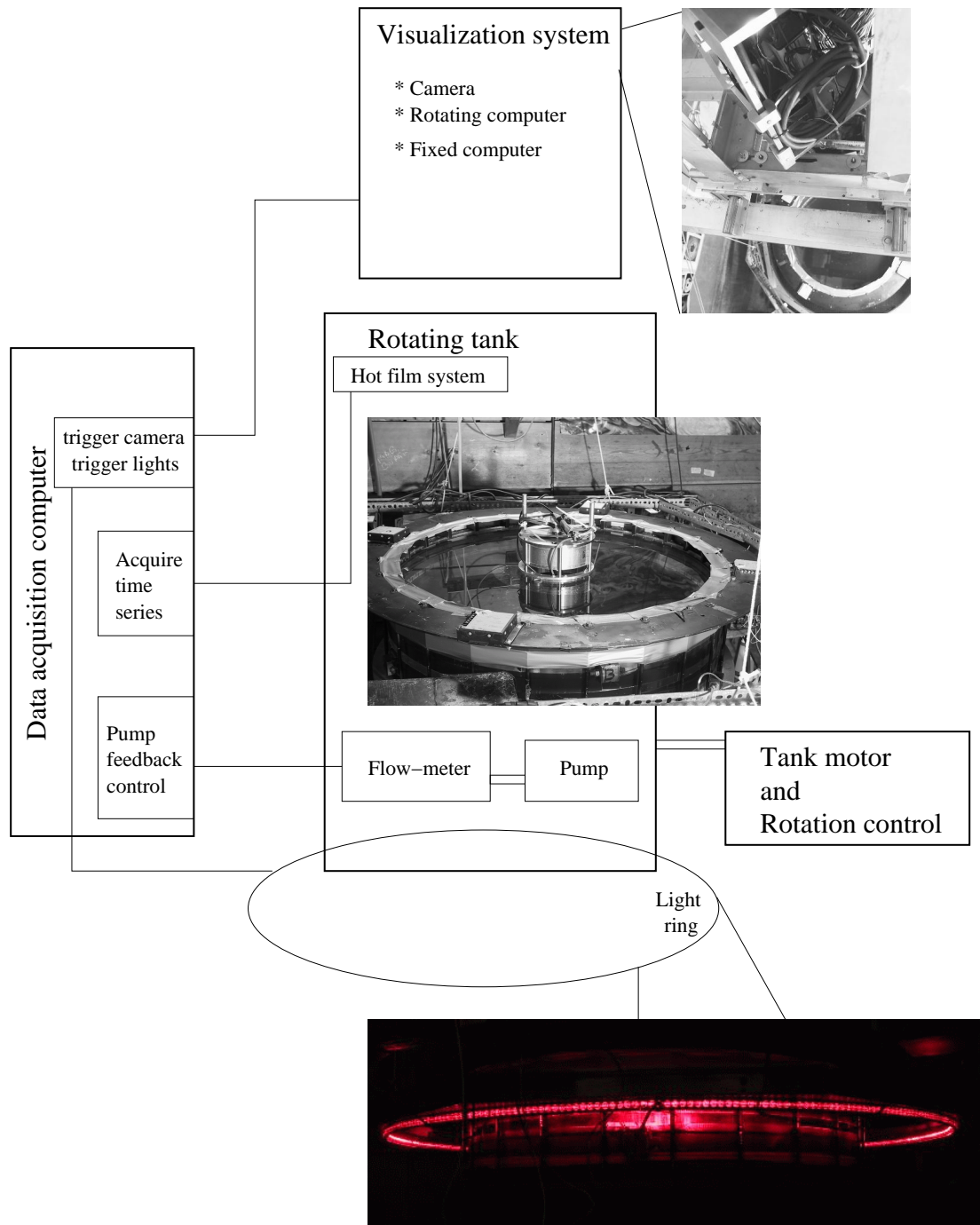


Figure 3.3: Block diagram of the experimental subsystems.

the large coherent spots of Jupiter in a laboratory setting, and the early results were published in 1988 [90]. Since then, several additions and major changes have taken place, largely in order to extend the range of possible measurements but also to improve the control of the experimental parameters. In this chapter we concentrate on the newest upgrades, which were done between early 1997 and late 1999. The previous system is described in detail in E. Weeks's dissertation [101], and the original version is in S. Meyers's dissertation [64].

The tank consists of an annular channel with a metal cylinder as the inside wall ($r_1 = 10.8$ cm) and an outside wall made of transparent acrylic ($r_2 = 43.2$ cm), as shown schematically in Fig. 3.4. Both walls are screwed into an anodized aluminum bottom plate, and a transparent acrylic lid screws on the top of the walls. The surfaces of the lid are made parallel to about 1/1000th inch, then re-polished, in order to minimize the visual distortion of particle motions. The pumping is done through three forcing channels cut in the bottom plate, shown in Fig. 3.5(right). The bottom plate is covered with a black conical plate which contains the small forcing holes, also shown in Fig. 3.5(left). The screw holes are covered with black silicone glue to make the bottom smooth. The forcing holes are arranged in three concentric rings, which fit above the forcing channels in the bottom plate. All the data in this thesis were taken with forcing through the inner and outer plates; the middle ring was unused during this study.

The tank is supported from below by a central shaft, which sits on two thrust bearings and is connected at the bottom to a toothed pulley. This pulley is coupled through a synchronous (timing) belt to the drive motor, with a speed ratio of 1-to-4. The motor system is a *Compumotor I-320*, obsolete since 1989. It consists of a Pulsed Width Modulated (PWM) AC servo motor, with a controller using rotation-rate feedback control directly on the motor shaft. The details of the controller are not available, since the documentation for the system is lost. The rotation rate is

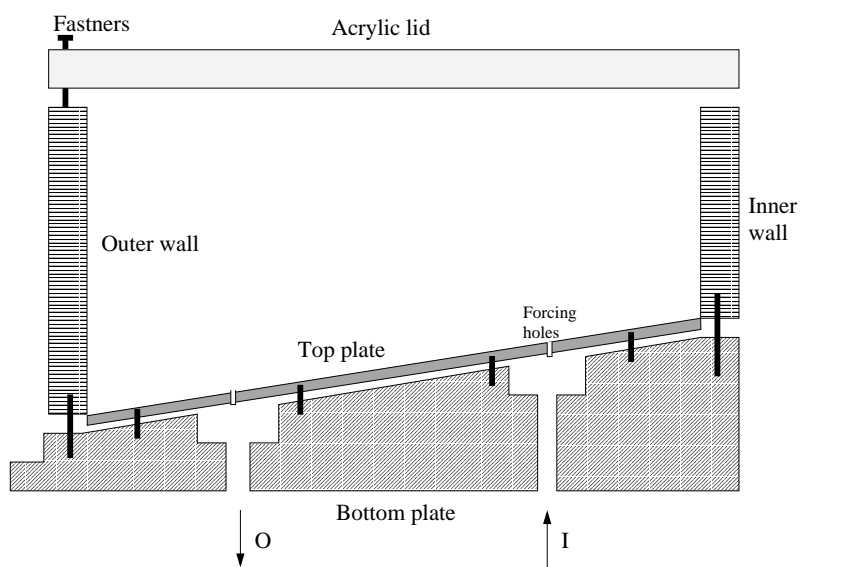


Figure 3.4: Exploded view of the water channel (not to scale). Here, only the inner and outer forcing channels are shown, without the central one.

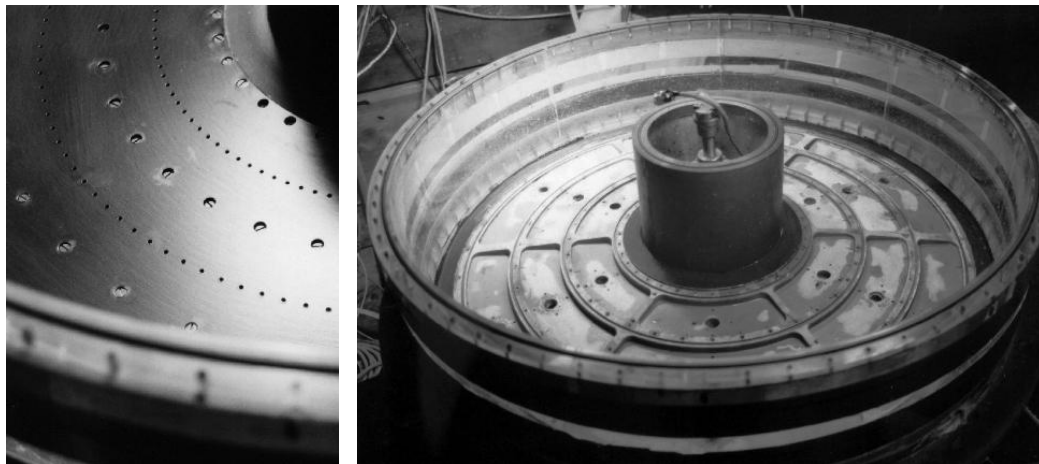


Figure 3.5: Photograph of the tank showing the bottom plate during cleanup (right), and the top plate with the forcing holes visible (left).

set through an analog indexer which has a resolution of 1/2046 Hz.

The camera is rotated by a Compumotor stepper motor with no gearing. The rotation rate is controlled by a similar indexer as the tank, but the resolution there is 1/500 Hz. Because the conversion factor on the tank indexer is not divisible by 4, the tank and camera rotation rates in our experiments sometimes differ by $\delta\Omega = 2.4 \times 10^{-4}$ Hz, or 0.015 rpm (e.g. at 1/4 Hz rotation). This difference in rotation rate is noticeable when following the motion of the tank for several minutes, but the relative error introduced into the velocity measurements is only on the order of $\delta\Omega$.

Two sets of slip-rings are available to transfer electrical power and signals on and off the rotating tank. These slip rings are used to power the pump and measure pumping rate, as well as to power and transmit the hot-film signal. Getting noise-free signal from the hot-film probes is essential for the study, and the newer set of rings provides two shielded channels with co-axial connections. These slip rings are rated for up to radio frequencies, which far exceeds our needs for the hot-film signal.

The rotation rate of the tank was found to oscillate around the required value. Evidence of this oscillation is found in the signal from a rotary encoder that measures the tank rotation rate, but mainly in the velocity measured by the hot-film probes. For example, a frequency spectrum of a velocity time series from the hot-film probes shows sharp peaks at the rotation frequency and its harmonics. The fluctuations seem to depend on the rotation rate of the tank; they are stronger at the lowest rotation rates, and they weaken as the speed is increased.

This problem has been known for some time, but a solution to it is not available. A tensioner pulley was added on the driving belt in order to reduce backlash effects; it was found to slightly improve the accuracy at the low rotation rates. It has been suggested that the motor and the tank need to be impedance-matched by connecting a fly-wheel on the motor shaft [64]. This solution was contemplated, but

the space around the motor would need to be re-designed. Also, the motor is often running at the low end of its operating range, and a higher gearing might be useful to allow the motor to respond with more precise velocity adjustments.

We can estimate the error induced from this variation as follows, since the probes are rigidly mounted to the tank: As the tank rotates at a nominal rate of Ω , the true rate might have the form $\Omega + \Delta\Omega(t)$ where $\Delta\Omega(t)$ is the oscillation in rotation rate as a function of time. Let us suppose that $\Delta\Omega(t) = \Omega_\epsilon \sin(ft)$ where Ω_ϵ is the maximum amplitude and f is the frequency of the variations. The effect of the variations on the fluid flow is negligible as long as the frequency of the variations f is high compared to the inverse of the Ekman time ($1/\tau_{Ek}$); in the experiments discussed here, f is in the range of a few cycles/second, while τ_{Ek} is always larger than 80 s, meaning that $1/\tau_{Ek} < 0.01$ Hz. Therefore as the rotation rate varies, the probe is being dragged through the water at some rate, and this will be measured as a spurious velocity. The corresponding velocity can be calculated as

$$v_\epsilon = \Omega_\epsilon r_{\text{probe}} \tag{3.1}$$

where $r_{\text{probe}} = 27$ cm in this case. This implies that a value of $\Omega_\epsilon = 0.01 \times 2\pi$ rad/s (or 0.01 Hz) would correspond to an error velocity $v_\epsilon = 1.7$ cm/s! This would suggest that we need to control the rotation rate to better than 0.01 Hz if we wish to obtain velocity measurements more accurate than 10% in the range of velocities of interest to us.

However, the real error is not as large as it seems at first glance. The tank, which weighs more than 200 kg when filled, itself acts as a fly-wheel which resists fast changes in rotation rate. Once the initial acceleration period is over, the rotation rate is stabilized by the tank, and the motor simply works to overcome the constant friction from the bearings and air drag. Since this inertial effect is weaker in the low-rotation case, it places a lower bound on the rates at which we can run

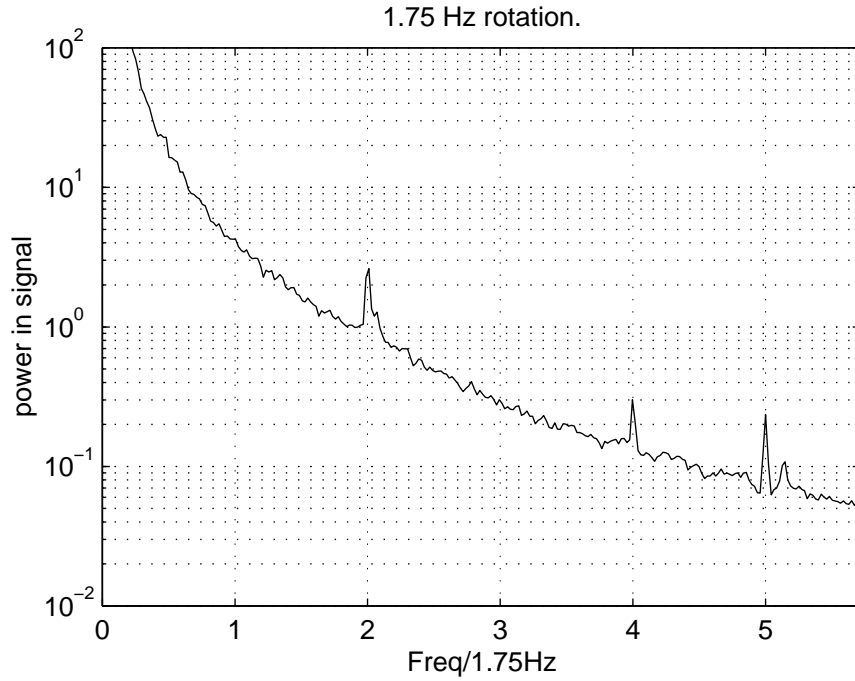


Figure 3.6: Frequency spectrum of velocity time-series showing peaks at the harmonics of the rotation rate; the horizontal axis was re-scaled by the rotation rate.

the experiment. The hot-film data shown in this work are all for $\Omega > 1.57$ rad/s (1/4 Hz). PIV data does not suffer from the same errors, and was taken down to 1/8 Hz.

Furthermore, the fluctuations that we observe in the time series due to the rotation rate are easily removed. As shown in Fig. 3.6 for the fast rotation case, they appear at exact multiples of the rotation rate in a frequency spectrum. Since their effect is very localized in frequency, these errors should not to affect regions of power-law scaling that we are searching for in this study.

3.2 The pumping system

The heart of the pumping system is a Moyno (model 34401) positive displacement screw pump, mounted in the central part of the annulus. The pump generates a maximum flux of about $650 \text{ cm}^3/\text{s}$ *in situ*, and has a minimum flowrate of about $125 \text{ cm}^3/\text{s}$. The output of the pump is divided into nine hoses through two successive flow dividers. The opposite is done for the return flow, where nine separate flow lines are combined into three, then one input to the pump. Each one of the 18 input/output hoses is connected to a ball valve which is screwed into the bottom plate of the annulus. This gives us a total of 18 input and output lines to the tank, divided into three forcing rings.

Each of the forcing rings is made up of six sections, 60 degrees each. Only six of the nine inputs/outputs are used at any time, since we use two out of the three rings. In all of the experiments described below, we connect the pump's output into the inner ring of holes ($r = 18.9 \text{ cm}$), and the return to the pump is drawn from the outer ring ($r = 35.1 \text{ cm}$). Each ring consists of 120 small holes (0.26 mm diameter), which implies that the distance between the individual holes is 0.99 cm at the inner ring and 1.84 cm at the outer ring. The middle ring was unused for all the of the experiments in this dissertation.

The pump is driven with a PMI (model U16M4) disk motor which is attached to the top lid, and which is connected to the pump via a flexible chain coupler. The motor is powered with an Aerotech (BA-series) linear servo amplifier. It was important to use a linear power supply since the switching amplifier which was previously used flooded the signal from the hot-film probes with electrical noise. The current power supply is able to provide $\pm 80 \text{ VDC}$ and almost 10 Amps, making the presence of an additional cooling fan very important. A rotary encoder which feeds back to the power supply is fixed to the motor shaft, thus closing a feedback control loop. The servo amplifier then controls the rotation rate of the pump and

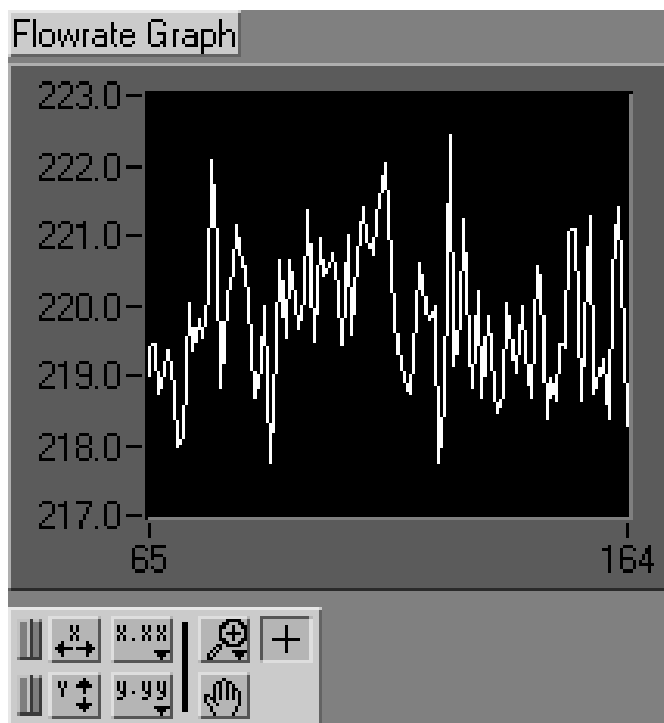


Figure 3.7: Sample time series of the flow rate in cm^3/s .

we have found the pumping rates to be very stable with respect to high frequency variations.

Over the duration of a long experiment however, we found that the pump rate showed some drift during the several-hour runs. This slow drift was removed by measuring the pump flowrate with an inline turbine flowmeter (EG&G model FT-10AEYW), whose output is connected to the data-acquisition computer. A bang-bang controller is used to keep the flowrate constant over the duration of the experiment. This setup allowed us to control the pumping rate to within $\pm 2 \text{ cm}^3/\text{s}$ over several hours of running. Figure 3.7 displays a typical flowrate measurement from the LABVIEW code that controls the pump. The x -axis is in arbitrary units, corresponding to approximately 1 s per division.

A final remark about the pumping system: The system is designed such that

the highest pressure drop is at the small forcing holes at the bottom of the channel. This ensures that the forcing into the tank is uniform in the azimuthal direction. This was tested previously in the lower forcing regime [101], and the high flowrate turbulent regime that we concentrate on should be even less sensitive to this detail of the forcing.

3.3 The hot-film system

(The black art of hot-film anemometry)

In the next chapters, we will combine visual observations with long velocity time series to obtain a general picture of the turbulent flow as it switches from three- to two-dimensions. This section describes the hot-film system that was used to obtain the long Eulerian time series. The details of the hot-film setup were worked out by Brendan Plapp, who was working as a post-doctoral researcher on this experiment. For this reason, some of the technical details might be incomplete. The essential ones are hopefully described in a satisfactory manner.

We start this section by describing the general system and its components, then we move in the next subsection into some details of the calibration and data analysis.

3.3.1 Probes and general considerations

The time series were obtained using constant-temperature hot-film anemometers (TSI model 1750) with the corresponding probes (TSI model 1210-60W). The probe sensing element is 3 mm long and 25 μm in thickness, as shown in Fig. 3.8. The sensor is held with two prongs, which penetrate a distance of 0.9 cm into the flow. The signal from the probes is then carried with coaxial cables to the anemometers, then through the slip rings to the acquisition computer. In the typical experiments



Figure 3.8: Photo of a hot-film probe. The sensing element is 3 mm long and $25\ \mu\text{m}$ in thickness.

reported here, the probe signal is sampled at 150 Hz for periods of 2 hours, thus yielding data files that had 10^6 velocities per probe. We used two probes that were placed 180° apart in the annulus, midway between the inner and outer walls of the channel. Each experimental condition was repeated two to four times, giving us a total of 4×10^6 to 8×10^6 data points for every value of the control parameters. The individual probes and the repeated runs were essential in confirming the measurements and in improving the statistical significance of the results.

The operating temperature of the probes is set by a control resistor for each probe separately. Since these resistors only come in increments of 1 Ohm, it is not possible to choose the exact operating temperature *a priori*. The data below correspond to hot-film temperatures around $67 \pm 2^\circ\text{C}$, corresponding to an overheat of approximately 42°C . The temperature of the water was also measured during the experiments and we verified that the change in temperature was usually smaller

than 1°C over the two-hour runs. This was achieved by ventilating the annulus room with an air-conditioning hose. The probes were calibrated before and after each of the experiments, so it was not crucial to know the exact overheat ratio. Finally, the water was always allowed to sit still at least 10 hours after refilling or filtering the tank; this was in order to de-gas the water to avoid the formation of bubbles at the hot-films during the runs.

In studying the statistics of the turbulence in the bulk of the flow, it is important to know that we are far enough away from the boundary layer. In a rotating system, the boundary layer is controlled by the balance of the viscous force with the Coriolis force. This balance is described by the Ekman number, defined in Chapter 2 as $Ek = \nu/(2\Omega\delta^2)$ where δ is an appropriate length scale. The thickness of the boundary layer (the Ekman layer) is determined by taking $Ek \simeq 1$, or

$$\delta \simeq \sqrt{\nu/(2\Omega)}. \quad (3.2)$$

In our experiment, $\nu = 0.01 \text{ cm}^2/\text{s}$ and $1.57 < \Omega < 11 \text{ rad/s}$. This gives values of δ in the range 0.02–0.05 cm. These boundary layers are quite thin, and the probe extends into the flow many times the Ekman layer thickness. Therefore, we are confident that our measurements are indeed “bulk” flow measurements, and not boundary layer velocities. This is further reinforced by checking the mean velocities measured from the hot-film data and from the visualization, which focuses on the central region of the tank, as described below.

Several factors influence the accuracy of the hot-film data: contaminants in the water, bubbles forming on the probes, temperature drifts, orientation of the probes. We reduced these effects by regularly filtering the water, replacing the probes to control for aging and buildup of contaminants (algae), and running them at a relatively high overheat to minimize the effect of temperature drifts. The water was allowed to de-gas for several hours before any experiments were run to minimize

bubble formation. Furthermore, care was taken in aligning the probes when they were inserted into the tank; they were oriented radially so that they would measure the azimuthal component of the flow. Our confidence in the data was strengthened by checking the reproducibility for several runs at the same conditions, and by checking consistency between the two simultaneous independent probes and with the PIV.

3.3.2 Probe calibration

The probes were calibrated before and after each run by first setting the tank at a constant rotation rate with no pumping, until the fluid reached solid-body rotation. By suddenly stopping the tank, a velocity jump corresponding to the tank's previous speed is measured: $v = \Omega r_{\text{probes}}$, where v is the instantaneous velocity of the flow, as shown in Fig. 3.9. This process was repeated at several rotation rates and a quadratic curve was fit through the points to obtain a relation between velocity and voltage. A sample calibration curve along with the voltage range is shown in Fig. 3.10.

Though the mean velocities from the two simultaneous probes should match exactly during a given run, they showed a random discrepancy of a few cm/s from each other. The source of the discrepancy is unknown, but might be due to the acquisition electronics. We addressed this problem by imposing an offset to the voltage from one probe until the mean voltages were equal, then using the calibration curve for one probe to convert both voltage series into velocities. This procedure produced velocity records that were statistically identical in their means and standard deviations, in spite of the fact that the calibration is non-linear. This method is equivalent to having a hardware DC offset on the acquired voltage, a technique that is commonly used in hot wire anemometry. The same procedure was repeated using the calibration from either probe. We found that the statistical results of interest

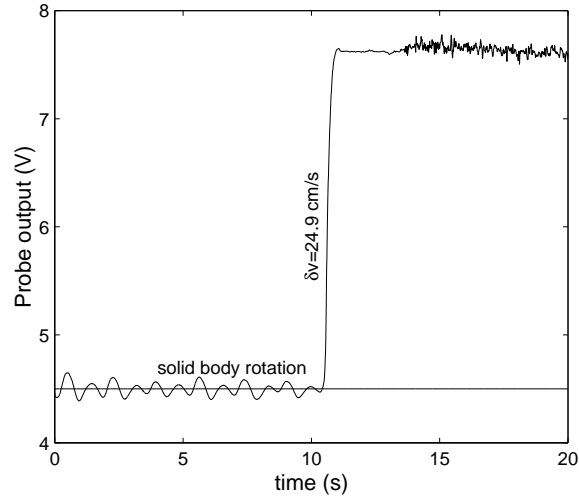


Figure 3.9: Example calibration time series showing the jump from solid body rotation when the tank is suddenly stopped from initial rotation rate $\Omega_0/2\pi = 0.15$ Hz.

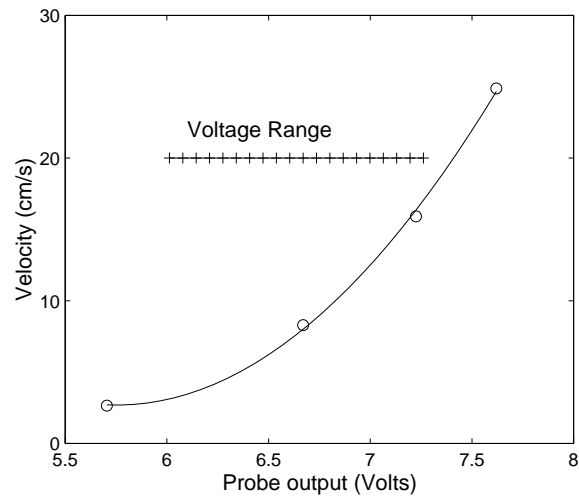


Figure 3.10: Example calibration points with quadratic fit. The '+' show the range of voltages in the corresponding experimental time series.

were indistinguishable.

3.4 Visualization system

The visualization system was built specifically for this experiment, without the use of the commercially available hardware. Three factors made the implementation of commercial PIV impossible: Rotation, rotation, and rotation. Actually, Rotation, size, and other geometrical constraints. Rotating PIV systems are not available commercially, so in the best case, one would have had to modify a commercial camera/computer system for implementation in this experiment. As for size, the illuminated area in our case is much larger than what was typical in most applications in 1997. Recently, other groups have developed large systems, but those developments were only possible once the resolution on digital cameras got above $1k \times 1k$ pixels; furthermore, the size of the annulus compared to the room does not leave enough space for the large laser necessary for the illumination. Finally, the curved outer walls and the opaque central cylinder make it necessary for the illumination to be done from several sides, making the implementation of a single laser very difficult.

In implementing the new PIV setup, the above constraints had to be accounted for, as well as other constraints such as making the system compatible with the existing hardware (slip rings, drive motor, etc...). This section is divided into four parts: the first describes the physical implementation of the PIV hardware (lighting, rotating camera, seeding particles). The second describes the basic PIV algorithm and some additions and improvements to it. The third part discusses error estimates on the data, and we end with some algorithms that were developed specifically for our experiment and which are not documented elsewhere.

3.4.1 PIV hardware

The hardware for the PIV consists of two main components: The illumination and the acquisition. Typical PIV systems are illuminated using a pulsed laser (typically a frequency-doubled Nd:Yag). A ring of Light Emitting Diodes (LEDs) seemed more suited for our purposes, because of the space/geometry constraints described above, and since the LEDs could be flashed bright enough at high enough frequencies. The acquisition is done using a Kodak ES1.0-10 bit digital camera, with a resolution of 1008×1018 pixels. The camera rotates independently above the tank, along with the computer that controls it. The third important component is the seeding particles, which will be described at the end of this section.

Illumination

The illumination is provided by a ring of 360 ultrabright red LEDs (AND model 190CRP, wavelength centered around 530 nm); the ring was designed and built with help from Jori Rupert-Felsot and a schematic drawing is shown in Fig. 3.11. These LEDs are 1 cm in diameter, and can be driven with a pulsed current up to 80 mA each; they are similar to the type of LEDs used in traffic signals. The design of these diodes makes them brighter by focusing the light from the lighting element into a very narrow cone: The nominal spreading half-angle for a single LED is about 4° . The actual angle was difficult to measure because the intensity is not axisymmetric around the light maximum, and because we found secondary peaks in the intensity as a function of cone angle. The thickness of the light sheet is limited by masking to be 2 cm at the outer wall of the tank, and spreads to approximately 5 cm at the inner wall. Even though this is a rather thick slice of the flow, we are still able to look at a region far from the top and bottom boundaries since the tank height at the inner wall is about 18 cm. Recent advances in laser technology have produced inexpensive and small diode lasers capable of producing 1 Watt or more of power.

In the future, one might want to consider replacing the light ring with small diode lasers which would produce a much thinner light sheet. This is especially an issue in the case of the 3D flow, but it is not of major importance in the fast rotation, 2D flows.

The LEDs are wired in parallel along a strip, and powered by a DC power supply (Lambda model SVPT 300-1) providing a maximum of 30Amps at 5VDC. The parallel wiring means that we cannot control the exact power through each individual LED, so there are some variations in the light intensity around the circle. However, this has little effect on the accuracy of the PIV, since the algorithm looks at the motion of particles in small spatial regions over two time steps, as discussed below, and the intensity from an individual LED is constant over different pulses. The advantage of having the lights in parallel is that it is easier to pulse a power supply providing low voltage/high current than to pulse a power supply providing high voltage/low current. Furthermore, one LED failing does not cause the whole ring to fail in this case.

The lights are pulsed in order to control the time between the two PIV frames. The control of the pulsing is done with a National Instruments (PC-TIO 10) timer card. A LABVIEW program is used to control the timing and intensity of the light pulses, and to synchronize with the camera. The electronics, shown in Figs 3.12 and 3.13 were built by Benoit-Joseph Gréa. The first diagram shows the intensity control of the LEDs. This controller uses the analog output from a separate National Instruments card to control the intensity and the TTL output of the timer card to control the timing. The diagram of Fig. 3.13 shows a current source used to control the current through the LEDs.

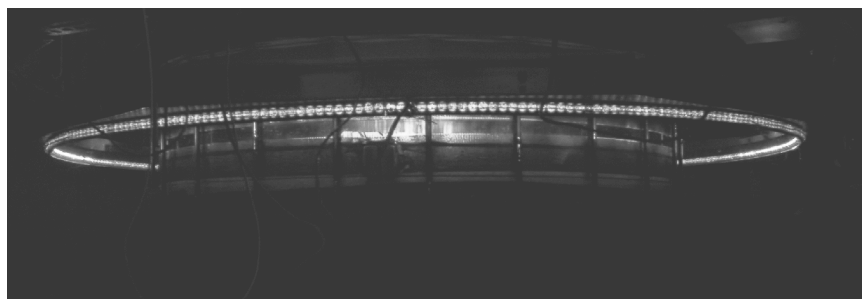
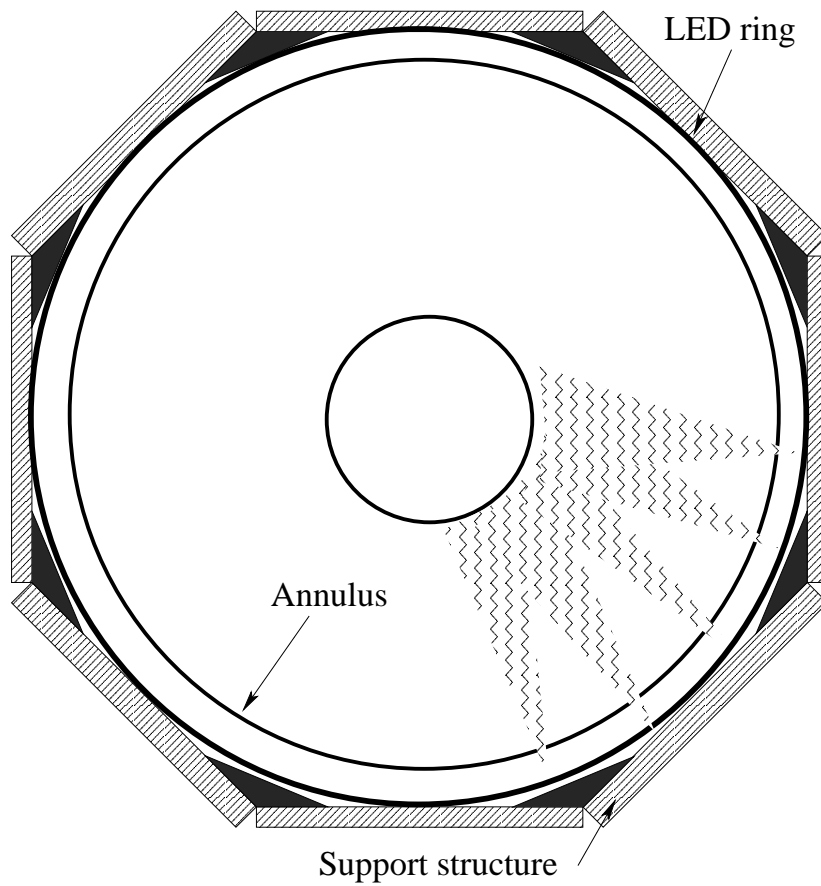


Figure 3.11: Schematic drawing of the LED ring around the annulus, and snapshot of a light pulse. The clearance between the ring and the tank is approximately 15 cm.

TRANSFORMING COMPUTER OUPUT

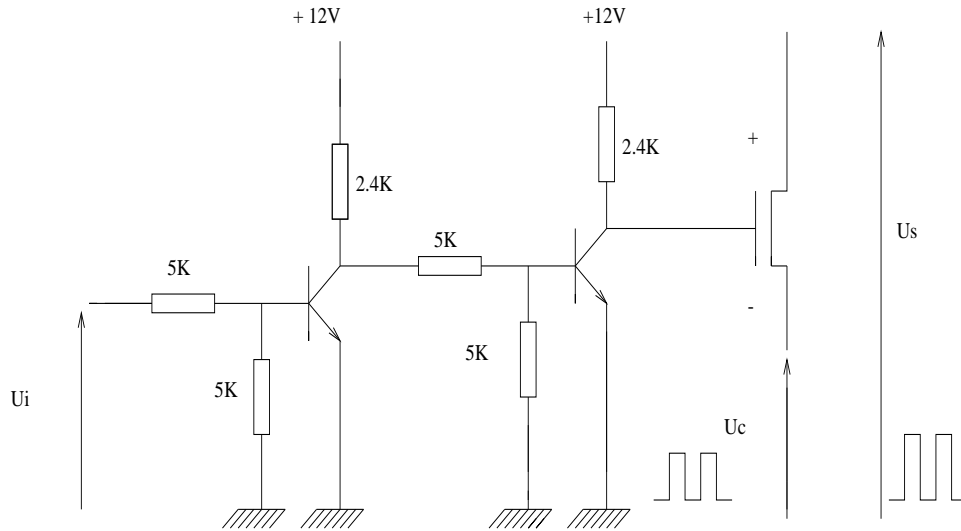


Figure 3.12: Electronics diagram controlling the intensity of the light pulses.

CURRENT SOURCE

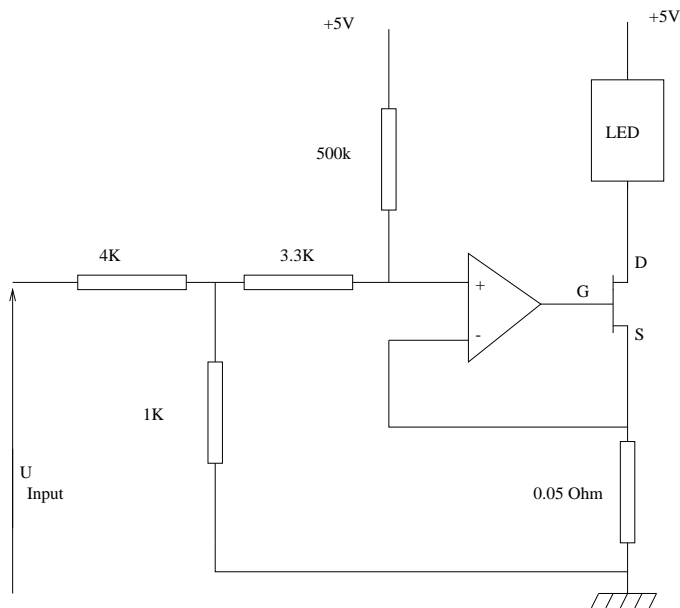


Figure 3.13: Current source to power LED ring.

The rotating camera

To photograph the flow, a Kodak ES1.0-10 bit digital camera is used. This camera has the ability to take two consecutive frames separated by as little as $5 \mu\text{s}$, with a resolution of 1008×1018 pixels at 10 bits each, i.e. providing 1024 levels of gray. A major design issue was to find a way to transmit the digital information from the camera's 70 pins while it is rotating. The solution was found by integrating a computer into the rotating platform along with the camera, as shown in Fig. 3.14. This computer is controlled during rotation through an ethernet connection which goes through the slip-rings; this way it is possible to control the data acquisition in real time.

The rotating computer (named "dizzy") had to meet certain design criteria, such as size and weight, but also had to withstand strong centrifugal acceleration. Table 3.1 shows some of the main design considerations and their importance. In the final implementation, the following components were housed on the rotating platform:

- Kodak digital camera with power supply.
- Analog CCD camera connected to live monitor.
- Motherboard and AMD K6-2 CPU.
- Computer power supply, also used to power analog CCD camera.
- Epix PIXCI-D frame grabber.
- Laptop hard drive (IBM travelstar 4GB).
- 256MB of RAM.
- Video card.
- Ethernet card.

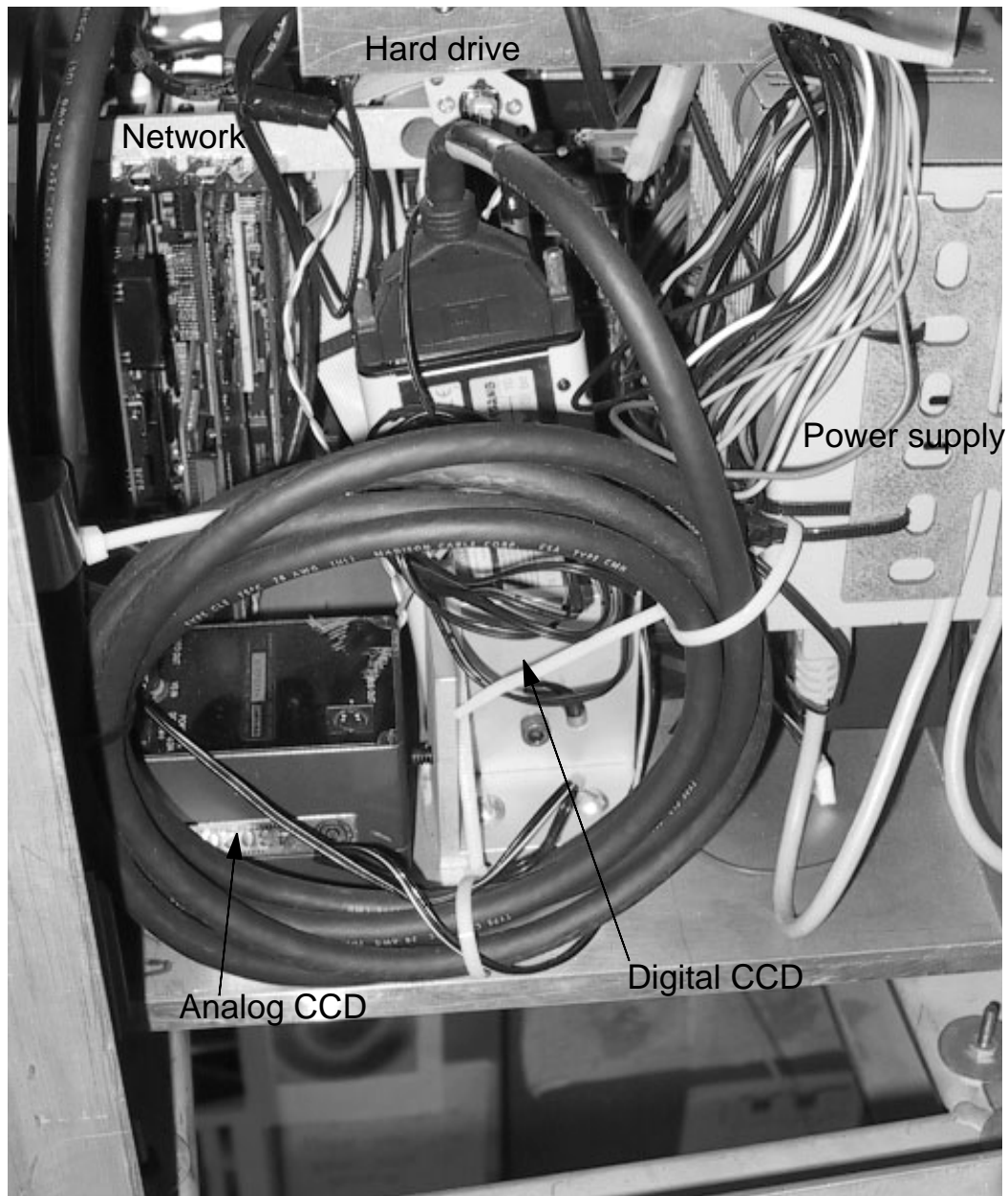


Figure 3.14: Photo of a the rotating camera and computer system. The camera is visible in the center behind the large cable, as is the computer's power supply. The hard-drive is mounted above the camera, co-axial with the rotation axis of the platform. The ethernet, video, and frame grabber cards are also visible on the left, as is the small analog CCD on the left in the foreground.

Table 3.1: The design parameters and their relative importance.

Constraint	Importance	Comments
Rotation	1	Withstand up to 3Hz rotation.
Weight and size	3	New setup has to fit with existing frame.
Vibrations	2	Minimal vibrations. Should be balanced.
Slip rings	2	Limited to 16 connections.
Flexibility	3	Ability to adjust camera angle, lens.
Real time control	2	Ability to see the flow in real-time and control data taking.
Accessibility	2	Should be easily accessible for repairs.

- Additional backup fan for CPU and motherboard

Once the components were chosen, the final design was made using IDEAS solid modeling software. This was important because the space limitations were serious, as seen in Fig. 3.14. The most important design decisions were to place both the Kodak camera and the hard drive along the axis of rotation (by placing the hard drive above the camera). In the case of the camera, this meant that it could be aligned with the tank's rotation axis. As for the hard drive, we could minimize the effect of the vibrations and the gyroscopic effects on the rotating platters and on the moving read-write arms. The weight of the power supply was balanced by the CCD camera, and the long cable for the digital camera was tied to some fixed posts in the frame. The system, as implemented, required only six slip rings: two for analog video, two for (co-axial) ethernet, and two for AC power to the computer and cameras. The platform was dynamically balanced by minimizing the vibrations by placing weights at different locations on the frame. An accelerometer was used to measure the vibrations as weights were added to the platform at different locations, until a minimum in the accelerometer signal was found. The weights are also visible in Fig. 3.14 on the right hand wall.

Since dizzy had to be controlled through its ethernet connection and since

the frame grabber could only be run under MS windows, the TIMBUCTU software package was installed to allow remote control. This was an important design choice since it meant that the graduate students did not need to be attached to the rotating platform, thus ruining the dynamic balance.

Seeding particles

The third, very important part of the PIV hardware is the choice of seeding particles. In past particle tracking implementations, crayon and wax particles were made specifically for this experiment. Those particles were difficult to make, and they were too large (1 mm in diameter) to be useful in our case.

The particle seeding now consists of white polymeric particles manufactured by Goodyear (PLIOLITE VT, $\rho = 1.026 \text{ g/cm}^3$). The particles are shipped as a polydisperse powder, so we sieve them and chose those in the range 100 – 200 μm . It is necessary to use such large particles because the field of view of the camera is about 1 m in diameter, so smaller particles would be much harder to see. Density matching the particles with the fluid is therefore very important since the particles are rather large, and since the rotating tank acts as a centrifuge which will eject heavy particles to the outer walls.

After the particles are sieved they go through a washing process to remove dust which can reduce the image contrast. The particles are then heat treated to decrease their density: The method, described in Ref. [29], consists of heating the particles in water up to about 90°C for about 30 minutes, then quickly pouring them into a beaker of ice. The heating allows the polymer to expand slowly, while the rapid cooling freezes it in the expanded state. It was found empirically that the particles thus treated stay in suspension for very long times, often longer than 24 hours. The heating also has the advantage of releasing any air bubbles that are trapped on the particles.

In order to obtain precise calibrations of the resolution of the camera, the picture in Fig. 3.15 was used. In this image, a ruler of known length was placed in the water, with the acrylic lid in place, and four pictures were taken with the ruler at different locations. The four pictures were digitally added to produce the picture below. By precisely measuring the length of the ruler in pixels (see blowup for resolution) and averaging these measurements, we could obtain a very precise calibration of the PIV images. A similar procedure was used in the case of “section” images, where only part of the tank is visible. The camera was always focused on the particles in the light sheet which is fixed. This meant that the distances were not distorted by focus problems.

Using the illumination scheme, the rotating camera and the seeding particles, we are finally able to obtain quantitative information about the velocity field from particle images. Two sample images are shown in Fig. 3.16. The full tank image corresponds to a resolution of 0.969 pixel/mm, while the section images have a resolution of about 3.51 pixels/mm.

3.4.2 Algorithms

The work described in this thesis uses a standard implementation of Particle Image Velocimetry to obtain quantitative velocity fields in the tank. The routines were written for MATLAB by Johan Kristian Sveen, and they are distributed under the GNU public license¹. The implementation of MatPIV is fairly advanced, using many modern ideas in improving the resolution and accuracy of the measurements. For a modern review of some of the methods, see Ref. [102]. Several additions and changes were made to the basic MatPIV package to suit our geometry and our data requirements. After a general overview of the standard PIV techniques, some of these additions are described below.

¹The web page for the software package is at <http://www.math.uio.no/jks/matpiv/>

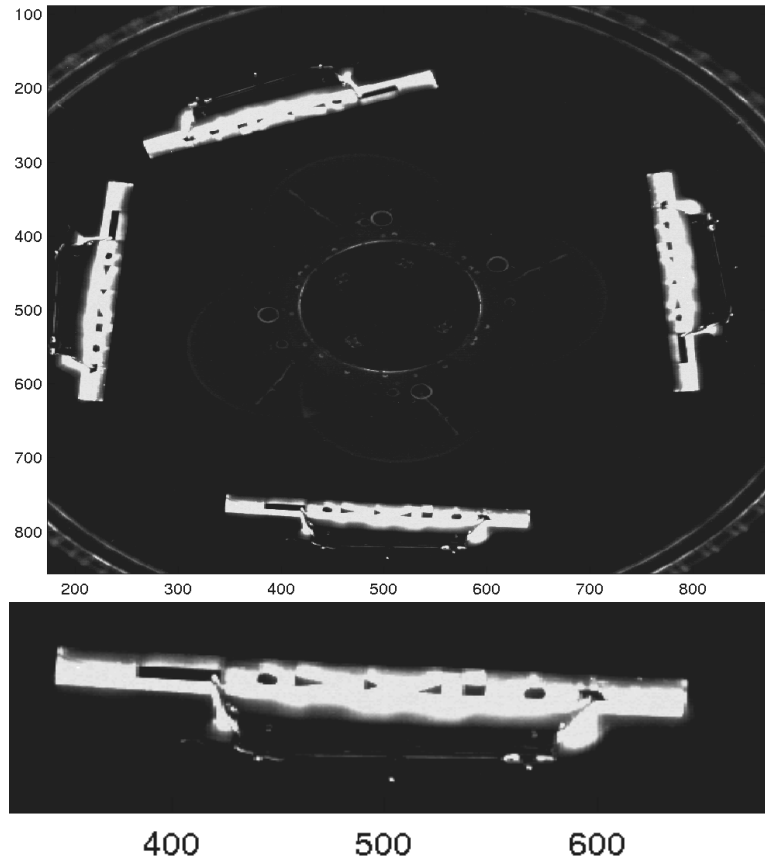


Figure 3.15: Calibration of the camera resolution, axes are in pixels. Bottom picture is a closeup of the ruler, showing the sharpness of the resolution.

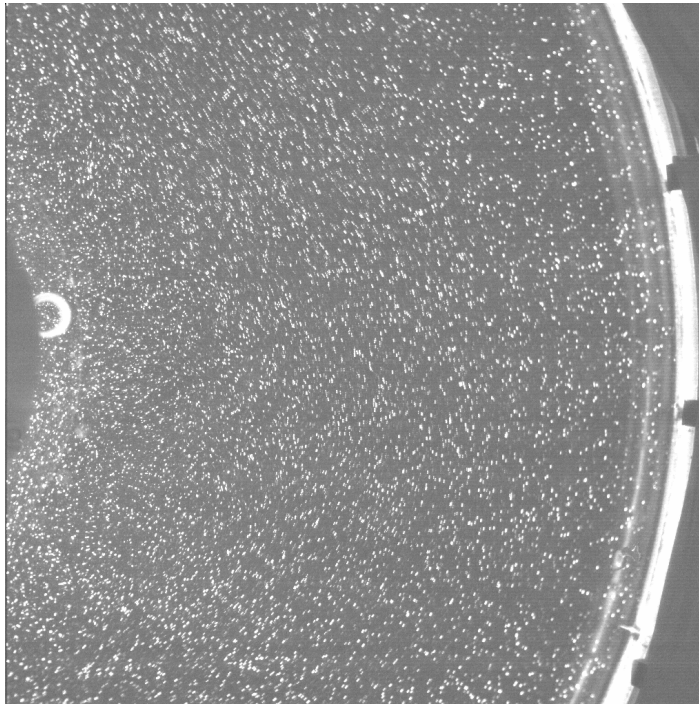
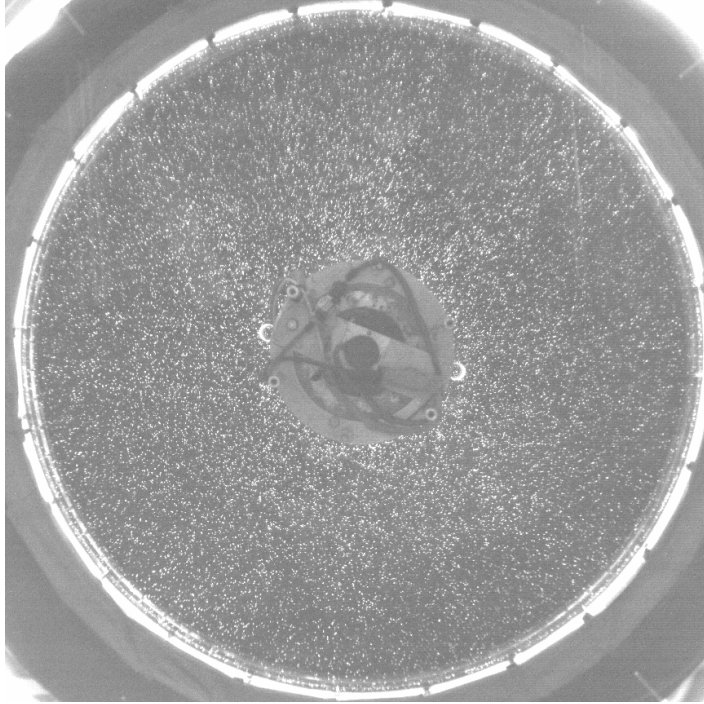


Figure 3.16: Particle images for the whole tank (top) and for a section (bottom). $\Omega = 4.7$ rad/s and $Q = 150$. Approximately 5,000 particles are visible in each of these pictures.

The basic algorithm for digital Particle Image Velocimetry is fairly widely used, and described in detail by Adrian [1] and in the recent book by Raffel *et al.* [73]. The technique involves taking two pictures of the flow, separated by a known time delay δt . The first step is to break the large image into small subsections as shown in Fig. 3.17. Typically, these *boxes* are 32×32 or 64×64 pixels, depending on the particle seeding density. Here, the first box is 32×32 and zero-padded to 64×64 , while the second box is 64×64 . This is to normalize the effects of the edges on the correlation function [73]. In these pictures, we can see that the number of particles is fairly large (more than 15 particles in the box), but the size of the particles is often only one pixel.

A cross-correlation of the box from image 1 and the corresponding region from image 2, when normalized properly, will show a peak at a some distance from the center of the 2D correlation function (Fig. 3.17). The location of this maximum corresponds to the distance that the particles traveled on average in the time delay δt . PIV is first and foremost a technique for measuring displacements. By assuming a known time step, velocities can be obtained by dividing the measured displacement by the time step. This is an important concept, since it means that standard PIV routines cannot resolve acceleration without modification, so rotation and shear information is not available.

The first improvement that can be made to the basic algorithm is to improve the peak finding. If we simply look for the maximum of the correlation function, then our resolution is equivalent to one pixel. This is shown in Fig. 3.18, where we plot the values of the correlation along the row and the column going through the peak of Fig. 3.17. We can improve our resolution by using information from

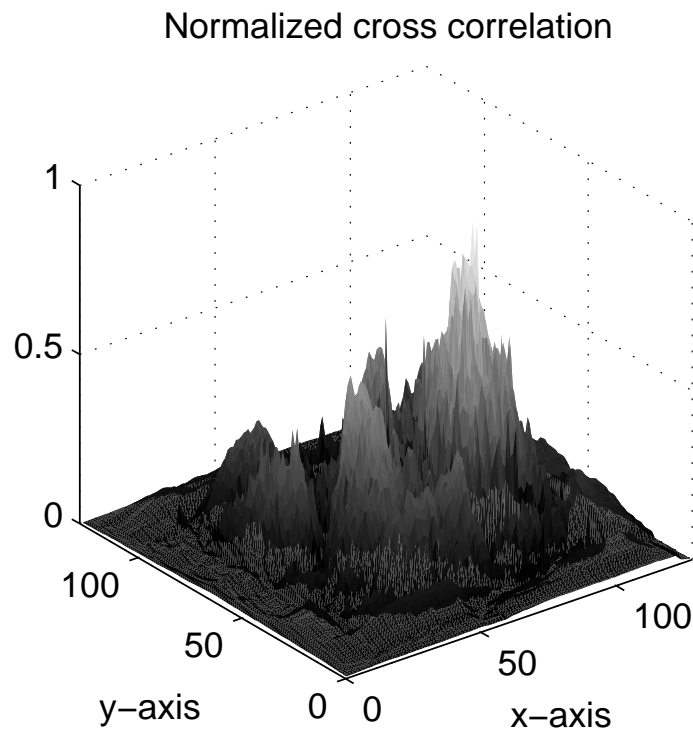
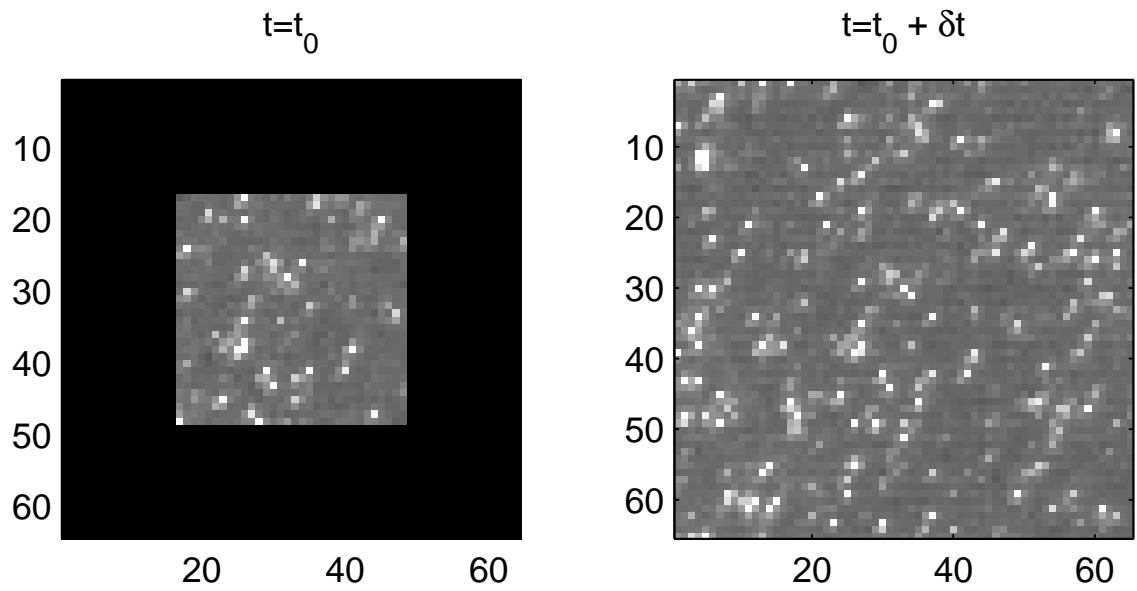


Figure 3.17: Standard PIV algorithm.

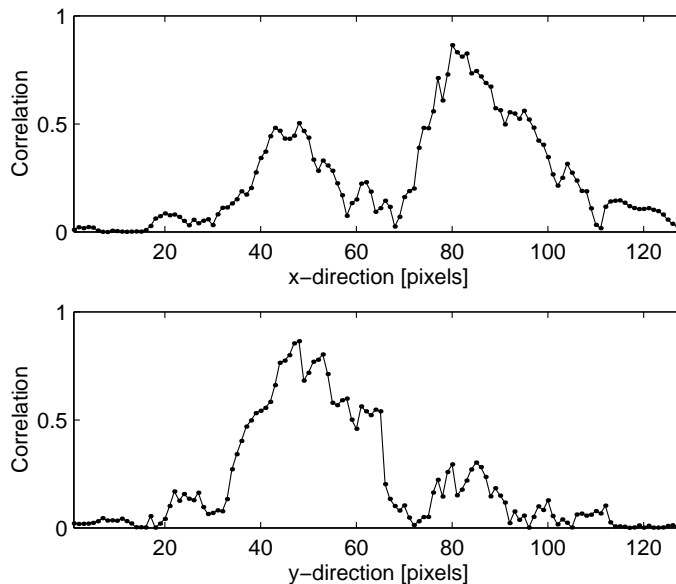


Figure 3.18: Slices through the 2D correlation function showing the location of the peaks. The fitting of the peaks uses the 5 adjacent points.

the points around the peak, e.g. fitting them with a smooth curve and finding the maximum of that curve. Typical choices for a fitting function are a paraboloid, a Gaussian, or finding the centroid of the points. Each of these fitting techniques uses a different number of points around the peak. The choice of function is largely a trial-and-error one, with intuition playing a major role in the analysis. In the example of Fig 3.18, we see that a large number of points might be necessary because of the large fluctuations near the peak. This improvement gives PIV a “sub-pixel accuracy”, which is one of its greatest strengths.

Improving the accuracy further is generally equivalent to increasing the height of the correlation peak. The first phenomenon that reduces these peaks is when particles leave or enter the interrogation box between the time steps. This problem is minimized by using large boxes that contain many particles, which essentially minimizes the box perimeter compared to its surface area. On the other hand, the value of the correlation will also suffer if the particles in the box lose

their place with respect to each other, i.e. in the case of strong shear or rotation in the flow. The likelihood of this deformation to happen is increased with larger box sizes, especially in regions with high velocity gradients. There are therefore competing needs with respect to the box size.

A standard solution to this conflict is to use multiple passes of the particle images with varying window size. The first pass uses a relatively large box to get a coarse-grained displacement field with few erroneous vectors. These outlier vectors are usually filtered out and interpolated from the surrounding values. The next pass uses a reduced box size along with information from the first pass; instead of correlating two regions at the same location of the image, the region from the second image is shifted by the displacement vector obtained from the first pass. This way, we maximize the likelihood that the particles that were in the first image will be in the second image, and hence we increase the height of the correlation peak. This process of reducing the box size can be repeated as desired, and for a “good” image, can produce a very high resolution of accurate displacements. A representative velocity field is shown in Fig. 3.19 corresponding to the high-resolution field from a section of the annulus. The vectors are approximately 0.3 cm apart.

3.4.3 Error estimates and controlling errors

While it is true that PIV provides “sub-pixel” accuracy in the measurement of mean displacement, this statement can be a bit misleading. Currently, the best PIV algorithms boast an accuracy of about 0.1 pixels in realistic experimental situations. As seen above, 0.1 pixels in our images corresponds approximately to 0.1 mm in physical space; with typical time delays $\delta t = 10$ ms, this accuracy in measuring displacement corresponds to a minimum error in velocity of 1 cm/s! This is a large error considering that our typical velocities are on the order of 20 cm/s. A reduction of the field of view would produce a more favorable ratio of pixels/mm,

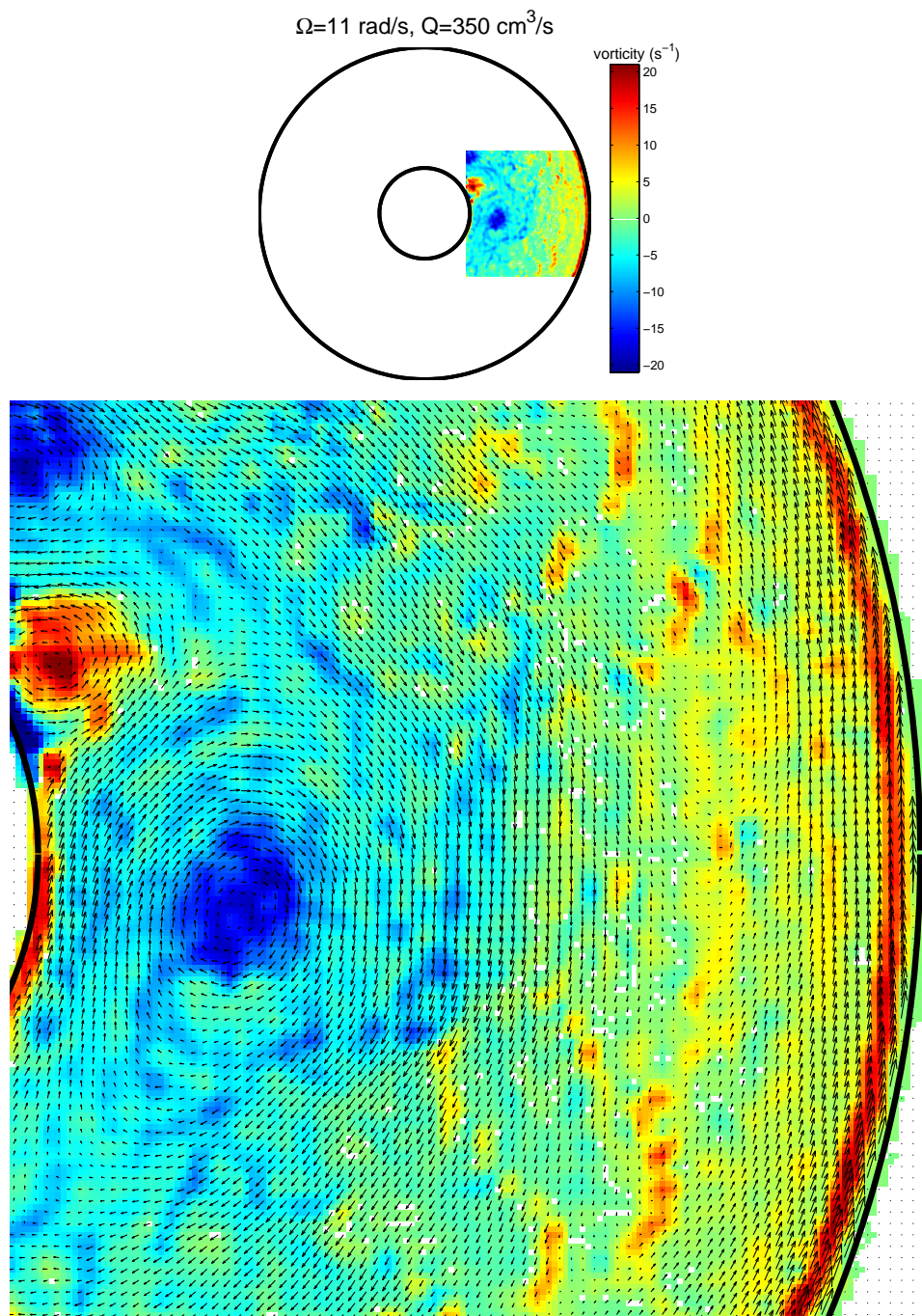


Figure 3.19: Velocity vectors and vorticity colormap in a section of the annulus. Note the presence of structures of different sizes; The resolution is as small as 0.3 cm.

but it would also require a smaller δt since the particles move a larger number of pixels in the same amount of time. This would again raise the error in the velocity measurements. For this reason, we rely on the hot-film measurements (which have much higher accuracy) for the sensitive velocity measurements, and we use the PIV to track structures in the flow, and to understand the flow evolution.

There are several types of error that can contaminate a visualization study. First, one needs to have confidence that the tracers in the flow are actually following the motion of the fluid. This becomes even more significant in the case of turbulent flow, where the local pressure and velocity gradients can have a large effect on the particles. Next, the visualization hardware has to function well: the images need to have a high enough contrast between the particles and the background, the particle images need to be larger than a few pixels, the amount of optical distortion should be kept to a minimum, the intensity of the images needs to be relatively constant between the first and second frames, etc. These errors can be minimized at the time of the design of the visualization system, and are crucial to reducing the measurement errors. The above sources will be referred to as “experimental” sources.

Once these experimental sources of error are minimized, there remain errors in the algorithms due to the discretization of the images both in space (discrete pixels) and in intensity (discrete bits). These errors are the ones that are typically discussed in the analysis of PIV error, e.g. by Westerweel *et al.* [103] and by Fincham and Spedding [31].

Below we will start with a discussion of the experimental sources of error in the following order:

1. Particle trajectory might not match actual fluid trajectory.
2. Motion perpendicular to the plane of illumination.

3. Uncertainties in time delay.
4. General quality of the images.
5. Image distortion.
6. Moving shadows from the experiment walls.

Afterwards we will move to the algorithmic error sources, and discuss the algorithms that were used in this study. The phenomenon of “peak locking” will be introduced as well as ways to deal with it.

Motion of particles

An extensive study of the motion of particles as passive tracers was carried out by Weeks [101]. Several forces are important in determining whether the motion of the particles will closely match the motion of the fluid, including the buoyancy force, the centripetal force, the viscous drag, the fluid inertia, lift (the Magnus force), and the pressure gradient. He concluded that neutral buoyancy was an important factor in choosing the particles to use. We will not repeat the analysis here, but below is a less extensive justification for the particles we use.

The particles used in this experiment were in the range of $100 - 200 \mu\text{m}$. These are relatively large compared with particles used in other turbulence experiments, meaning that the drag from the fluid might not be strong enough to keep the particle stationary with respect to the water around it. Mei states that the frequency response of a solid particle in a liquid depends on the density ratio and the stokes number of the particle [62]. He calculates that for a particle which is perfectly neutrally buoyant, the frequency response will be exact for any frequency. For a density ratio close to unity, the frequency response will also be close to unity for low Stokes numbers [62]. The Stokes number is defined as:

$$St = \frac{\rho_p U_c D_p^2}{18\mu L_c} \quad (3.3)$$

where the subscript p refers to the particle, and c refers to the flow. Using $\rho = 1.025 \text{ cm}^3/\text{s}$, $U_c = 20 \text{ cm/s}$, $D_p = 0.015 \text{ cm}$, $\mu = 0.1 \text{ g/cm s}$, and $L_c = 1 \text{ cm}$, we obtain $St = 0.0026$. This means that the stokes drag is dominant, even for a structure (e.g. vortex) that is 1 cm in diameter and that is moving at 20 cm/s. This quick calculation shows that our particle trajectories should match the flow very well. In practice, we find that the particles centrifuge to the outside of the tank at high rotation-rates for flows where the mean jet is weak. However, this behavior occurs on time scales of several minutes, whereas the image pairs are typically a few milliseconds apart. Therefore the error in the displacement over 10 ms will be very small compared to the actual displacement.

Out of plane motion

The out-of plane motion of the particles is also an issue to consider. In the case of the high rotation rate flows, this problem is minimal since the flow is forced to be largely 2D. This is a significant advantage of our study compared with 3D turbulence where one is looking at two of three important velocity components. In the 3D flow, we do have some flow in the direction perpendicular to the light sheet, and one needs to be careful in interpreting the low rotation data. However, since our light “sheet” is rather thick (about 2 cm) and the time delays are short (about 10 ms), a particle would have to be traveling vertically at 2 m/s in order to leave the illuminated region. This is typically not the case in our flows except possibly above the injection holes; even in the 3D flow we expect the out of plane motion to be small.

Time delay

The accuracy of the time delay δt is determined by the light pulsing. We use a “frame straddling” technique in controlling the time delay which works as sketched in Fig. 3.20. The camera shutter is opened for 30 ms while the experiment is kept in the dark. After an initial delay, we flash the LEDs for a known time t_{LED} . Shortly afterwards the first frame finishes and the second camera frame starts, at which time we flash the LEDs again. The minimum time between camera frames is very short, on the order of 5 μs , which means that we can control δt very precisely by flashing the LEDs. The rise time for those is also in the μs range and the clock that controls the timing runs at 2 MHz. All this means that δt between frames is known to better than 10^{-6} seconds, i.e. the error introduced by this is very small. However, the nominal value for δt is the value between the start of the first flash and the start of the second flash. The fact that the time t_{LED} is finite (typically in the range 2-6 ms) might introduce a certain error in the measurements. However, if the particles do not accelerate significantly between the frames, the particle image from the first and second frames will be similar, and the correlation should still work properly.

Quality of images

In our PIV technique, we have followed some of the rules of thumb that were developed for increasing the accuracy of the measurements. These rules of thumb were developed from computer generated images; starting from a known computed velocity field, a first image is generated typically with a Gaussian distribution of particle sizes and intensities. The particles are moved according to the flow field, and the PIV code is used to re-calculate the velocity field. By checking the calculated version with the known one, a few patterns emerged in terms of the size and density of particles, etc [73].

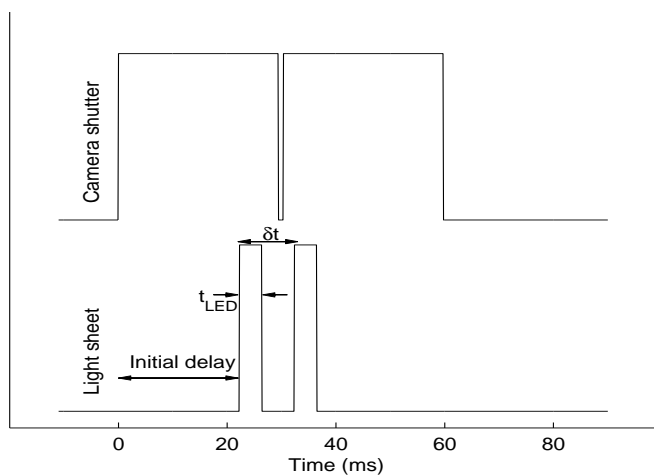


Figure 3.20: Frame straddling technique.

These rules of thumb concern the size of the particle image which should be larger than 4 pixels, the particle density where a correlation box should contain more than 4 particles. Our particles are smaller than one pixel in size, but their image appears large due to their brightness. The typical particle displacement between frames should be less than one pixel, although that can be corrected for by shifting the window.

Image distortion

We visualize our experiment through a thick ($t = 4.3$ cm) acrylic lid. The casting process that is used for such thick pieces allows them to cool down outside the mold. Therefore we have found that 10% variations in thickness are common for such plastics. It was important to smooth out these thickness fluctuations to remove any lensing effects that would distort the apparent motion of the flow. That was done by carefully machining both sides of the lid, making sure that the surfacing did not heat the plastic to more than 40°C. Once both surfaces were made parallel and flat (nominally to a few mills), the lid was polished to make it transparent.

The machining was done at Advanced Research Labs at the Pickle campus, while the polishing was done by Glass Mountain Optics, a company that specializes in polishing telescope mirrors.

Moving shadows

A source of error that is specific to our system is produced by the moving shadows of the tank walls. The shadows are produced from two sources: First, the top lid is held by metal posts which screw into the bottom plate, thus making the whole setup more rigid. Second, seams in the walls where different acrylic sections are glued together also produce shadows due to small cracks in the glue. The light from the individual LEDs is very directional, so that the posts cast shadows as they pass in front of the diodes.

As the tank rotates, these shadows sweep in the opposite direction such that a correlation box that is well lit during the first frame can become darker in the second frame or vice versa. At the low rotation rates, the shadows move very slowly compared to the pulsing rate, so they do not represent a big problem. However, at $\Omega = 11$ rad/s, the shadow can move 5 cm in the 10 ms between frames.

This change in illumination can cause the correlation peak between the two images to be shifted in the direction of the shadow motion, in a way that is quite complicated. However, we can minimize the effect of the moving shadows by filtering the water and keeping only the large bright particles. If the contrast between the particles and the background is strong, the bright particles are significantly brighter than the background even when they're in the shadow, and the induced error is minimized in this way.

Peak locking

The major source of error in the PIV algorithms comes from estimating the location of the correlation maximum. These estimates often show a bias towards integer number of pixels, a phenomenon known as “peak locking”. It is caused either by particle images that are too small (only 1 or 2 pixels), by a variation in the sensitivity of the individual pixels, or by the “fill factor” of the camera, i.e. the area of the CCD array that is sensitive to light [73]. In our case, the fill factor of the Kodak ES1.0 is 60% (a small value), and probably the cause of the peak locking that we experience. The signature of peak locking is seen in a histogram of the measured displacements as in Fig. 3.21(a). This kind of error is well documented [31, 73] but solutions to it are difficult. The first solution is to try different functions to fit the correlation peak; we use a Gaussian fit which gives the best results for our data, but which does not solve the problem completely, as shown in Fig. 3.21.

With help from Benoit-Joseph Gréa, we implemented two changes to the PIV algorithm which reduced peak locking significantly. The first change was to implement non-integer window displacements during the second pass of the PIV routine. Using MATLAB’s interpolation function, we were able to make box shifts of non-integer number of pixels. The second change was to implement box rotation to increase the correlation peak height. So by using the initial vector field, we could estimate the amount of vorticity in a given region and rotate our windows to account for the solid body rotation of the particles. These two changes were found to improve the peak locking problem, as shown in Fig. 3.21(b), where the histogram for the same particle images produced much more evenly spread displacements.

In summary, it is very difficult to estimate the actual error in the PIV measurements. These errors probably vary as a function of rotation and pumping rates, with the cleanliness of the water, or with the size of the field of view. Studies of simulated particle images using algorithms such as ours produce an accuracy of about

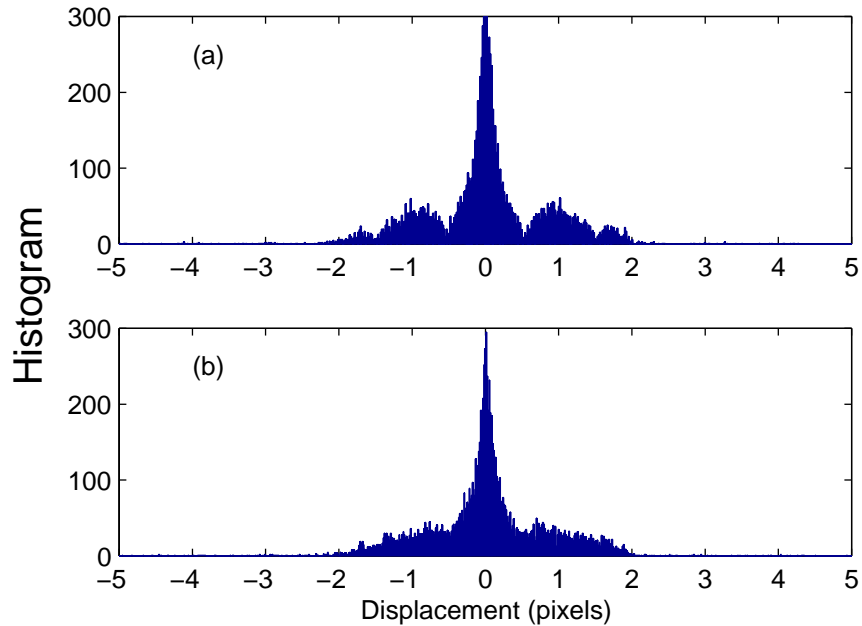


Figure 3.21: Peak locking, observed in part (a), is largely removed in part (b) with non-integer window displacements, and box rotations.

0.2-0.3 pixels or better for the mean displacement in a box. That would mean a conservative estimate of $0.03/10^{-2}$ cm/s, or ~ 3 cm/s. Such an uncertainty is too high to obtain precise quantitative information about the flow-field, making high-order statistics inaccessible with the current PIV. However, for the high flow rates ($U > 60$ cm/s), the signal to noise ratio is high enough that we are able to obtain robust statistics such as energy spectra and correlation functions.

Even with its limitations, the PIV is still very useful for computing and visualizing a flow-field at all flow conditions. It has provided some of the first quantitative data about vortex interactions in a 2D flow, as will be seen in later chapters. This warrants a few words about the computation of vorticity. The algorithm used to compute vorticity uses the “circulation” method, which is essentially the computation of an integral rather than a derivative. We use Stoke’s theorem relating the vorticity and the circulation [73]

$$\Gamma = \oint \mathbf{u} \cdot d\mathbf{l} = \int \omega \cdot d\mathbf{S} \quad (3.4)$$

where Γ is the circulation, \mathbf{l} is the path along the surface \mathbf{S} , and $\omega = \boldsymbol{\omega} \cdot \hat{\mathbf{n}}$ is the vorticity. In a discrete grid, this equation can be applied to a point by marching in a box around the point and summing the velocities. This method produces much lower errors in the vorticity measurements than typical differencing schemes. It is equivalent to a center difference scheme applied to a smoothed (3×3 kernel) velocity field [73], so that it can also be used to compute other derivative quantities (e.g. divergence).

3.4.4 Specific algorithms

A few algorithms are very specific to our experiment and were developed over the course of the study. Below, we describe three main ones that will help us analyze the data in future chapters. The first is an algorithm that calculates the azimuthal and radial velocities from the Cartesian velocity vectors. The second calculates the polar shear tensor $\sigma_{r\phi}$ from the velocity field. The third maps the annulus onto a rectangular channel, transforming the polar geometry into a Cartesian one.

Azimuthal and radial velocities

In order to obtain the azimuthal and radial velocity, one needs to remember that those velocities depend on the location in the tank. Given a position (x, y) (x and y have zero-mean), the first step is to convert that position into an (r, ϕ) coordinate. Then the u and v velocities need to be transformed in the same way to their polar values u_{rad}, u_{θ} (here, rad and θ are different from the radial and azimuthal coordinates r, ϕ). Using the above transformed pairs, and using $U = \sqrt{u^2 + v^2}$ as the magnitude of the velocity, we obtain the radial and azimuthal components using:

$$\begin{aligned}
u_r &= U \cos(u_\theta - \phi) \\
u_\phi &= U \sin(u_\theta - \phi)
\end{aligned}
\tag{3.5}$$

One advantage of obtaining the azimuthal velocity is that we can easily impose a fixed rotation on all the velocity vectors. This is done by subtracting a constant times the radial position from the azimuthal velocity:

$$u_{rot} = u_\phi - c \cdot r. \tag{3.6}$$

This technique is very useful when we wish to subtract the mean rotation from the flow. It allows the viewer to digitally place him/herself in the frame of the moving flow rather than the frame of the tank. By making this rotation, the vortices seen in the vorticity plots match the vortices in the streamfunction very well, as will be seen in later chapters. In the past, the camera was rotated faster/slower than the tank to have the same effect of bringing out the vortices that are advecting with the flow.

Polar shear

The shear in a polar coordinate system is defined as

$$\sigma_{r\phi} = \frac{r}{2} \left[\frac{\partial(u_\phi/r)}{\partial r} + \frac{1}{r} \frac{\partial v_r}{\partial \phi} \right] \tag{3.7}$$

where u_ϕ is the azimuthal velocity and u_r is the radial velocity. In the case where the azimuthal variations can be ignored, the ϕ derivative can be dropped and we compute the mean shear as

$$\bar{\sigma}_{r\phi} = \frac{r}{2} \frac{\partial(u_\phi/r)}{\partial r}. \tag{3.8}$$

Both of these quantities are of interest and will be used in later sections. To calculate $\sigma_{r\phi}$ and $\bar{\sigma}_{r\phi}$, we start by computing u_r and u_ϕ by using the above method. Once that is done, the only required step is to differentiate u_r and u_ϕ in terms of r and ϕ . For that, we use the chain rule. Since the functional relationship between (x, y) and (r, ϕ) is known, we use a finite differencing scheme (3rd order) to obtain the derivatives with respect to the Cartesian coordinates, and we use the exact form for $(\partial x/\partial \phi)$, etc. for the other terms. These steps provide all the necessary derivatives, and adding them appropriately becomes a simple matter. All the terms in Eq. 3.7 above can be estimated in this way.

Mapping the annulus onto a rectangle

Starting with the annular geometry, we would like to map the circular walls onto straight lines for both the inner and outer boundaries. This way, the flow is in a periodic straight channel, where the horizontal coordinate is the azimuthal angle, and the vertical coordinate is the radial position. This routine is very useful if one needs to measure the velocity at a particular radius, or at a particular azimuthal slice. It is the only routine among those described here which requires interpolation of the data, so care must be taken with that aspect.

If we wish to map a 2D vector field (such as velocities), the first step is to obtain the radial and azimuthal components as described above. Quantities such as vorticity or other single-components 2D fields need not be changed. Next, we define a rectangular grid of r and ϕ , as shown in Fig. 3.22. This rectangular grid $(r_{\text{rect}}, \phi_{\text{rect}})$ can be written in terms of Cartesian (x, y) coordinates by simply using

$$\begin{aligned} x_i &= r_{\text{rect}} \cos(\phi_{\text{rect}}) \\ y_i &= r_{\text{rect}} \sin(\phi_{\text{rect}}) \end{aligned} \tag{3.9}$$

and these (x_i, y_i) consist of the coordinates on the annulus, but rearranged in a

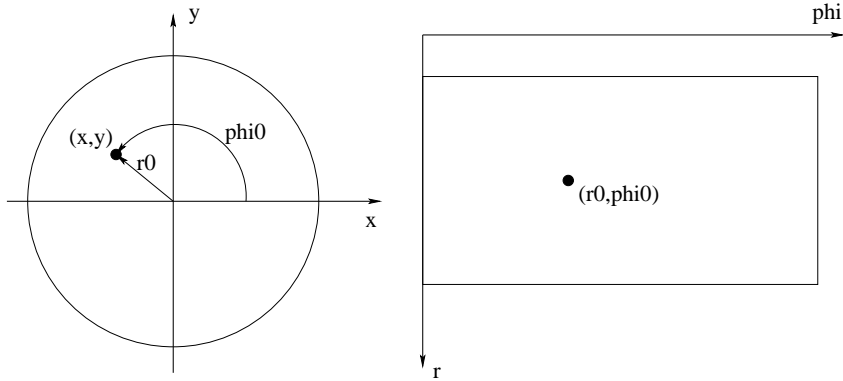


Figure 3.22: Rectangular mesh and corresponding coordinates on the annulus.

rectangle. The final step is to use MATLAB's 2D interpolation function to obtain the values of u_r and u_ϕ at every (x_i, y_i) which corresponds to a $(r_{\text{rect}}, \phi_{\text{rect}})$ on the rectangle.

The mesh size of the rectangular grid is typically taken to be equivalent to the PIV resolution: In the radial (y) direction, the step size was taken to be 0.8 cm. In the azimuthal (x) direction, we typically chose ϕ going from 0 to 2π in 600 steps, which is roughly equivalent to the number of vectors at the outer perimeter of the annulus. Extensive testing of the effect of the grid size was done, and we did not find the size or the exact form of the interpolation to be very significant in the final results.

An example of this mapping is shown in Fig. 3.23. Here, we map the vorticity and stream-function fields because they are easy to visualize.

Because of the geometry of the annulus, this rectangular mapping oversamples the regions near the inner wall. A small vortex near the inside of the tank will appear much larger in size, and one should be careful in defining the size/wavenumber of structures as a function of radius. Note however that the relation between the structures is preserved, and this technique is very useful in many calculations as will be seen later.

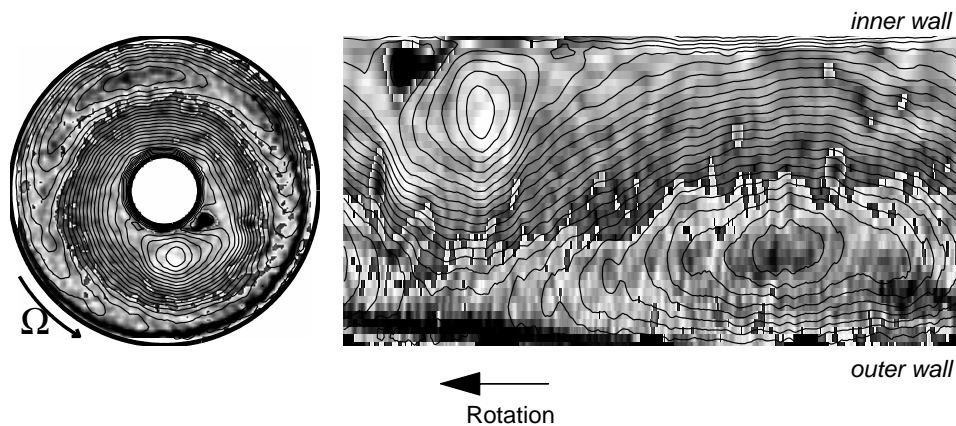


Figure 3.23: Vorticity and stream-function field mapped onto a rectangle.

A final note on the colormaps used in this thesis: When color images are unavailable for 2D maps, it is often useful to use discontinuous gray scales. These gray-scale schemes take some time to get used to, but they convey information with much less ambiguity and with the possibility of including more detail than a standard gray scale. In Fig. 3.23, we use a gray-scale scheme for the vorticity ω which goes from light to dark as ω approaches zero from below. At $\omega = 0^+$, the scale discontinuously jumps back to white and gets darker again as ω increases. By this method, a vortex with a dark center surrounded by lighter tones has cyclonic ω , meaning ω has the same sign as the rotation direction of the tank. A vortex with a light center surrounded with dark tones is anti-cyclonic, turning in the opposite direction than the tank.

3.5 Summary

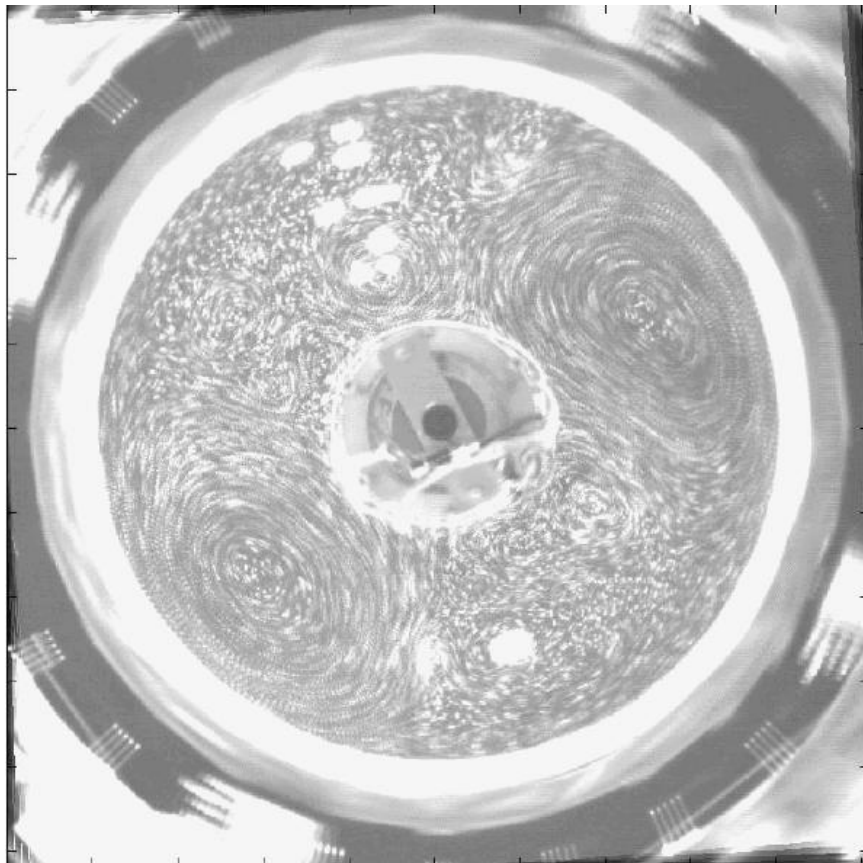
In summary, this is a very instrumentation-intensive experiment and its unique geometry makes standard instruments often unsuitable. This chapter described the control of the two experimental parameters, as well as the ways in which measurements were made. It concentrated on the hot-film anemometry and the par-

ticle imaging, placing some error bounds on the accuracy of these measurements. These error bounds suggest that the PIV can be used to resolve flow structures and show their dynamic behavior as vortices interact with each other and with the mean jet. The hot-film measurements allow us to get very long time series with high signal-to-noise ratio, thus allowing us to calculate high-order statistics of the turbulent velocity series. This chapter also introduced some of the “tricks” used in the analyzing the PIV data which are unique to our experiment.

In the next chapter, the techniques described here will be used to test the theory introduced in Chapter 2. The visual information will be used first to describe the flows obtained in the experiment. Since this is a not a very typical flow, some care will be taken to characterize it properly as a function of the control parameters. We will then use the hot-film time series to look for scaling of the high-order structure functions. The changes in scaling between the low and high rotation rate cases will be discussed and related to the spatial structures seen in each of the flows. Finally, we will try to make a good connection between the structures that we see visually and the scalings that we observe in the time series.

Chapter 4

Transition from 3D to 2D



When Leonardo Da-Vinci first observed turbulent flows, he saw and sketched the structure of the eddies being carried by the mean flow. His understanding of turbulence was a spatial one, concerning the interaction between spatially extended structures. This (*Leonardian*) view of turbulence remains important, but it has been largely replaced by the statistical view, which is more quantitative with measurable and reproducible predictions, since the work of Kolmogorov. Most recently, there has been significant interest in bringing together the two viewpoints by understanding the relation of the statistical fluctuations to real structures in the flow. These advances have been made possible by advances in visualization and in computation. They were motivated by attempts to explain the anomalies of the statistical scaling (e.g. [78, 27]), but also to control the turbulence in order to reduce drag, improve mixing, or other practical applications [97, 21].

In this chapter, we will start with a Leonardian description of our flow, by describing the coherent structures that form and the interaction between the strong jet and the vortices. This will be done by starting with a general overview and adding levels of detail through the use of the visualization techniques. The slow-rotation and fast-rotation cases will be compared, making the case for a two-dimensionalization of the fluid flow as the rotation rate is increased.

The second part will move to the Kolmogorov statistical description of the flow through the use of the long velocity time series. These measurements allow us to look for scaling regions and to test quantitative ideas of turbulence such as the hierarchical symmetry of the She-L  v  que model. These calculations show a clear shift with increasing rotation rate from flows similar to the usual 3D flows, to a 2D flow which matches Kolmogorov's 1941 theory in several ways.

We will finally bring together the two approaches and explain the statistical information with the spatial structures that we visualize.

4.1 Flow description

In order to describe the flows in the rotating annulus in the 3D and 2D cases, let us pick two representative snapshots. The first one, which we will refer to in this section as the 3D flow, is taken at a rotation rate $\Omega = 1.57$ rad/s ($\Omega/2\pi = 1/4$ Hz), and at a pumping rate of $Q = 550$ cm³/s. This is not the lowest rotation rate at which data were taken, but it corresponds to a Rossby number of approximately 0.7. The representative 2D flow will be at a rotation rate $\Omega = 11.0$ rad/s ($\Omega/2\pi = 1.75$ Hz), and a pumping rate $Q = 350$ cm³/s. The corresponding Rossby number here is about 0.2.

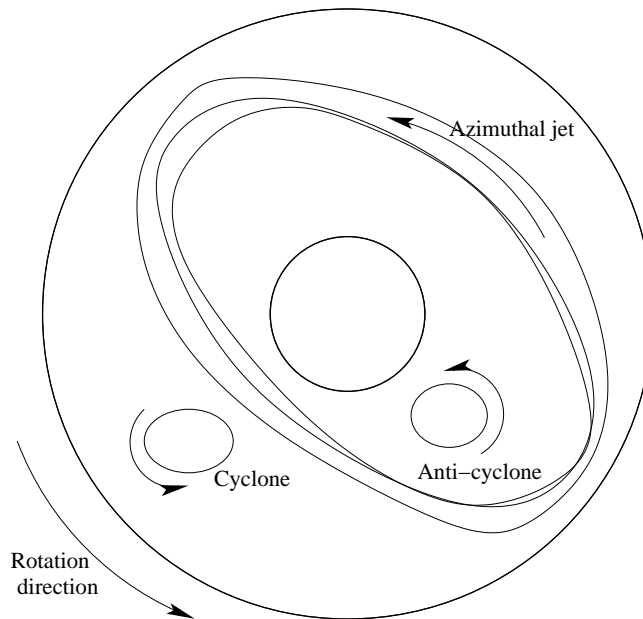


Figure 4.1: Schematic representation of a cyclonic vortex, an anti-cyclonic vortex, and a jet in the annulus.

Using particle images of the whole annulus, let us start with a general overview of the flow and add detail as we go along. A schematic of what we will discuss is shown in Fig. 4.1; the streamlines which connect without crossing the

center of the annulus correspond to cyclonic and anti-cyclonic vortices. Streamlines that contain the center of the annulus correspond to the strong counter-rotating jet which travels along the periodic azimuthal direction. These structures are visible in the streamlines of the flow field; they are also visible in the vorticity and shear plots as we will see in the upcoming subsections.

4.1.1 Velocity vectors: Mean jet

The first thing we resolve in the data is the strong anti-cyclonic jet, which is visible in the velocity field for both the 2D and 3D cases in Fig. 4.2. This jet is produced by the radial flux of water from the forcing holes (shown by the dashed and dotted lines), and is quite strong in the rotation frame of the tank. The mean azimuthal velocity in the 2D case is 30 cm/s, and 12 cm/s in the 3D case. It is clear from this figure that the jet fills the width of the tank.

4.1.2 Streamfunctions: Jet and vortices

Very little structure is visible in this vector field, due to the high mean velocity of the jets which carry the vortices in them. To obtain more detail, we compute the streamfunction of each flow. This is done with a matlab routine¹ which numerically integrates the velocity field; with only minimal smoothing, we can obtain clean contour plots of the streamfunction, as shown in Fig. 4.3. Here, the jet is still visible, but we see some small vortices on the periphery of the flow, e.g. at 3 o'clock and 9 o'clock in the 3D case. The structures are advected by the mean jet, so it is not surprising that they are not very distinct from it in a streamfunction plot. In the streamfunction contours, the regions of high density of contour lines correspond to regions of high velocity. This means that the flow velocities are high between the vortices, and small at their centers, as one would expect.

¹Written by Mark Shattuck.

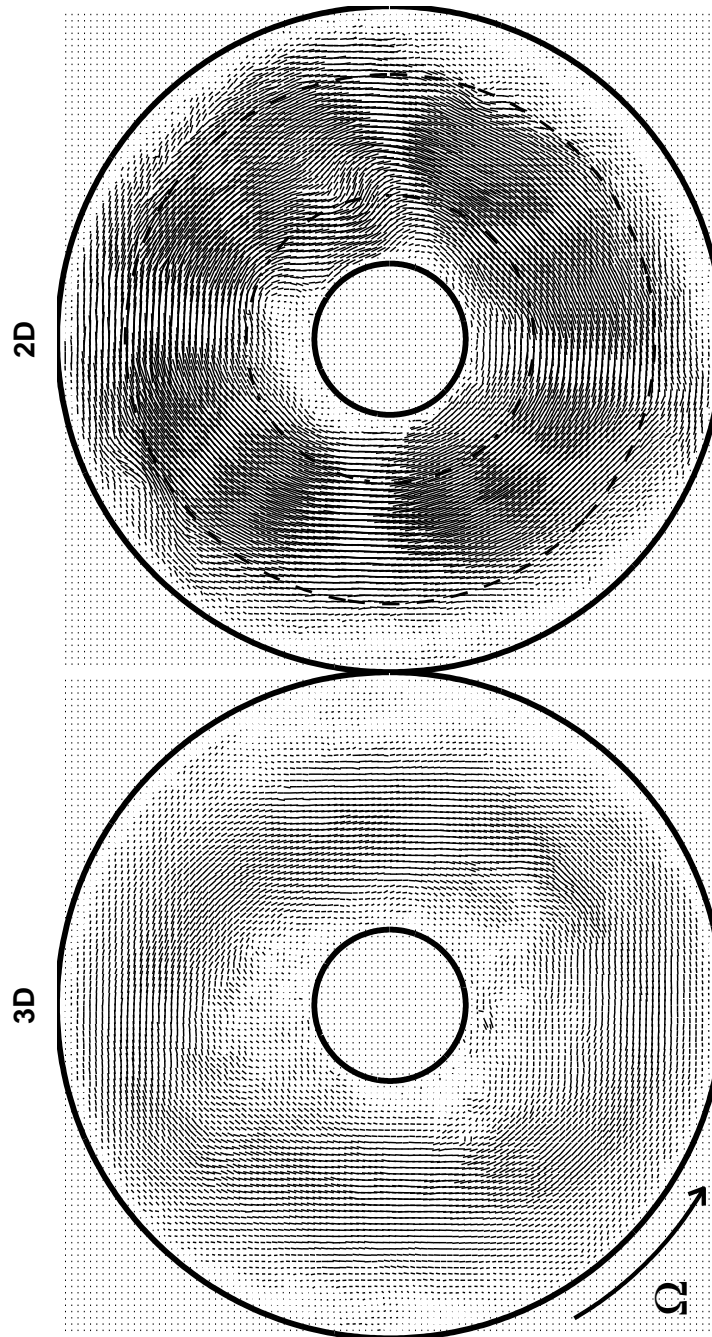


Figure 4.2: Velocity field for the 3D ($\Omega = 1.57$ rad/s, $Q = 550$ cm³/s) and 2D ($\Omega = 11$ rad/s, $Q = 350$ cm³/s) cases.

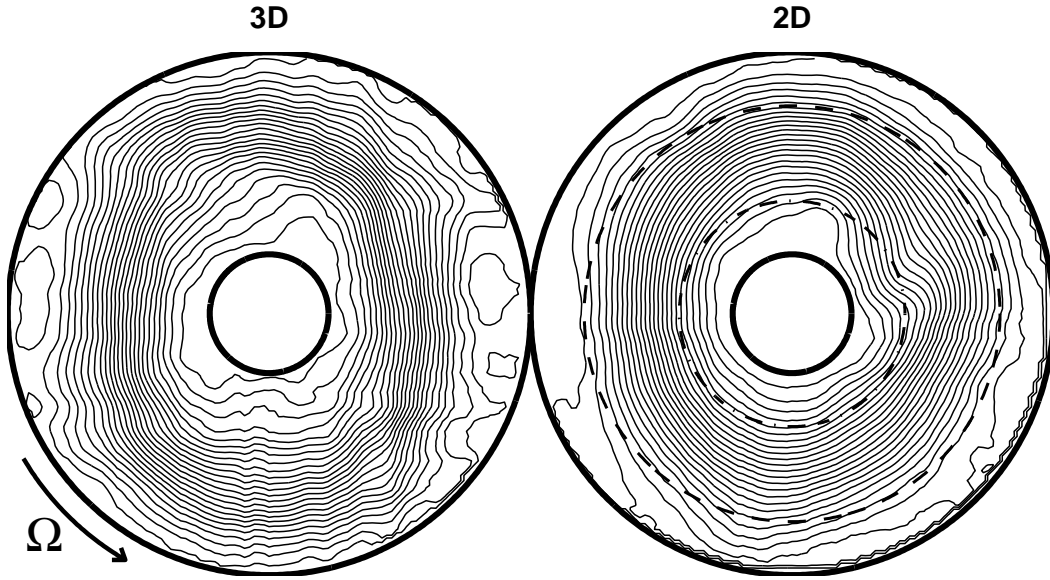


Figure 4.3: Streamfunction contours. Same conditions as Fig. 4.2. Contour line spacing corresponds to a flux of $12 \text{ cm}^2/\text{s}$ in the 3D case and $30 \text{ cm}^2/\text{s}$ for the 2D case.

In order to bring out the distinction between the jet and the vortices, we rotate the velocity field by the mean rotation rate of the flow, as described in Section 3.4.4. Under that transformation, large distinct structures in both the 2D and the 3D cases are seen relative to the mean flow. These large vortices form soon after the initiation of the pumping, and once they form they are stably advected along with the mean jet. The vortices interact with each other and with the boundaries, as well as with any smaller structures that are formed in the flow; structures of the same vorticity tend to merge together while vortices of opposite sign repel. In the 3D case, the largest vortices usually reach a steady size and do not grow or breakup. In the 2D case however, the largest vortices can sometimes grow to fill most of the tank in the azimuthal direction, at which point they usually break into two or three smaller parts. These parts separate and act as distinct vortices until they either dissipate some of their energy or eventually merge and grow again. The

large vortices in the 3D flow of Fig. 4.4 are locked to the mean jet, and they do not directly interact among each other. In the 2D case, the two large structures combine to almost fill the tank completely; they are actually the result of the breakup of a single large vortex a few seconds earlier.

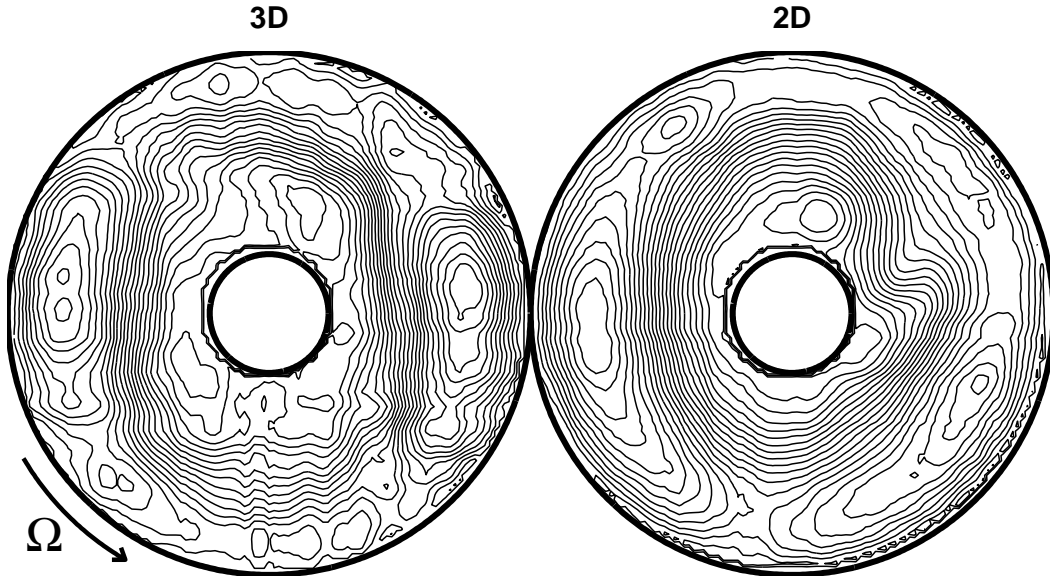


Figure 4.4: Streamfunction contours with mean rotation subtracted. Same conditions as Fig. 4.2.

The number of large stable vortices varied with rotation and pumping rates. Sommeria et al. [89] found the number of vortices to decrease with stronger pumping. Our experiments operate in a different parameter regime with higher pumping and lower rotation rate. We found that one large vortex was present for the more 2D flows, while the more 3D flows allowed the existence of two vortices. The lowest rotation rate and highest pumping rate sometimes produced three stable vortices, but those cases were not studied here. We relate this effect to a weaker inverse cascade in the case of the lower rotation rates. While the inverse cascade is still present and does lead to the merging of small structures into large ones, the largest scales do not reach the scale of the system. The number of vortices is plotted in

Fig. 4.5 as a function of rotation and pumping rates.

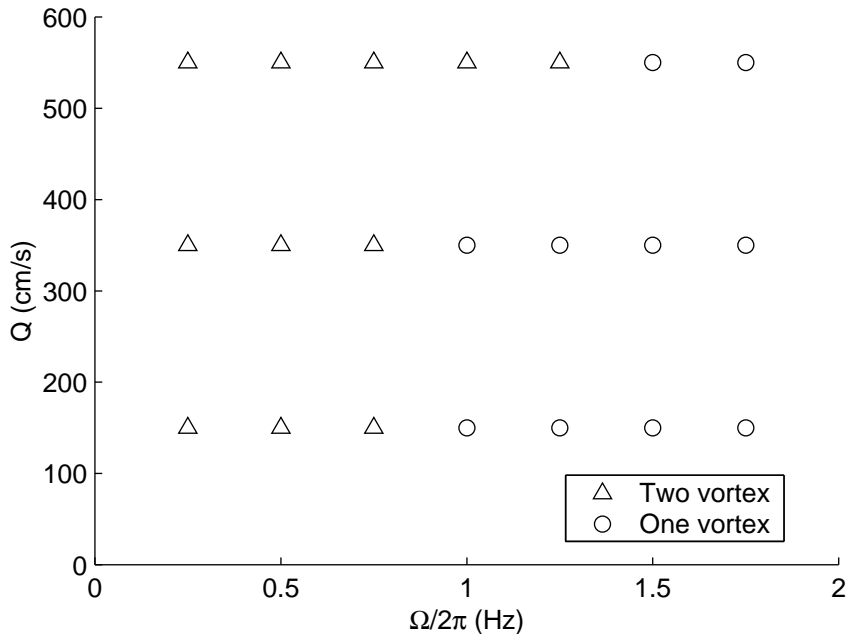


Figure 4.5: Number of large stable vortices (spots) for different pumping and rotation rates.

4.1.3 Vorticity and shear: Vortex interactions

Furthermore, note that there are vortices on both the inside and the outside of the jet, i.e. towards the center and the edge of the annulus. Since the jet represents a maximum in velocity, this means that the velocity gradient on the outside has a different sign from the gradient on the inside. This is evident in a plot of the vorticity (Fig. 4.6(a,b)). Here, we superpose the streamfunction from Fig. 4.4 with the vorticity field to show the correspondence between the structures and the vorticity. The colorbars correspond to vorticity, and indicate that the vorticity is mainly negative (cyclonic in this case) near the outside of the tank, and positive (anti-cyclonic) near the inside. Note that the sign of the tank rotation is arbitrary, and we chose to make anti-cyclones positive for clarity. However, the dominant sign

of vorticity is always anti-cyclonic near the inside of the tank for a counter-rotating jet, which can easily be shown from geometric considerations [53].

Vorticity maps contain very useful and important information about the flows in our study. The 2D flow is a very good approximation to the case of ideal flow, i.e. an inviscid 2D flow. In such flows, vorticity can only be created at the boundaries; in the bulk, it is a passive tracer which follows material movement. Since our system is forced, vorticity is generated in the bulk of the flow as well, but vortex motion still corresponds very well with material motion. In the 3D case, the vortices which are visible are 2D slices of a 3D field. This is especially true of the small structures. Information in the vertical dependence of these structures is not known, but they probably twist and connect with other structures elsewhere in the flow.

In the 2D plot, note the presence of a cyclone (dark centered-vortex) close to the center of the tank near 2 o'clock. Also visible is an anti-cyclone near the outer wall at 6 o'clock. These vortices are opposite to the dominant sign in their respective regions. They are formed at the recirculation region of the large stable vortices, where the velocity gradients are reversed. The 2D nature of the flow is such that these vorticity patches grow and form coherent vortices. Because these "tornadoes" have the wrong sign vorticity, they get ejected radially to the opposite side of the tank, where they match the background. The effect of these ejected vortices depends strongly on the rotation rate, and seems to play a major role in the dynamics of the flow, so we will come back to them in later sections.

Next, we turn our attention to the shear field, which is computed using Eq. 3.7 in the previous chapter, and shown in Fig. 4.6(c,d). In both the 2D and 3D cases, the shear is dominated by radial structures which correspond roughly to the edges of the vortices. This shows that the shear in the turbulent field is dominated by the azimuthal derivative. This is especially true for the ejections noted above: they correspond to regions of intense shear which changes sign rapidly. It should

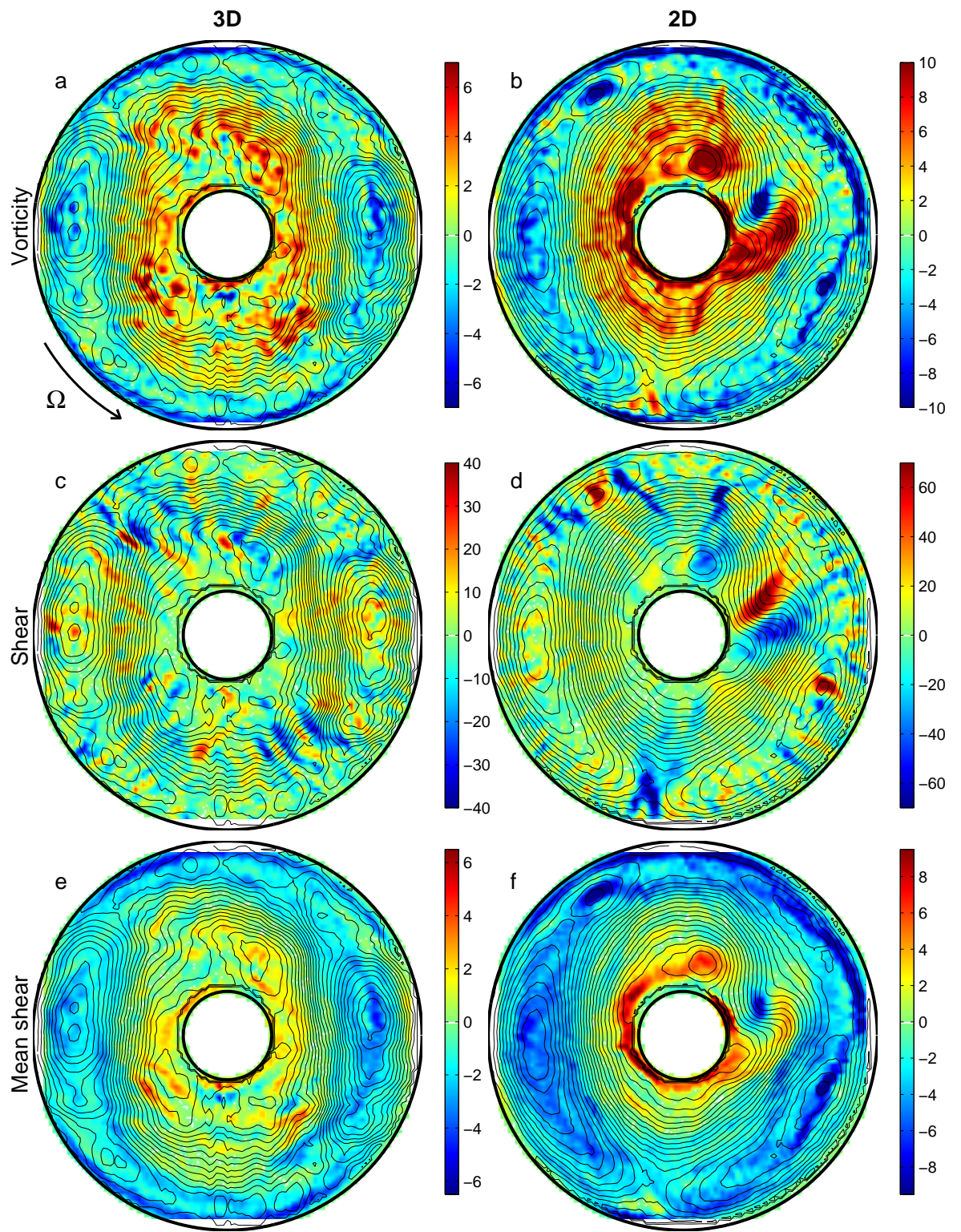


Figure 4.6: Vorticity (a,b), polar shear (c,d) and mean shear (e,f) fields. Same conditions as Fig. 4.2. Note the location of the change in sign of vorticity ω compared with mean shear $\bar{\sigma}$. Full shear is dominated by radial structures.

come as no surprise that these regions of high shear act to deform fluid parcels and to carry them quickly into different regions of the flow.

It is the “background shear” ($\bar{\sigma}_{r\phi}$) of Fig. 4.6(e,f) , defined in Eq. 3.8 that explains the reason for the radial ejections. By ignoring the azimuthal derivative of the velocity field, we obtain the shear field due to the mean motion of the jet. This shear is much weaker and varies over longer distances than the full shear of Fig. 4.6(c,d). The dominant feature of this field is that, like the vorticity, the shear is mainly cyclonic near the outside of the tank and mainly anti-cyclonic near the inside. This is important because a vortex which has the same sign as the background shear is stable until it merges with another vortex of the same sign. A vortex whose sign is opposite that of the background shear cannot remain there: it gets ejected radially across the channel to the region with the same sign shear. In some situations, such a vortex can also lose much of its energy through stretching and shedding of vorticity filaments, as in the case the vortex at the bottom of the 2D field (Fig. 4.6(a,b)), where the ejecting anti-cyclone is deformed by the mean jet. Such a vortex might completely lose its coherence as it moves radially, but if it crosses the jet maximum without dissipating its energy, it survives until it merges with another vortex of the same sign.

4.1.4 Ejection events

In the 3D field of Fig. 4.6(a,b), also visible is a small ejection occurring at the inner wall, near the top of the annulus. The signature of this ejection is also visible in Fig. 4.6(c,d), where a region of high positive shear is present at the edge

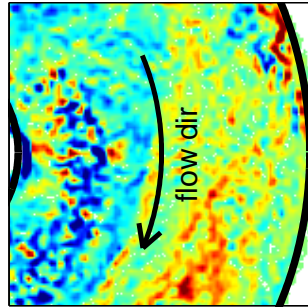
of the anti-cyclonic large vortex. The 3D ejections are more difficult to see, due in part to their small size. In contrast, 2D ejections occur at a wide range of sizes and are often easy to follow between frames.

To emphasize the difference between the 2D and 3D ejections, we look at two closeups of ejection events at low and high rotation rates, shown in Fig. 4.7. Two ejection events can be followed in the low rotation (3D) case: As the cyclonic (red/yellow) structure sweeps past, we see the formation of a weak anti-cyclone (blue) at the outer wall, marked with the circle at $t = 1.0$ s. This small vortex extends radially and some of the fluid is carried inward. A similar process happens near the inner wall as the strong anti-cyclone (blue) causes a cyclonic (red) ejection (circle at $t = 3.0$ s). Note that the ejecting structures are small in size and consist of several small vortices orbiting each other.

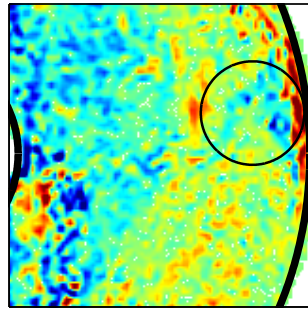
In the high rotation case, the ejecting anti-cyclone forms at the outer wall and grows to about 10 cm in size before being transported across the jet to the anti-cyclonic region of the flow. We can see that it is connected to a thin anti-cyclonic region near the wall, and it grows by drawing fluid from this boundary region. In the last frame ($t = 0.9$ s), it appears that this vortex is being elongated and sheared by the jet. For the conditions of this sequence, the maximum velocity in the jet can reach 80 cm/s near the center and has to go to zero at the edge. Therefore the velocity gradients can be quite large and the shear felt by an ejecting vortex can be very significant as it tries to circumvent the large cyclonic vortex.

We also see in this sequence several cyclones being carried in the jet. The cyclones reach the region of favorable shear sooner than the anti-cyclones, as seen in Fig. 4.6(e,f), so they are more likely to preserve their shape and to get carried azimuthally without losing their coherence. The size of the ejecting vortices varies with rotation and pumping rate; these vortices are always small in the 3D case, while the 2D vortices can have a range of different sizes and strengths.

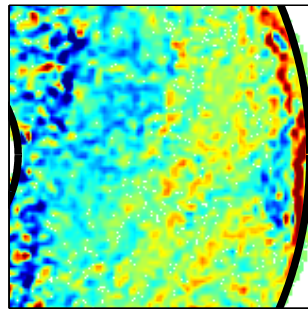
$\Omega=1.57$ rad/s, $Q=350$ cm³/s



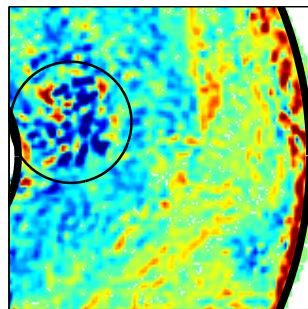
t=0 s



t=1.0 s

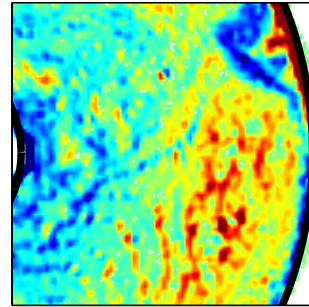


t=2.0 s

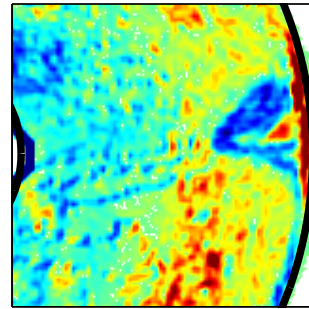


t=3.0 s

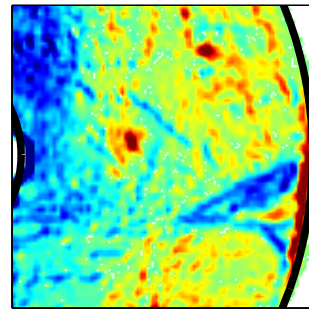
$\Omega=11.0$ rad/s, $Q=550$ cm³/s



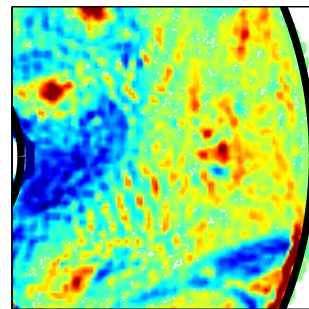
t=0 s



t=0.3 s



t=0.6 s



t=0.9 s

Figure 4.7: Two ejection events, at low and high rotation rates. See text for discussion.

The ejection events and the later merging between the ejected vortices and the large coherent structures can be thought of as a non-local dynamics. Here, non-local refers to locality in wavenumber space, and the non-locality is the interaction between structures of highly different sizes. The creation of the small vortex can be thought of as a large-scale dissipation mechanism, where energy from the largest scales is being drawn out and injected back at a smaller scale. Once the vortex is ejected, it can get sheared by the mean jet (e.g. the anti-cyclone near the bottom of Fig. 4.6(a,b)), or it can cross the jet and merge with the large vortices on the other side, thus cascading energy back up to the large scales. The existence of strong non-local interactions was found to increase the amount of intermittency in numerical simulations [52], which is consistent with our observations.

The motion of the 2D vortices corresponds to advecting fluid parcels, as expected for 2D inviscid flow (ideal flows). The image in Fig. 4.8 was taken during the transient stages, shortly after the formation of the largest structures, so the slightly heavier particles have had several minutes to centrifuge to the outer edge of the annulus in the absence of any turbulent mixing. An ejection event near the top of the annulus carries these particles into the bulk of the flow. This ejection can also be followed in the vorticity map. The later motion of these particles corresponds very well with the motion of the vortex as the latter crosses the center jet. This is confirmed by the group of particles marked with the square, and the corresponding vortex in the vorticity field.

Also visible in this figure is the spiral nature of the ejection events. The vortices that form in the recirculation regions of the large stable vortices are effectively “rolled up” at the stagnation point by the mean jet. This is visible in the spiral structure in the particle image near the top, and also near the bottom of the figure.

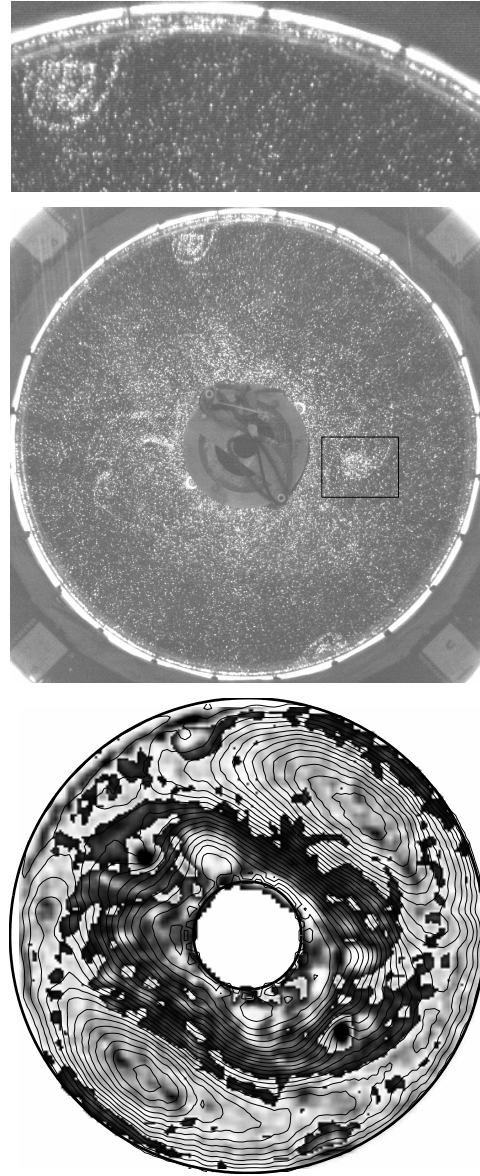


Figure 4.8: Particle ejections (top) and corresponding vorticity and streamfunction fields (bottom), $Ro = 0.14$, $\Omega = 6.28$ rad/s, and $Q = 150$ cm³/s. The particles ejecting near the top indicate the spiral structure of the ejecting vortices. Structures with a dark center are cyclones while those with a light center are anti-cyclones. Streamline spacing is 19 cm²/s.

These vortices give further support for the applicability of spiral vortex model.[57]

4.2 Evidence of two-dimensionalization

From the above analysis, it is clear that the slow-rotation and fast-rotation flows are very similar. They all consist of a strong counter-rotating jet which is populated by vortices of varying sizes. This suggests that even at the low rotation rates, the rotation is already an important factor which inhibits the stretching of vortex tubes. This is indeed true for the cases shown above, since the typical Rossby numbers are all below one. In this section we show the initial moments of the flow evolution, which underscores the important role of rotation and shows a clear example of an inverse energy cascade. In the second part of this section, we show evidence of a much more 3D flow at a rotation rate $\Omega = 0.79$ rad/s (1/8 Hz). This flow is shown as an extreme example, but the statistical analysis in the later sections will be done for rotation rates starting at 1/4 Hz.

4.2.1 Flow development

Evidence of an inverse energy cascade is visible during the initial moments of our flow setup. If the pumping is started after the water has reached solid body rotation, small anti-cyclonic and cyclonic vortices form above the inlet and outlet holes respectively. The vortices are smaller and weaker than the resolution of the PIV, but within a short time, like-sign vortices start to merge together and grow, cascading energy to the larger scales as shown in Fig. 4.9. The radially outward flux from the pumping simultaneously generates a strong counter-rotating jet between the forcing rings. The jet grows in strength until the pumping is balanced by the Ekman dissipation in the top and bottom boundaries. This behavior is found for all rotation rates in the range $1.57 < \Omega < 14.1$ rad/s, and we expect that the same behavior continues for higher rotation rates. The evolution rate however does

depend on the experimental conditions.

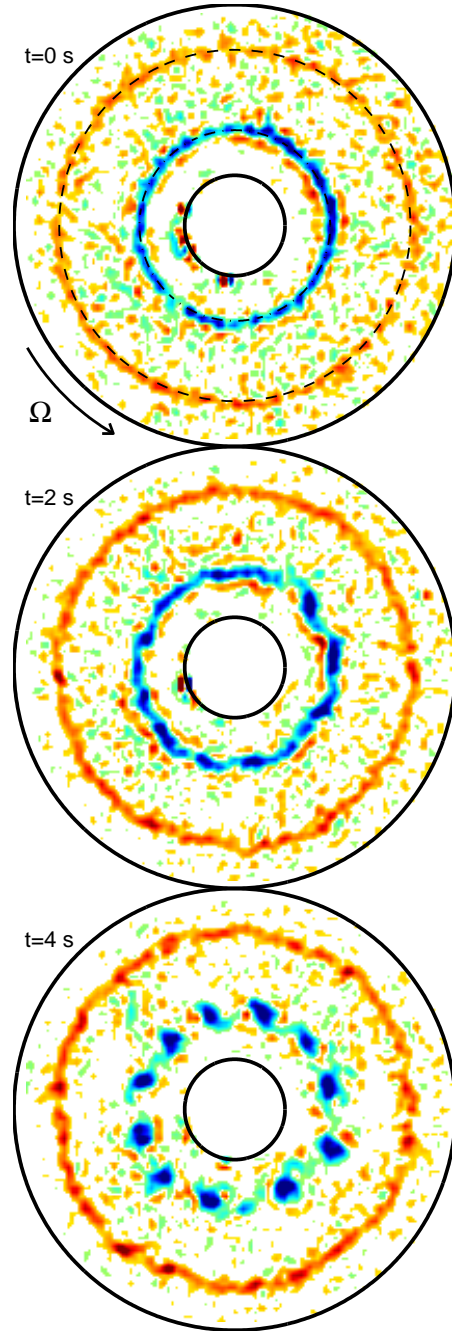


Figure 4.9: Initial moments of the flow setup ($\Omega = 6.28$ rad/s). A ring of anti-cyclones (blue) initially forms above the inlet holes, and cyclones (red) above the outlets. The interaction between vortices causes them to elongate and create spiral structures. In this figure, we threshold the values of vorticity and show only those values that are significantly above the noise, for clarity. The vorticity values are different for different times.

The vortices which form above the forcing holes interact with their immediate neighbors in groups of two or three. For instance, a group of three anti-cyclones might start to orbit each other initially. The vortex centers would then get pulled in towards the center of the trio, thus creating an elongated structure similar to a backwards “S”. The new vortex then keeps rotating with stronger vorticity, and the lobes from the “S” get wrapped around the central core of the vortex. The orbiting and merging steps repeat with the larger structures until the interactions with the walls become important. This process is similar, if not identical, to the one suggested by Lundgren[57] for the formation of spiral vortices. One expects that the vortices still display a spiral structure at later times, although our visualization does not resolve those details.

4.2.2 Lowest rotation 3D flow

In order to show the existence of a clearly 3D flow, a set of PIV data was taken at $\Omega = 0.79$ rad/s (1/8 Hz). This low rotation rate is more significant than the case with no rotation at all, since we can start to see hints of the “jet and vortices” structure seen at the higher rotation rates. Although oscillations in the tank rotation rate make hot-film measurements difficult at these slow rotations, PIV data is largely unaffected since the camera rotates independently, and since the oscillations have little effect on the flow outside the boundary layer. A snapshot of a flow at this rotation rate, with $Q = 550$ cm³/s shown in Fig. 4.10.

$\Omega=0.79$ rad/s, $Q=550$ cm³/s

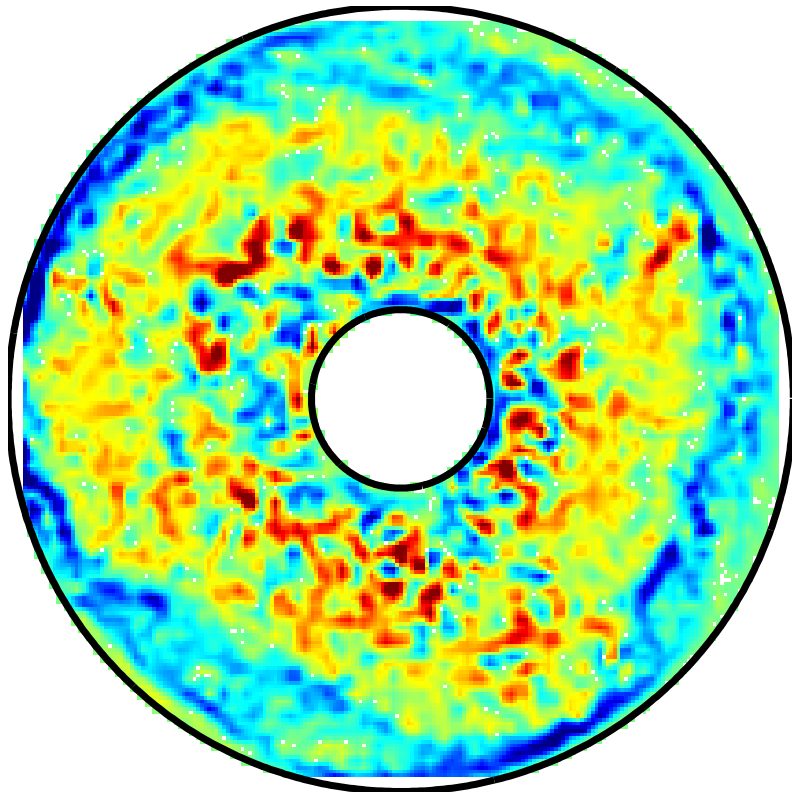


Figure 4.10: Low-rotation flow ($\Omega = 0.79$ rad/s, or 1/8 Hz, $Q = 550$ cm³/s) showing strong signs of three-dimensional turbulence. Vorticity range is $-5 < \omega < 5$ s⁻¹.

The first observation is the existence of very small, strong vortices of both signs near the inner region of the flow. Recall that these vorticity patches are a 2D slice of a 3D field, so that the vortices might be oriented in different directions. A stream function contour of this flow would show very little detail, so it is not shown. However, we do see the formation of larger vortices, similar to the fast rotation rates, near the outer wall; these vortices however remain much smaller and weaker than in the previous figures. They get carried azimuthally by the weak jet, as in the other cases.

Note that this flow does not show the same evolution as the faster rotation cases. The vortices that form above the forcing holes do not merge together to produce larger ones, hence there is no inverse cascade. Instead, strong anti-cyclones produce cyclonic vortices near them, and vortex pairs of opposite signs orbit each other, interacting with other vortex pairs in a very complicated dance.

The “3D” flow in Fig. 4.6(a,b) shows a similar region of anti-cyclones in the cyclonic region, and vice-versa. These vortices are small (~ 1 cm) and relatively short-lived. The presence of these small eddies is evidence that the inverse cascade (i.e. the mechanism that pushes the vortices to merge and grow) is very weak for the low rotation rates. One expects that as the rotation rate is increased, the inverse cascade gradually becomes stronger, and the 2D approximation improves until it becomes very closely applicable at the high rotation rates.

4.2.3 Top-bottom cross correlation

Finally, strong evidence of the two-dimensionalization comes from the cross correlation of the time series from two probes placed above one another. The two probes are at the same azimuthal and radial position, one near the top lid and one near the bottom. The cross correlation coefficients for a range of pumping and rotation rates are shown in Fig. 4.11. Although the value of the coefficients never

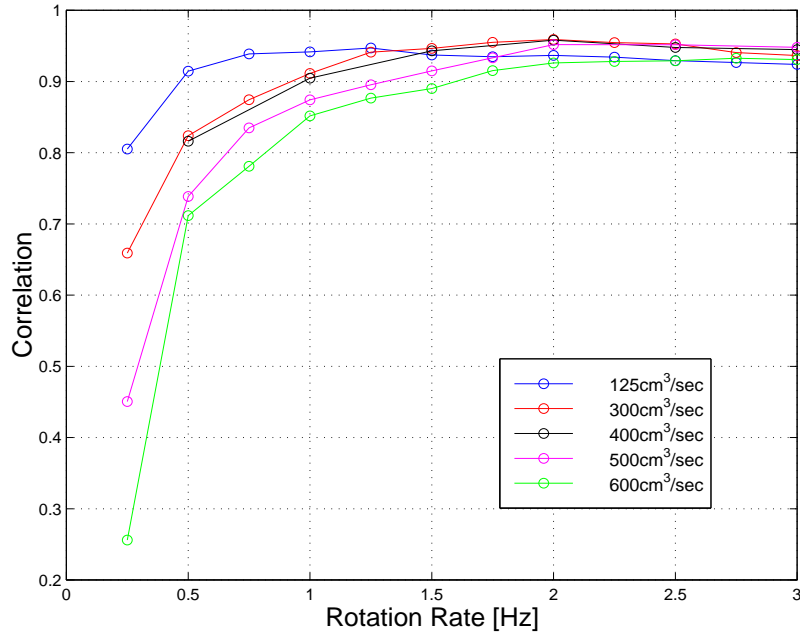


Figure 4.11: Linear correlation values for different rotation and pumping rates. Error bars on this data are unknown.

reaches 100% (possibly due to noisy time series), we see that the cross-correlation is above 90%, independently of the pumping rate for $\Omega/2\pi \geq 1.75$ Hz.

This high correlation coefficient is evidence that largest structures are columnar, or that the flow motion is mainly parallel to the axis of rotation. The small scale structure in the flow might still be different, although a detailed study has not been done.

4.3 Mean quantities

The next step after the general description of the vortices and their interactions is to describe some mean quantities of the flow. These quantities can provide a better theoretical understanding of the flow, as in the case of the force balance. Understanding the mean velocities and length scales can also provide typical values

to be used in the definition of the dimensionless numbers.

4.3.1 Radial profiles

In this section, we consider the following parameter values: $Q = 150 \text{ cm}^3/\text{s}$ and $\Omega = 11.0 \text{ rad/s}$ for the 2D case and $Q = 550 \text{ cm}^3/\text{s}$ and $\Omega = 1.57 \text{ rad/s}$ for the 3D case. These values are chosen because they yield similar velocity scales, and they also correspond approximately to the values used in obtaining the long time series. From the visualization data, the radial profiles of velocity, vorticity and shear are plotted in Fig. 4.12 for the 3D and 2D cases. Here, the quantities are averaged azimuthally and over several snapshots to give a good approximation to the true mean radial profile.

In both cases, the jet fills the width of the tank and the velocity profile has a clear maximum between the forcing rings. The location of this maximum moves slightly towards the outside of the tank as the pumping is increased, for all rotation rates. This means that for a fixed value of the maximum velocity, the total kinetic energy in the flow is increased since a larger volume of water is displaced at the outer radii.

The 2D vorticity profile displays a central region where the vorticity of the flow increases almost linearly. This region corresponds to the region with the strong jet, away from the large coherent vortices that travel near the inside and outside walls. The signature of the vortices is found to be a plateau of vorticity near the walls. For the 3D flow, the central region is not linearly increasing, but one can still differentiate between a “jet” and a “vortices” regions.

The polar shear is defined in Eq. 3.7 as

$$\sigma_{r\phi} = \frac{r}{2} \left[\frac{\partial(u_\phi/r)}{\partial r} + \frac{1}{r} \frac{\partial u_r}{\partial \phi} \right] \quad (4.1)$$

where u_ϕ is the azimuthal velocity and u_r is the radial velocity. In the case where the azimuthal variations can be ignored, the ϕ derivative can be dropped and we

compute the mean shear as

$$\bar{\sigma}_{r\phi} = \frac{r}{2} \frac{\partial(u_\phi/r)}{\partial r}. \quad (4.2)$$

In our turbulent flows, the shear at each time step is actually dominated by the ϕ derivative, as shown in Figs 4.6(c,d) and 4.6(e,f). However, when we average over many snapshots, we are left with a curve more similar to that obtained from Eq. 4.2. The value from Eq. 4.2 is plotted in Fig. 4.12 because it yields a higher signal-to-noise ratio, since we are not averaging large positive and negative numbers.

The shape of the curve for shear is similar to the shape of the vorticity curve. One important difference however is that the shear ($\bar{\sigma}_{r\phi}$) changes sign at a different radial location than the vorticity (ω). The large coherent vortices of Fig. 4.6(a,b) are only stable in the region where $\bar{\sigma}_{r\phi}$ and ω are of the same sign, as previously discussed by Marcus [58]. In the region where the shear is adverse, the vortices can dissipate through the shedding of filaments of fluid, or by elongating in the plane of the flow and losing their coherence. Therefore the change in the jet profile can be related to the size of the structures in it.

Finally, note that the vorticity and shear profiles might be affected by the location of the forcing holes; the details of this dependence are left to future study.

4.3.2 RMS velocity

The azimuthal velocity of our flow is set by the balance of the torque due to the Coriolis force and the torque from the Ekman dissipation. Sommeria *et al.* [89] derived an approximate formula for the maximum velocity based on this balance:

$$u_\phi = \left(\frac{b}{a^2}\right)^{1/3} K(Q\Omega)^{2/3} \quad (4.3)$$

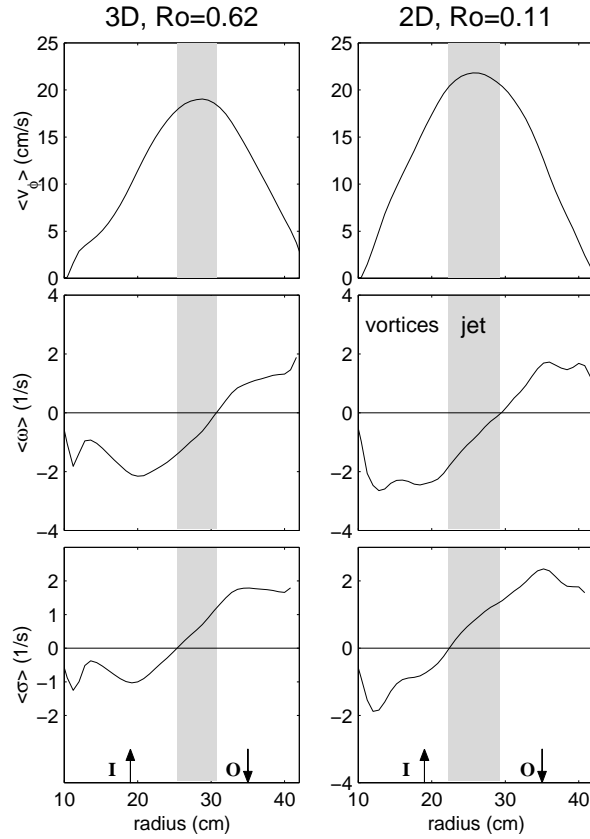


Figure 4.12: Radial profile of azimuthal velocity (u_ϕ), vorticity (ω), and mean shear (σ) for the 2D ($\Omega = 11.0$ rad/s, $Q = 150$ cm³/s) and 3D ($\Omega = 1.57$ rad/s and $Q = 550$ cm³/s) cases. The shaded areas correspond to regions where the vorticity is positive and the shear is negative, where coherent long-lived vortices cannot survive.

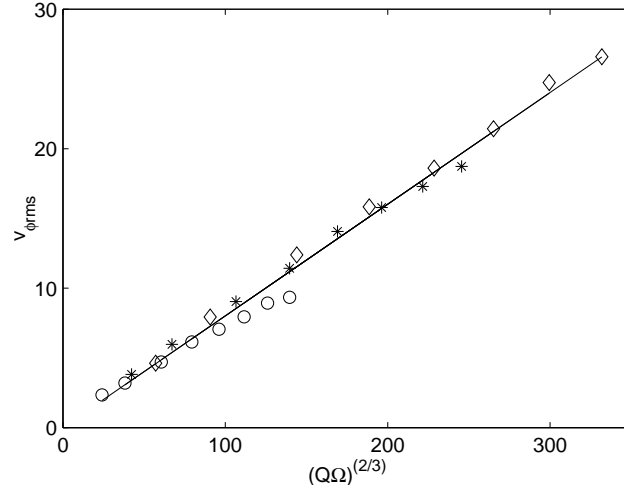


Figure 4.13: RMS azimuthal velocity plotted vs. $(Q\Omega)^{2/3}$ for $Q = 150, 350, 550 \text{ cm}^3/\text{s}$ (o, *, and \diamond respectively), and $0.78 \leq \Omega \leq 11.0 \text{ rad/s}$. The solid line is a linear fit to the data, giving a slope of 0.08, and an intercept of 0.02. The corresponding $b/a^2 = 0.37$

where K is a constant which depends on the tank geometry and fluid viscosity², and a and b are constants that depend on the shape of the jet. From the PIV data, one is able to obtain the root-mean-squared (rms) velocity for all rotation and pumping rates. A plot of this velocity vs. $(Q\Omega)^{2/3}$ is shown in Fig. 4.13, and the values are shown in Table 4.1. Table 4.2 shows the values of the maximum velocity, computed as $v_{\text{mean}} + 2\sigma$ where σ is the standard deviation, which show a similar scaling with $(Q\Omega)^{2/3}$.

The shape of the jet can vary significantly over the wide range of pumping and rotation rates, making a single value for a or b misleading. Nevertheless, the observed linear dependence of the velocities on $(Q\Omega)^{2/3}$ supports the theory that the Ekman dissipation is the main mechanism limiting the azimuthal velocity. A similar plot (not shown here) can be made for the maximum velocity and gives a

² $K = \left(\frac{sd^2}{2\pi^2\nu h_0 \langle r \rangle^2} \right)$, where s is the slope, d is the distance between the forcing rings, h_0 is the mean height, and $\langle r \rangle$ is the mean radius. $K = 0.21$ for our flows.

similarly good fit.

4.3.3 Reynolds and Rossby numbers

Dissipation does not play an important role in our experiments; we quantify that by computing the Ekman number ($Ek = \nu/2\Omega L^2$ where ν is the kinematic viscosity, Ω is the rotation rate, and L is a characteristic length), which compares the viscous effects to the Coriolis term. The Ekman number is always small in our experiments ($10^{-5} < Ek < 10^{-4}$), indicating that the viscous effects are always negligible. Related to the Ekman number is the Ekman spin-down time, $\tau_{Ek} = h_0/2(\nu\Omega)^{1/2}$ where h_0 is the mean height of the tank. This time scale should be long compared to the typical turnover time of vortices for dissipation effects to be weak. We find that τ_{Ek} for our experiments are always larger than 80 s, much longer than the other time scales in our flow.

In the absence of dissipation effects, two dimensionless numbers are important in characterizing our flows: The Reynolds number ($Re = UL/\nu$ where U is a typical velocity), and the Rossby number ($Ro = \omega/2\Omega$ where ω is a typical vorticity) which describes the importance of rotation. One can also define a “global” Rossby number ($Ro_g = U/2\Omega L$), although this definition would require us to extract a subjective length scale from the flow. Some representative Reynolds and Rossby numbers are shown in table 4.3, corresponding to all the hot film data and some important PIV data conditions.

Table 4.1: RMS velocities plotted in Fig. 4.13.

Q	$\Omega = 0.79$	1.57	3.14	4.71	6.28	7.85	9.42	11.0 rad/s
150 cm ³ /s	2.35	3.19	4.72	6.15	7.06	7.95	8.93	9.34
350 cm ³ /s	3.82	5.98	9.04	11.4	14.1	15.8	17.3	18.7
550 cm ³ /s	4.63	7.94	12.4	15.8	18.6	21.4	24.7	26.6

The Reynolds number is kept approximately constant for the long time series, as shown in the table, which allows us to isolate Rossby number effects on the turbulence. The pumping rate is reduced as the rotation rate is increased in order to keep $U_{\max} \simeq 20$ cm/s, as measured by the hot-film probes. The Reynolds number, using the mean azimuthal velocity (averaged over the whole annulus) and the distance between the forcing holes (16.2 cm) for L , is always in the range $1.4 \times 10^4 < Re < 2.0 \times 10^4$. We also compute the Taylor scale Reynolds number, based on the Taylor microscale ($\lambda^2 = \langle (\partial_x u)^2 \rangle / u_{\text{rms}}^2$) and the rms velocity, which allows us to better compare with other experiments. Our value for Re_λ remains fixed at $Re_\lambda \simeq 360$, with $\lambda_{2D} \simeq 2.0$ cm in the fast rotation case and $\lambda_{3D} \simeq 1.8$ cm for slow rotation.

The Rossby number can be thought of as a ratio of time scales: It compares the rotation period of the system ($1/\Omega$) with the typical turnover time of vortices ($1/\omega$). A small Ro indicates a flow where the Coriolis effects from the tank rotation are dominant, and the flow is expected to approach a 2D state. The complete range of our Rossby numbers from PIV and hot film measurements is plotted in Fig. 4.14 as a function of rotation and pumping rates.

For a fixed pumping rate, the reduction in Ro is clear, and we are able to cover a fairly large range. However, a surprising fact is that Ro for high-pumping/high-rotation flows are as high as the ones for the low-pumping/low-rotation. This would indicate that a high-energy flow at 11 rad/s is as 2D as a lower-energy flow at

Table 4.2: Maximum velocities for the same conditions as in Fig. 4.13.

Q	$\Omega = 0.79$	1.57	3.14	4.71	6.28	7.85	9.42	11.0 rad/s
150 cm ³ /s	7.15	9.70	1.44	1.85	2.13	2.40	26.9	28.2
350 cm ³ /s	11.3	18.2	27.9	35.5	43.5	49.0	53.8	58.2
550 cm ³ /s	13.1	24.3	38.1	49.1	57.9	66.8	76.7	83.3

Table 4.3: Conditions for hot film (HF) and some sample PIV measurements. State I is strongly 2D while state IV is 3D. Re and Ro are based on a length scale $L = 16.2$ and the mean velocity, $\langle v \rangle$, as given.

	State	Rotation Ω (rad/s)	Pumping Q (cm ³ /s)	$\langle v \rangle$ cm/s	Re	Ro
HF and PIV	I	11.0	150	9.34	2.0×10^4	0.11
	II	6.28	150	7.06	1.5×10^4	0.14
	III	3.14	300	8.5	2.0×10^4	0.32
	IV	1.57	450	4.23	1.4×10^4	0.62
PIV only	V	0.79	550	4.63	0.89×10^4	1.1
	VI	0.79	150	2.35	0.56×10^4	0.49
	VII	11.0	350	18.7	3.0×10^4	0.21
	VIII	11.0	550	26.6	6.8×10^4	0.29

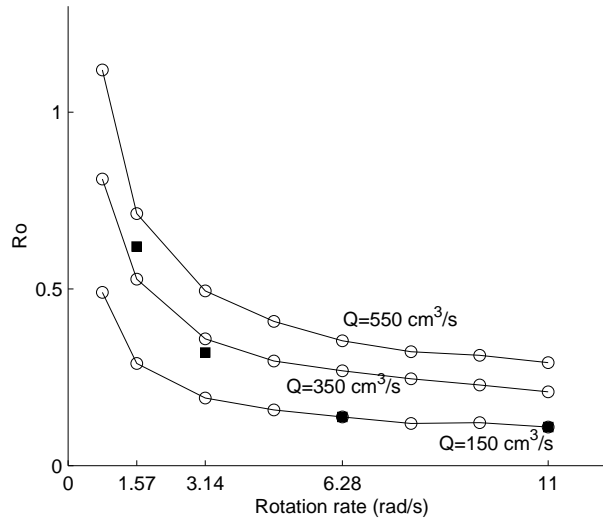


Figure 4.14: Range of Rossby number as a function of rotation and pumping rates. The solid squares are points where the hot film data were obtained.

1.57 rad/sec, a very surprising observation, especially in light of the cross-correlation values of Fig. 4.11. The same trends are found for Ro_g , although the actual values depend on the length scale used.

We suggest that it is possible that the Rossby number is not an accurate measure of the two-dimensionality of a turbulent flow, especially in the case where solid boundaries are present, or in the presence of 3D forcing. Further study is needed to fully determine the relationship between Ro and the two-dimensionality in our experiment, and to compare with numerical simulations [18, 15].

4.4 Time series

Now we make our way from the Leonardian realm to the statistical realm, by shifting our attention from the spatial description of the flows to the time series. The relation between the fluctuations in the time series and the structures in the flow are explored in Fig. 4.15. Here we plot a sample PIV field (where the annulus has been mapped onto a rectangle, as discussed in Section 3.4.4) and the corresponding azimuthal velocity at the radius of the hot film probes. In this geometry, the inner wall corresponds to the top of the figure, the outer wall is at the bottom, and the flow direction is left to right. Several vortices are visible in this flow. The most prominent is the one ejecting from the inner wall near $\pi/2$, with a dark center. Also visible is the large cyclonic vortex centered at $3\pi/2$; this structure is mainly visible through the streamlines closing, since its vorticity is not very large. It is broken by a highly elongated anti-cyclone which passes the hot film radius.

The sharp drop in the azimuthal velocity at $\pi/2$ corresponds to the large negative velocity due to the circulation of the ejecting vortex. The ejecting anti-cyclone also causes a small dip in the velocity near $5\pi/4$. Note that both a cyclonic and an anti-cyclonic ejections would cause a drop in the measured velocity, although the shape of the vortices being different, the drop might be smaller or shorter in the

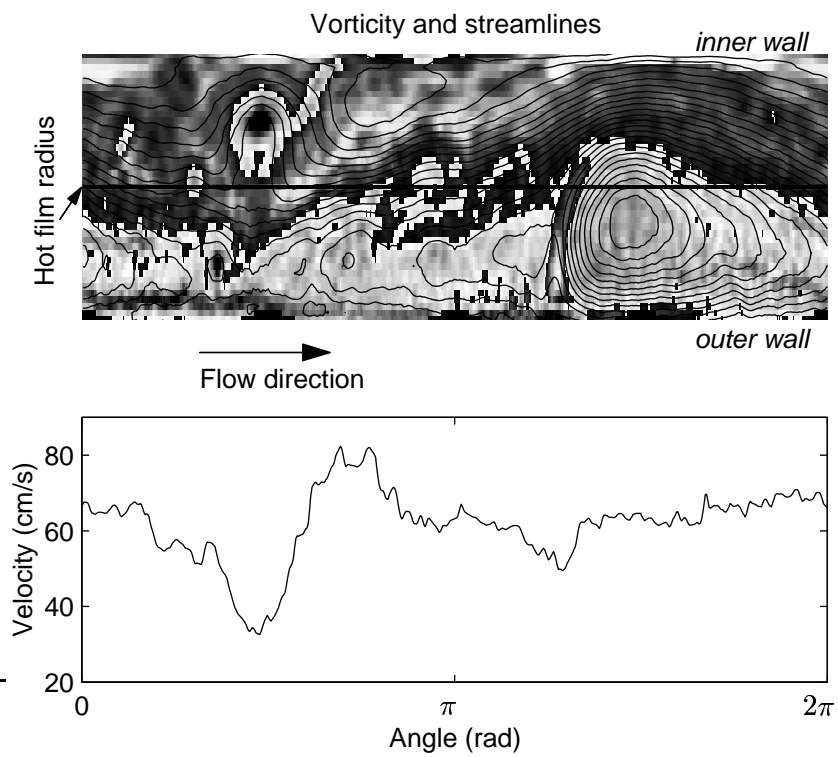


Figure 4.15: The annulus mapped onto a rectangle, showing the flow profile ($\Omega = 11.0$ rad/s, $Q = 550$ cm³/s) and the corresponding azimuthal velocity at the hot film radius. Here, vortices with a dark center correspond to cyclones, while vortices with a light center are anti-cyclones.

anti-cyclonic case.

The velocity time series measurements all display large low frequency oscillations, as shown in Fig. 4.16(a) and (c), which are very similar to the drop in Fig. 4.15. Superposed on those variations are high frequency “turbulent” fluctuations corresponding to the smaller structures being swept past the probe. Note that in these flows a 15 cm structure would sweep by in about 1 s and the dynamics at those scales are quite complex, as seen in parts (b) and (d) of Fig. 4.16. Both the 2D and the 3D flows look turbulent, and it is difficult to distinguish between them with only low-order statistics. It will become apparent in the next section that the distinction between 2D and 3D flows is pronounced when high-order methods are used.

The near periodicity in the time series is due to the periodicity of the annulus in the azimuthal direction. The long-lived structures sweep past the probes at regular intervals as they are carried along by the flow. At the lower rotation rates, the pattern of the flow is mostly fixed; it rotates carrying with it the structures that are visible in the vorticity field, which is the cause of the periodicity in the 3D case. In the 2D case, the vortices grow to a larger size, and they interact with each other. These interactions are strongly time-dependent and they break the periodicity as vortices merge or break up. However, all of these large fluctuations are well outside the range of length and time scales of interest in the turbulent statistics, and therefore they are not problematic in our statistical calculations.

4.5 Structure functions

As discussed in Chapter 2, the high-order structure functions (S_p) are expected to scale differently in 2D and 3D. In this section, these scalings are explored with emphasis on the differences between the 2D and 3D cases. The details of the 2D scaling in our experiment are studied in the next chapter, where we explore an

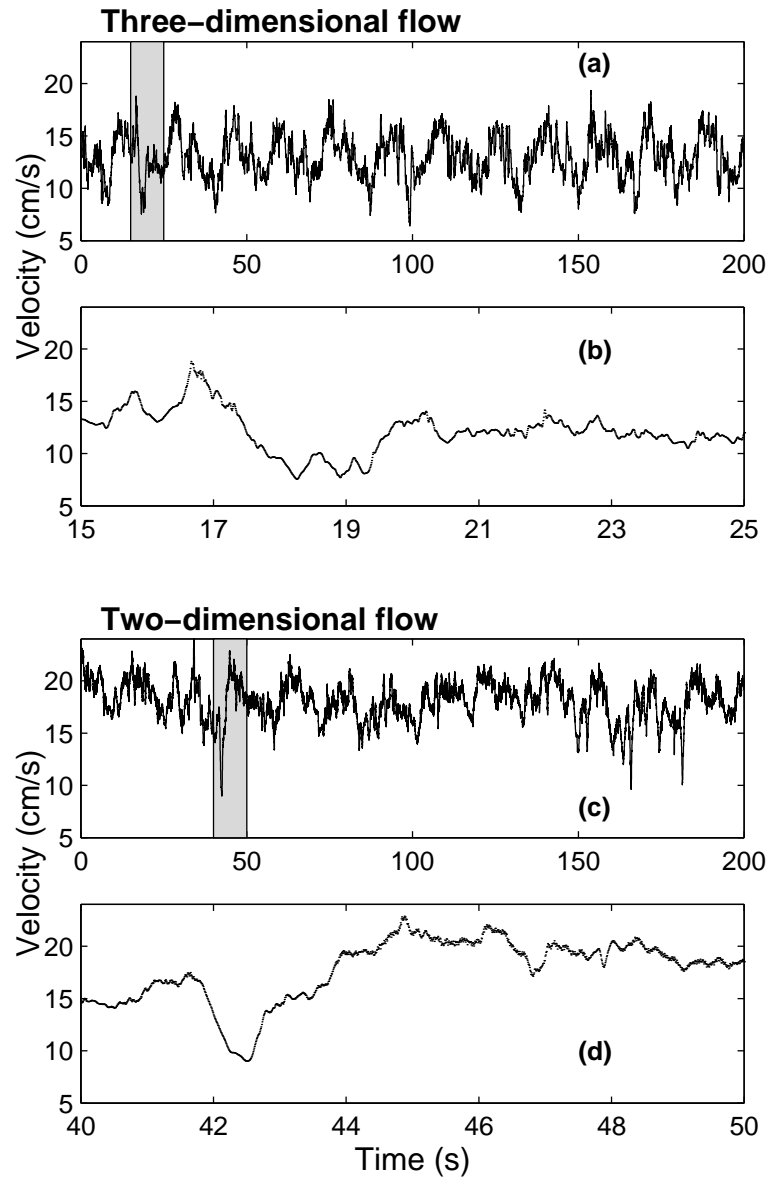


Figure 4.16: Typical time series segments and details for $\Omega = 1.57$ rad/s and $Q = 450$ cm³/s **(a),(b)** and $\Omega = 11$ rad/s and $Q = 150$ cm³/s **(c),(d)**. The large velocity drops correspond to regions in the flow where the velocity is deflected in the radial direction by the vortices. Note that a 15 cm structure would sweep past the probe in approximately 1 s, a time much faster than the slow fluctuations seen in the time series.

anomalous scaling that was not previously predicted for 2D turbulence.

The scaling arguments of the structure functions should apply in the inertial range, i.e. far from the Kolmogorov scale (η) and from the integral scale L_i . For 2D turbulence, this range is divided into a forward enstrophy cascade for wavelengths λ smaller than the injection length λ_i , and an inverse energy cascade for $\lambda > \lambda_i$ [49], as discussed previously.

Several length scales might act as injection lengths in our flow, but an important one is approximately $\lambda_i \simeq 2$ cm, corresponding to the distance between the forcing holes in the outer ring (see next chapter for a discussion). Therefore we expect both the forward and inverse cascades to exist, limited by the Kolmogorov length η at the small scales, and by the Rhines length λ_β at the large scales. The dynamics at the small scales however are complicated by the existence of two forcing lengths, corresponding to the distance between the holes at the inner and outer rings.

The Kolmogorov dissipation scale η is given by the fluid viscosity and the mean energy transfer rate,

$$\eta = \left[\frac{\nu^3}{\varepsilon} \right]^{1/4} \quad (4.4)$$

where we need to assume small-scale isotropy to estimate ε by

$$\varepsilon = 15\nu \left\langle \left(\frac{\partial u}{\partial x} \right)^2 \right\rangle = 15\nu \int k^2 E(k) dk. \quad (4.5)$$

The value of η remains nearly constant at $\eta \simeq 0.07$ cm for all rotation and pumping rates of the time series (conditions I–IV). The digital sampling rate of the hot-film probes, $f = 150$ Hz, corresponds to a spatial scale of $dx = U/f \simeq 0.1$ cm, which is close to the estimate of η ; our spatial resolution however is limited by the length of the probe’s sensing element at 0.3 cm.

The Rhines length λ_β can also be estimated from the time series by using Eq. 2.29 ($\lambda_\beta = (2U/\beta_R)^{1/2}$). For our data, λ_β is in the range $18 < \lambda_\beta < 40$ cm for the 2D and 3D cases respectively.

The PDFs of the velocity differences $\delta v(\ell)$ for several separations (ℓ) at low and high rotation rates are shown in Fig. 4.17. Observe that the low-rotation (3D) PDFs shift from exponentials (in the tails) at small separations to a Gaussian shape at large separations, as expected for 3D turbulence. The high-rotation (2D) PDFs on the other hand preserve their shape over a wide range of separations, indicating a self-similar flow. The 2D PDFs show a large departure from Gaussianity at all scales, consistent with numerical simulations by She *et al.*[79] and by Farge *et al.*[28] which have found coherent structures to cause deviation from Gaussianity.

The self-similarity might be due to the ejections existing at all the scales in the inertial range, or alternatively to an inverse cascade which preserves the coherence of vortices as they merge and grow. In the 3D case, the scale dependence of the PDFs is like that of other 3D experiments, indicating that the coherent structures only exist at small scales of the inertial range. This can be due to small-scale ejections, or to a forward energy cascade responsible for the self-organization of the flow into vortices, as in other 3D flows.

The structure function exponents are obtained by the method of Extended Self Similarity (ESS). This technique, introduced by Benzi *et al.* [9], has become the standard way to extract scaling exponents from flows where the scaling range is limited. It works by plotting S_p vs S_3 on log-log axes and fitting a line through them, the idea being that S_3 scales linearly with ℓ for a Kolmogorov-type flow (Kolmogorov's four-fifths law). Since systematic errors (or trends) should be present in S_3 as well as other order structure functions, the technique provides a more robust scaling region than the standard way of plotting S_p vs. ℓ . In the framework of ESS, a self-similar flow would produce scaling exponents $\zeta_p = p/3$, because the different S_p

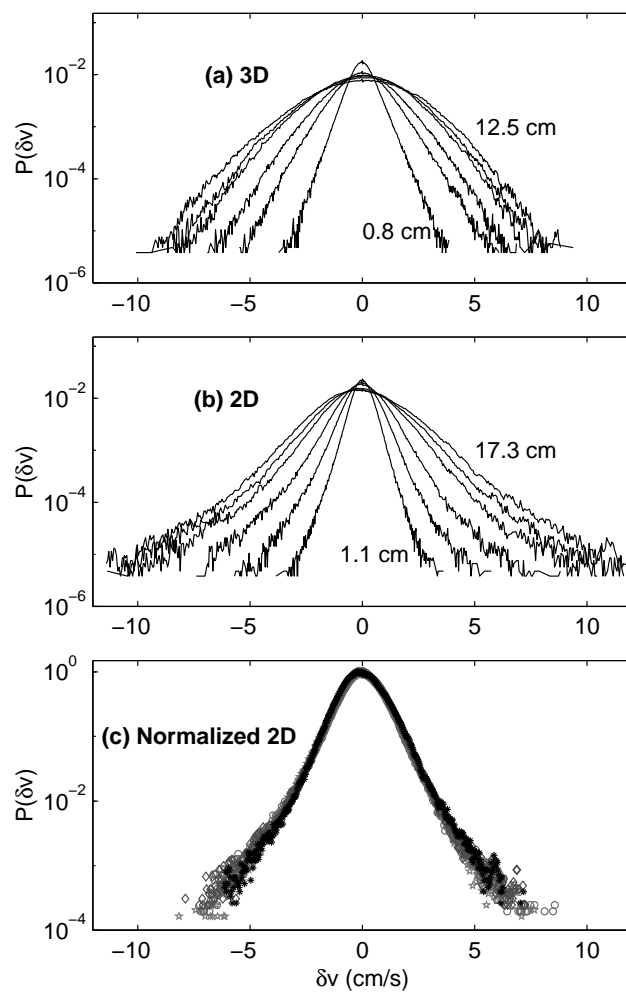


Figure 4.17: Velocity difference histograms for (a) 1.57 rad/s, 450 cm³/s ($\ell = 0.8, 2.4, 3.9, 7.0, 8.5$ and 12.5 cm) and (b) 11.0 rad/s, 150 cm³/s ($\ell = 1.1, 2.3, 4.6, 9.2, 12.7$ and 17.3 cm). Part (c) shows the same curves as part (b) re-scaled by their standard deviation (x -axis) and by their maximum (y -axis).

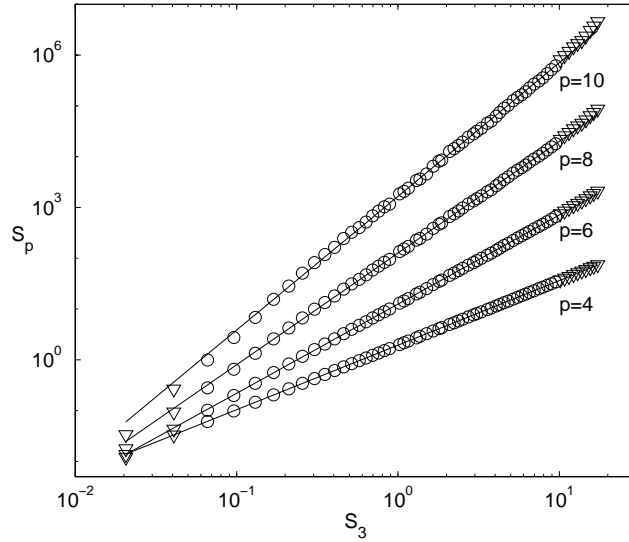


Figure 4.18: Linear fits to $\log(S_p)$ vs. $\log(S_3)$ (Case IV, 3D flow) in the inertial range (o). The smallest scale is approximately 0.5 cm, and the largest scale is about 15 cm. The ∇ show deviations from the scaling outside the inertial range.

are compared to S_3 . However, in general one could plot S_p vs. any order structure function, and the slopes would change accordingly.

A representative plot of S_p vs. S_3 for the 3D flow is shown in Fig. 4.18, where we observe a sizeable scaling region. The fits are typically quite good for both the 2D and 3D cases in the range $0.5 < \lambda < 15$ cm for the 2D and 3D flows. This region is bounded by η and λ_β but never quite reaches either. However, the curvature of our tank distorts structures much larger than 15 cm, so it is not surprising that we see deviations in the linear fit at those scales. At the small scales end, the dissipation is predicted to start affecting the flows at scales a few times η , so the deviations might be due to the dissipation effects; we might also be running into the resolution of the HF probe. Note that the alternative definition $S_p = \langle |\delta v|^p \rangle$ is used here, since S_3 changes sign in the case of the 2D flows (see next chapter).

Finally, the structure function exponents, ζ_p for $p \leq 10$ are shown in Fig. 4.19

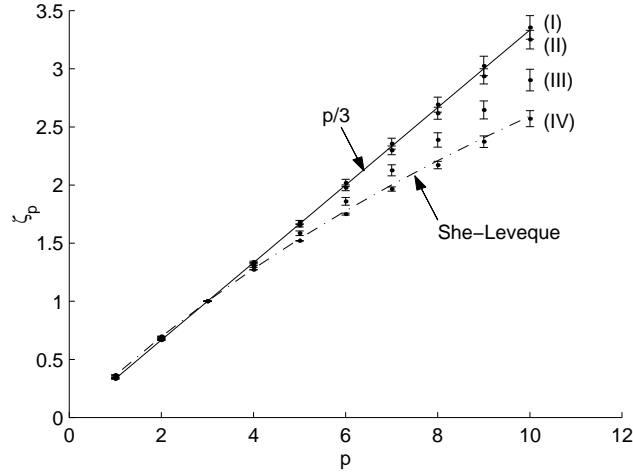


Figure 4.19: Structure function exponents for the different data sets, from the most 2D case (I) to the most 3D (IV) (see table 4.3)

for four Rossby numbers. The scaling for the most 2D flow falls on the $p/3$ line. For lower rotation rates a gradual departure from the self similar linear scaling develops, until the most 3D flow falls on the log-poisson curve, matching data from 3D turbulence experiments and simulations.[3, 13] This suggests that structure function exponents are a reliable measure of the extent to which our flow is 2D or 3D. The values of ζ_p for the different conditions of our flow are given in Table 4.4, along with values for Couette-Taylor flow, another flow with strong rotation. Also included are the values from the atmospheric boundary layer at $Re_\lambda \simeq 10,000$ [92], for comparison.

The points plotted in Fig. 4.19 are the average values for the two probes over all realizations at the same conditions. The error bars correspond to the standard deviation from the different experimental runs. In order to test the convergence of our fits, the data were divided into sets of shorter time series and the structure function routines were run on those subsets. For time series longer than $N = 2.50 \times 10^5$ points, the spread in the calculated exponents (ζ_{10} in particular) with record length was comparable to the spread from separate runs, the latter being due to system-

atic errors during a given run. It was therefore more advantageous to take several independent realizations of the same flow rather than longer time records.

Table 4.4: Values of ζ_p for different Rossby numbers, compared with values from other experiments.

Current experiments				
p	$Ro = 0.11$	0.14	0.32	0.62
4	1.34 ± 0.0065	1.33 ± 0.0053	1.30 ± 0.0084	1.27 ± 0.0016
6	2.02 ± 0.031	2.00 ± 0.025	1.86 ± 0.033	1.75 ± 0.0086
8	2.69 ± 0.065	2.62 ± 0.051	2.40 ± 0.062	2.17 ± 0.032
10	3.36 ± 0.10	3.25 ± 0.080	2.90 ± 0.093	2.57 ± 0.070
p	$p/3$	Couette-Taylor [81] $Re_\lambda \simeq 220$	Atmospheric flow [92] $Re_\lambda \simeq 10,000$	She-L�ev�eque [80]
4	1.33	1.27	1.26	1.28
6	2.00	1.71	1.71	1.78
8	2.67	2.08	2.05	2.21
10	3.33	2.40	2.38	2.59

4.6 Hierarchical Symmetry

We have seen that the structure function exponents show a shift from a linear scaling with order p at high rotation rate to the typical 3D behavior for the low rotation rate. This information only shows the departures from self-similarity for the 3D case, which has already been studied extensively. To learn more about the internal structure of the flow, we turn to the She-L ev eque [80] model of turbulence. This model assumes an internal organization of the flow, which consists of a hierarchy of structures ranging from strong highly intermittent ones (such as collapsed vortices) to weaker more common events. The model proposes two tests of this internal organization, which allow us to better understand the relationship between the structures of different intensities in our flow. The β - and γ -tests of the Hierarchical Structure model are applied below.

The tests concern the scaling of the hierarchy of functions $F_p(\ell) = S_{p+1}(\ell)/S_p(\ell)$. The F_p function is the mathematical expectation value for a family of weighted probability distribution functions $Q_p(\delta v_\ell) = |\delta v_\ell|^p P(\delta v_\ell) / \langle |\delta v_\ell|^p \rangle$, or the mean fluctuation amplitude with respect to this family of distributions. For higher p , $Q_p(\delta v_\ell)$ is peaked at higher intensity of the fluctuations δv_ℓ . Therefore, these functions describe the intensity of fluctuations in the flow, with higher order F_p describing the more intermittent, larger, fluctuations. The model proposes the scaling

$$F_{p+1}(\ell) = A_p F_p(\ell)^\beta F_\infty(\ell)^{1-\beta} \quad (4.6)$$

where $0 \leq \beta \leq 1$ is a constant, A_p is independent of ℓ , and where

$$F_\infty(\ell) = \lim_{p \rightarrow \infty} \langle |\delta v_\ell|^{p+1} \rangle / \langle |\delta v_\ell|^p \rangle \quad (4.7)$$

characterizes the most intermittent structures.

4.6.1 The β -test

Since in theory one needs to wait an infinite time to measure F_∞ , the difficulty is avoided by considering the ratio:

$$\frac{F_{p+1}(\ell)}{F_2(\ell)} = \frac{A_p}{A_1} \left(\frac{F_p(\ell)}{F_1(\ell)} \right)^\beta \quad (4.8)$$

which can be calculated for all values of p . The β -test consists of checking for this power law scaling. If it exists, then the hierarchical symmetry is verified and the value of the slope (β) in log-log space is a descriptor of the amount of intermittency in the flow. Characteristic curves of the β -test are shown in Fig. 4.20, for a 2D case and a 3D case.

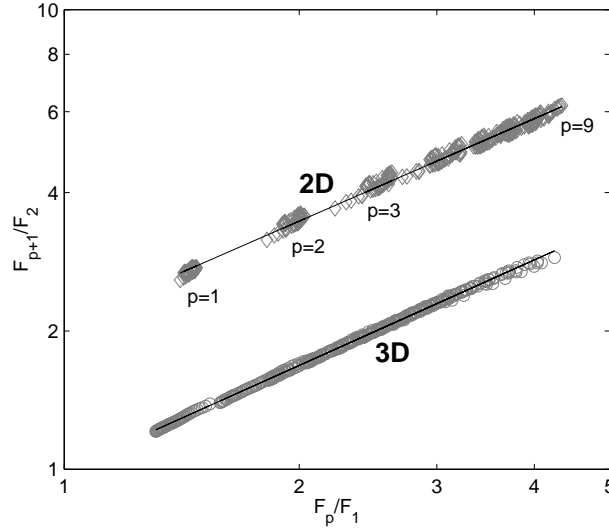


Figure 4.20: Example β -test fits for 3D and 2D cases. The 2D curve is shifted up for clarity. The slopes of these curves are $\beta = 0.74$ ($Ro = 0.11$) and $\beta = 0.76$ ($Ro = 0.62$).

The value of β remained unchanged with $\beta_{\text{I}} = 0.74 \pm 0.02$ and $\beta_{\text{IV}} = 0.76 \pm 0.02$, and with the intermediate values $\beta_{\text{II}} = 0.78 \pm 0.02$ and $\beta_{\text{III}} = 0.72 \pm 0.02$. These are significantly lower than values reported for Couette-Taylor [81] (0.83) and free jets [56] (0.87). A low β is consistent with the fact that the intermittent structures in our flows are very coherent, and that they stand out of the turbulent background, as seen in Fig. 4.7. Since these structures exist for all the cases discussed here, it is not surprising that β should vary little with the conditions of the experiment, and that its value should be small compared to previously reported values [81, 56].

The points for the 2D case are collected in compact groups for each p , as expected for a self-similar flow; if the flow were perfectly self-similar, these compact groups would each collapse to a point since there is no dependence on ℓ by hypothesis. In contrast, the 3D points trace a straight line both in ℓ and p . From the results of Fig. 4.20 and the scaling of the structure function exponents, we conclude that the 2D flow is no less intermittent than the 3D flow (low β_{2D}), but that the rotation

two-dimensionalizes the intermittent structures; these structures themselves become self-similar in the 2D case, producing a flow where vortices of all (inertial range) sizes and strengths are present. This conclusion is consistent with our visual observations of the ejected vortices.

4.6.2 The γ -test

The Hierarchical Structure model further assumes the scaling

$$F_\infty \sim S_3^\gamma(\ell), \quad (4.9)$$

where γ describes the relative scaling of the most intermittent structures with respect to the magnitude of more typical events (of the order of $\langle \delta v \rangle$, or $S_3^{1/3}$). Its meaning can be understood by an observation of the series of PDFs in Fig. 4.17 for fluctuations at different scales. The value of γ describes how fast the tail magnitude (characterized by F_∞) changes in response to the width of the PDFs (characterized by $S_3^{1/3}$). When $\gamma = 1/3$, the tail expands in the same way as the width of the PDFs, so that the whole family of PDFs preserve their shape. This is a situation where the fluctuations of all intensities are statistically alike, or the flow is globally self-similar. Another limit is $\gamma = 0$, in which the magnitude of the most intermittent structures is not related to the typical fluctuation magnitude. This is the situation where the coherent intermittent structures are physically decoupled from the disordered fluctuations. An example can be found in the randomly driven Burgers equation where shocks are the most intermittent structures and the only dissipative structures in the limit of vanishing viscosity.

In summary, decreasing γ indicates an increasing distinction of the most intermittent structures with respect to the background flow structures. With the assumption of Eq. (4.9), the relative scaling exponent of the velocity structure functions ζ_p is given by [80]

$$\zeta_p = \gamma p + C(1 - \beta^p), \quad (4.10)$$

where $C = (1 - 3\gamma)/(1 - \beta^3)$. Given the values of β , the validity of the assumption (4.9) can be tested by checking that:

$$\zeta_p - \chi(p; \beta) = \gamma[p - 3\chi(p; \beta)], \quad (4.11)$$

where $\chi(p; \beta) = (1 - \beta^p)/(1 - \beta^3)$.

From Eq. (4.10), it is evident that a self-similar turbulent flow can be reached in two ways: either $\beta \rightarrow 1$ or $\gamma \rightarrow 1/3$. According to the Hierarchical Structure model, β measures how fast the coherence of flow structures is established for fluctuations standing out of the random background field, or how fast the coherence of the most intermittent structures are degraded with decreasing magnitude. When β approaches one, flow structures of all intensities appear alike; this similarity of all intensities implies in general the lack of coherence, or the lack of intermittency. In this scenario, γ can in principle have any value. Such a scenario has not yet been observed.

On the other hand, the relative scaling γ approaching 1/3 is a different scenario to achieve a self-similar flow. Since F_∞ is the magnitude of the most intermittent structures, γ measures how fast its magnitude (e.g. the tail of the PDFs) changes with the typical fluctuation magnitude represented by S_3 (e.g. the width in the bell-like curves in Fig. 4.17). This seems to be the scenario observed here: during the 3D-2D transition, β remained unchanged ($\beta \simeq 0.75$), while γ showed a gradual approach from $\gamma_{3D} = 0.18$ to $\gamma_{2D} = 0.34$ (Fig. 4.21).

The fits for γ are very robust and do not depend strongly on β . The value of γ_{3D} is slightly higher than those reported for Couette-Taylor experiments and free jets (0.10). This is probably due to the effect of rotation, since even in the most 3D

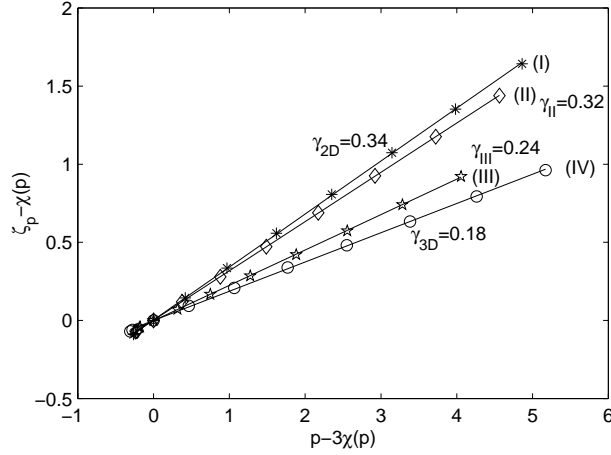


Figure 4.21: γ -test for all hot film data. The numbering is as in Table 4.3. The lines are least-squares fits to the data.

flow the stretching of structures is already slightly inhibited. On the other hand, the value of γ_{2D} gives further indication of a self-similar flow. Therefore, the γ test helps discover a smooth transition in the degree of the synchronization between the high and low intensity fluctuations when the rotation rate increases. A uniform β for flows at all rotations implies that the high intensity fluctuations differ from low intensity fluctuations in the same way in all regimes during the 3D-2D transition.

4.7 Summary and discussion

In this chapter, the 2D and 3D turbulent flows that we obtain in our (non-standard) experiment are described. The first step is to compare the flows visually by using the PIV. We find that for the lowest rotation rate ($\Omega = 0.79$ rad/s), the flow is highly 3D as suggested by the large number of small vortices populating it. This is an indication that the inverse cascade mechanism is very weak. For slightly larger rotation rates, the flow starts to lose its 3D character, presumably because vortex stretching is slowed down. This leads to the existence of a weak inverse cascade,

which becomes increasingly strong as the rotation rate is increased. Finally, in the case of the highest rotation rates, small vortices quickly merge with other structures in the flow and the largest scales grow to fill the tank in the azimuthal direction. The energy of these largest scales can get transferred back to smaller scales through the ejection of smaller vortices which draw energy out of the large ones and back into the flow at a smaller scale. These vortices can either get sheared and dissipate their energy, or they can merge with the large structures again, thus cascading energy back to larger scales.

In the second part of this chapter, the long time series are analyzed using high-order statistics. We search for intermittency in turbulent flows at a fixed Reynolds number ($R_\lambda \simeq 360$) with varying degree of three-dimensionality. As the flow becomes more 2D, it gradually becomes more self-similar. The slopes of the structure functions for the most 2D cases are indistinguishable from the linear scaling $\zeta_p = p/3$. As Ro increases, the slopes approach and eventually match experiments in fully 3D turbulence and the prediction of the She-L  v  que model. However, when we use the β -test, the values of β for the 2D and 3D flows all point to a highly intermittent flow, where the intermittent structures are coherent and stand out of the background. This is consistent with our visual observations of coherent vortices populating the turbulent jet at all rotation rates. These vortices lose their singularity and gain in spatial extent as the flow becomes 2D, probably due to their inability to stretch and collapse into filaments. This is measured by the γ -test, with the value of γ shifting from 0.18, a value comparable to other 3D experiments to $\gamma_{2D} \simeq 0.33$, as predicted for self-similar turbulence.

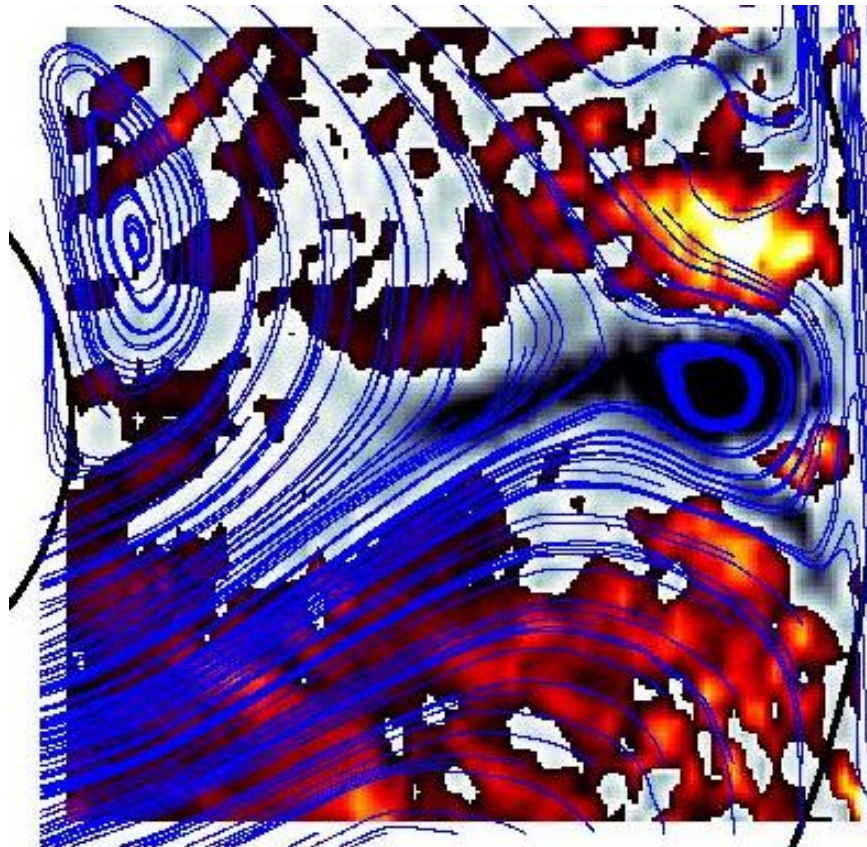
The above results suggest the following physical picture for the rotating turbulence in the annulus: Vortices exist in all turbulent regimes at all scales starting from the injection scale and with all intensities. At low rotation rates (3D regime), large intense vortices break into smaller vortices and a cascade of energy from large

scales to small scales takes place. Consequently, there are less intense vortices at large scales in 3D than in 2D. As the rotation rates is increased, large intense vortices become more stable and the flow becomes self-similar. These results suggest that a distinction should be made between the concepts of “intermittency” and “self-similarity”. Intermittency and strong coherent vortices in the turbulent field can emerge out of non-local dynamics, even in the absence of vortex stretching. However, we have found that the presence of these intermittent structures does not exclude a self-similar cascade in 2D flows, since vortices of all inertial range sizes can exist. The presence of these coherent structures however implies that the statistics of the velocity increments are far from Gaussian, even at large separations. Future studies will test the effect of the beta plane on the dynamics, as well as the validity of the Rossby number in determining the level of two-dimensionality of a rotating turbulent flow.

In the next chapter, we will concentrate on the scaling of the structure functions and the energy spectrum in the 2D case. Those quantities display an anomalous scaling which will be explored and explained.

Chapter 5

Anomalous scaling in 2D flows



The two-dimensionalization of a 3D turbulent flow by rotation is real and can be measured in several ways. In the previous chapter, we saw that we could observe this transition by using high-order statistical tools. In particular, the scaling of the structure functions by using the ESS method showed a clear shift to a self-similar flow as the rotation rate was increased. The transition was also evident in the behavior of the γ -test of the hierarchical structure model. From the visualization, the measured statistical values could be related to actual structures in the flow. The dynamics of the large structures were found to create intermittent bursts which affected the scalings in different ways in the 2D and 3D cases.

In this chapter, we concentrate on the 2D turbulence. The energy spectrum is calculated from the time series, thus allowing us to study statistics in Fourier space. Furthermore, the scaling of the structure functions of the fast-rotation flow are explored as they scale with the separation distance (ℓ), and they are compared with the relative scaling with respect to S_3 . The statistics in both real space and in wavenumber space, consistently with each other, display an anomalous scaling which was not predicted for 2D turbulence.

The hot-film data used in this chapter correspond to a tank rotation rate $\Omega = 11.0$ rad/s, and a pumping rate $Q = 150$ cm³/s (data set I, Talbe 4.3). The corresponding Rossby number is 0.11, and the Reynolds number is 2×10^4 . For these parameters, the flow is highly 2D and sufficiently turbulent to produce an inverse energy cascade. The cascade however is much stronger in the case of higher pumping, and the PIV data are used for the pumping rates $Q = 350$ cm³/s and $Q = 550$ cm³/s.

Representative vorticity fields for the low pumping ($Q = 150$ cm³/s) and high pumping ($Q = 550$ cm³/s) are shown in Fig. 5.1. These flows show the strong coherent vortices ejecting from the inner and outer walls, as well as the large vortices being carried by the mean jet.

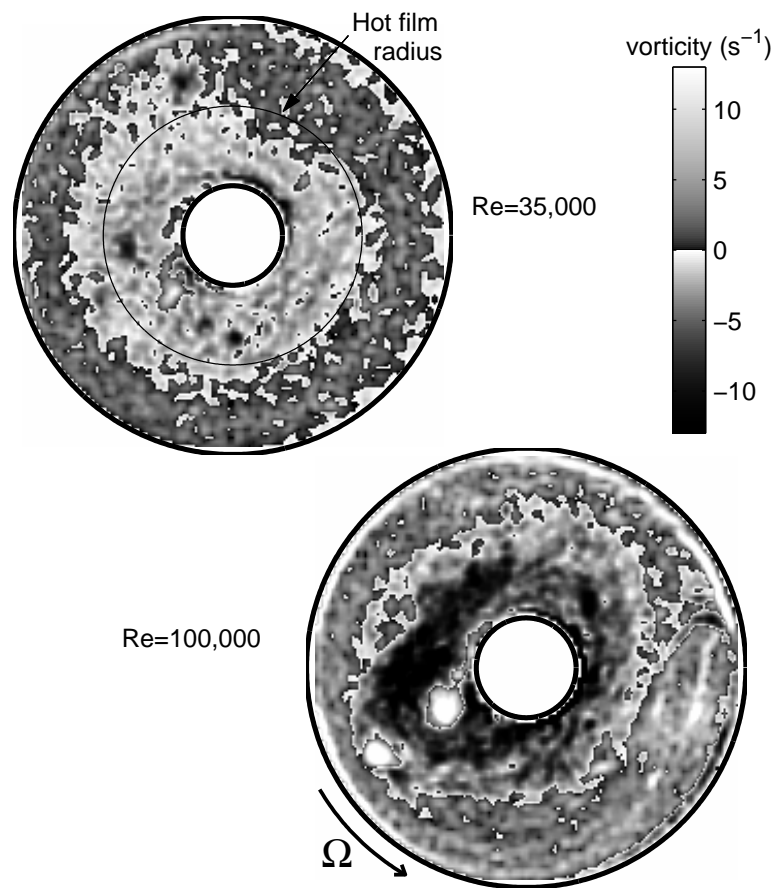


Figure 5.1: Two representative vorticity fields for high rotation rate flows.

5.1 Energy spectrum

We start by computing the energy power spectra from the velocity time series data assuming Taylor’s frozen turbulence hypothesis. Taylor’s hypothesis is applicable because the turbulent intensity (ratio of the rms velocity fluctuation to the mean velocity) is less than 10%. The spectra contain a region with $E(k) \sim k^{-2}$ (Fig. 5.2), in contrast with Kraichnan’s prediction of $E(k) \sim k^{-5/3}$ for the inverse cascade [49]. Energy spectra obtained from PIV measurements of the azimuthal velocity data at $Re = 100,000$ show a scaling consistent with that obtained from the time series data, as shown in the upper curve of Fig. 5.2.

Fits of all of the hot-film spectra in the range $0.1 < k < 1.22 \text{ cm}^{-1}$ give a slope of -2.04 ± 0.06 . At $k \gtrsim 1.22 \text{ cm}^{-1}$, corresponding to $\ell \lesssim 5 \text{ cm}$, the scaling starts to depart from the power law. The spectra from the two simultaneous probes at those scales start to deviate from each other, as shown by the two bottom curves in Fig. 5.2. The two traces are indistinguishable for $k < 1.22 \text{ cm}^{-1}$ but they start to deviate for higher k . The sharp spectral peaks correspond to harmonics of the tank’s rotation rate, not to dynamics of the flow, as discussed in Section 3.1, and shown in Fig. 3.6. These peaks are very localized since the time series are long and the finite-size effects are small.

Two previous (relevant) theoretical approaches had predicted energy spectra of $E(k) \sim k^{-2}$:

The first is a prediction made by Gilbert [36, 35] for the Lundgren spiral vortex model [57]. The Lundgren model assumes a flow made up of individual vortices of different sizes and ages which interact among each other and shed vorticity filaments. The circulation from the vortex core folds the filaments back in the shape of a spiral, a dynamic which has been simulated numerically. Starting with this premise, Lundgren was able to recover the standard $E(k) \sim k^{-5/3}$ in the case where the vortices were allowed to stretch in the axial direction [57]. When stretching

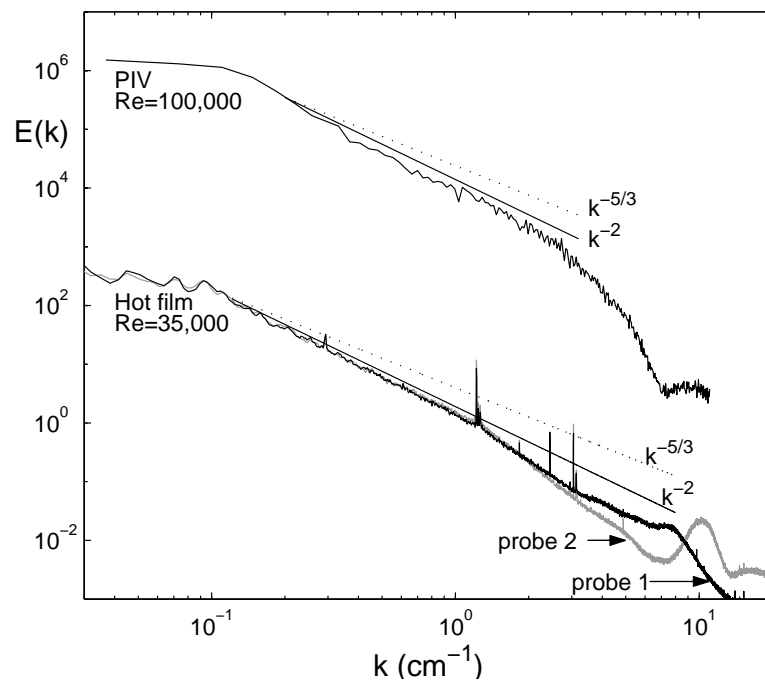


Figure 5.2: Energy spectra (arb. units) with a dotted line showing the Kraichnan $k^{-5/3}$ inverse cascade and a solid line showing k^{-2} behavior.

is removed from the model, the slope of the energy spectrum becomes -2 when averaged over a distance spanning many such vortices [35]. Spirals were found in the flow in our system as suggested by Fig. 5.3 (see also Chapter 4), so it is interesting that our energy spectrum should match the predictions for the spiral vortex model. However, Gilbert also reported discontinuities in the energy spectrum $E(k)$ [36], which we do not observe in our data.

The second context in which this scaling of the energy spectrum was predicted is for the case of rotating turbulent flows. The prediction was made by Zhou [105] in 1995, followed by Canuto and Dubovikov [18] in 1996. The two groups use similar approaches which might or might not be equivalent¹. These authors do not explicitly address the two-dimensionalization of the flow. Zhou’s prediction is “phenomenological”, and is based on estimates of the time scales of the nonlinear interactions with the time scale associated with the rotation. He does not indicate whether the slope of the energy spectrum is for an inverse or a forward cascade. On the other hand, Canuto and Dubovikov only discuss a forward cascade. In their analysis, the forward cascade of energy is “inhibited” by the rotation, thus causing the slope to become steeper. We shall see below that the energy in our system is cascading inversely, so it is improbable that the models quoted here are applicable.

At high wavenumbers, our power spectra are consistent with those previously found for the forward (enstrophy) cascade in 2D turbulence, $E(k) \sim k^{-n}$, where $3 \leq n \leq 4$. However, our spectral range is too small to deduce a value for n .

5.2 Probability distribution functions

By plotting the PDF for the velocity differences $P[\delta v(\ell)]$ (Fig. 5.4), we obtain a good indication of self-similarity: We normalize the velocity differences by their

¹There have been several comments and answers by the above authors about the similarity and differences of their approaches [106, 19].

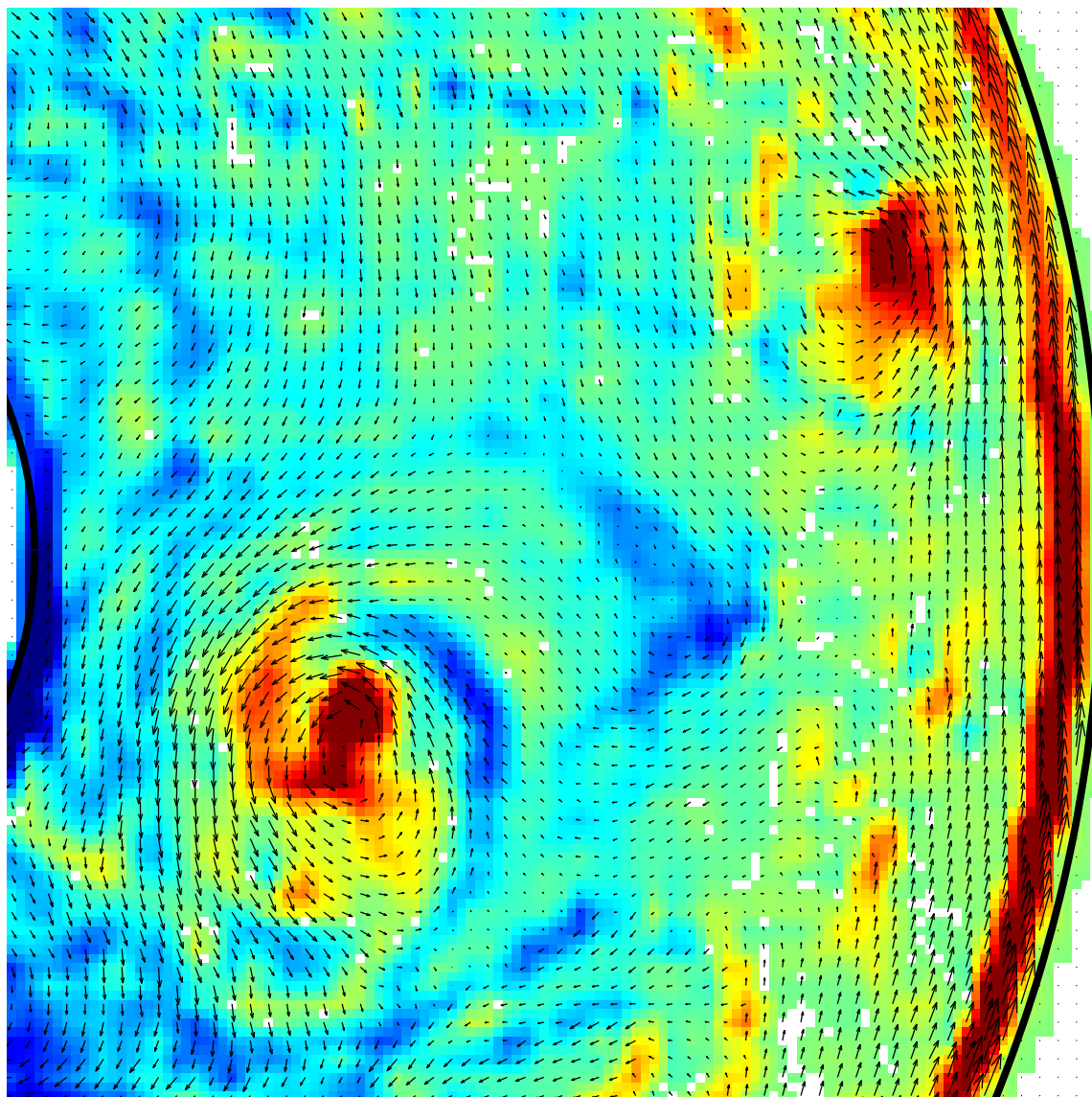


Figure 5.3: Ejecting vortex showing spiral structure ($\Omega = 11.0$ rad/s, $Q = 350$ cm³/s). Such vortices often occur in our flows.

standard deviation $(\delta v)_{\text{rms}}$ and the probability by its maximum value, P_{max} . By plotting P/P_{max} vs. $\delta v/(\delta v)_{\text{rms}}$, we observe a very good collapse of the PDFs onto a single curve, indicating a flow where the statistics are independent of the scale at which they are measured.

The curve that is traced by the PDFs is far from Gaussian; the enhanced probability in the tails is likely due to the strong velocity differences that arise as coherent vortices pass the probes, as discussed in the previous chapter. However, the collapse onto a single curve is quite good for all experimental runs, for both the energy and enstrophy cascade ranges (i.e. both $\ell > 2$ cm and $\ell < 2$ cm). This is in stark contrast with all previously observed flows where the statistics at large separations are Gaussian, indicating a lack of correlation of the statistics at large scales. In the case of other self-similar flows [69, 12], the PDFs were nearly Gaussian at all scales. In the case of 3D intermittent turbulence, the statistics shifted from exponentials to Gaussian with increasing ℓ , as is the case for the 3D flow in the previous chapter.

From the normalization of the PDFs, we get a second indication of anomalous behavior: The value of the standard deviation of the velocity differences, δv_{rms} scales as $\delta v_{\text{rms}}(\ell) \sim \ell^{1/2}$ (see insets of Fig. 5.4). This is consistent with the scaling of the energy spectrum in the inverse cascade range (Fig. 5.2), but departs from the expected value from Kolmogorov's 1941 theory. The four-fifths law of K41 predicts the scaling $S_3 = \langle \delta v \rangle^3 \sim \ell$, therefore $\langle \delta v \rangle = S_3^{1/3}$ should scale as $\ell^{1/3}$, as opposed to the $\ell^{1/2}$ that we observe.

5.3 Structure functions

Self-similarity was already discussed in the previous chapter through the use of the structure function scaling. By using Extended Self Similarity (ESS), the relative exponents of the structure functions were found to fall on the $\zeta_p = p/3$ line.

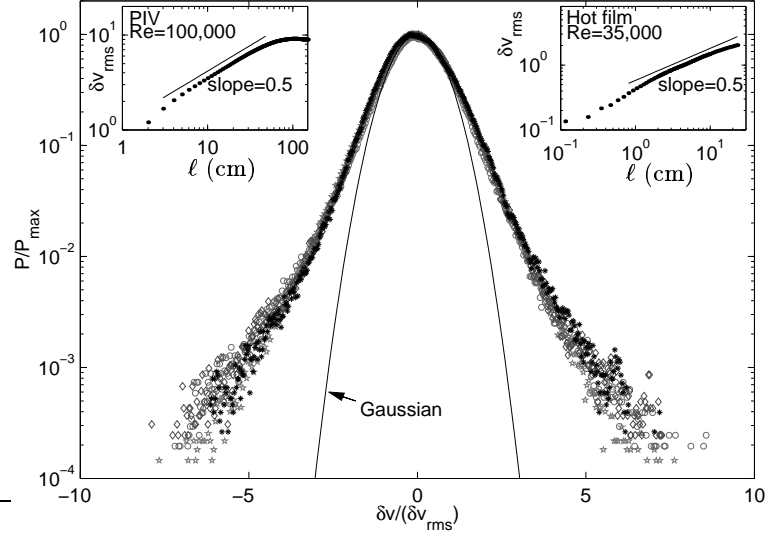


Figure 5.4: Normalized probability distribution function for the velocity differences ($\ell = 0.6, 4.6, 9.2, 17.3$ cm). The standard deviation of the velocity differences (see insets) scales as ℓ^α where $\alpha = 0.50 \pm 0.06$ for $Re = 35,000$ and $\alpha = 0.54 \pm 0.06$ for $Re = 100,000$.

Here, we look more carefully at the scaling of these structure functions S_p , both as a function of ℓ [as shown in Fig. 5.5(a)] and as a function of S_3 (ESS) [Fig. 5.5(b)].

There is a scaling region in Fig. 5.5(a) (labeled A) from about 2 cm to 8 cm, and some indication of another scaling region (labeled B) for $\ell < 2$ cm; the transition between the two regions can be seen more clearly in the plot of $S_{10}/\ell^{5.5}$ vs. ℓ in the inset. The 2 cm lower limit of scaling of the structure functions is below the 5 cm ($k = 1.2 \text{ cm}^{-1}$ in Fig. 5.2) length where the energy spectrum behavior changes; this difference might be due to systematic error in calibration of the probes (note in Fig. 5.2 the difference in two probes at high wavenumbers), or perhaps because the scaling regions in real space and in Fourier space do not exactly correspond, as discussed for example by Frisch [33] (p. 62).

The ESS plots of our data, Fig. 5.5(b), exhibit power law scaling through both ranges A and B, for lengths $0.5 < \ell < 15$ cm. Since S_3 should contain the

same trends as the other structure functions, it is not surprising that the switching from region A to B is lost by this method.

One test for the existence of an inverse energy cascade in 2D turbulence is the sign of $S_3(\ell)$: The energy transfer for anisotropic flows can be written as $\langle \varepsilon \rangle = -\frac{1}{4} \nabla_\ell \cdot \langle |\delta \mathbf{v}(\ell)|^2 \delta \mathbf{v}(\ell) \rangle$, where \mathbf{v} is the full 3D velocity vector and $\langle \varepsilon \rangle$ is the mean rate of energy transfer (Frisch [33], p. 88). For the 3D forward cascade, $\langle \varepsilon \rangle$ is positive; a negative value of $\langle \varepsilon \rangle$ corresponds to an inverse cascade. If the anisotropy is not too strong, the longitudinal S_3 dominates the transverse S_3 , and one can obtain the sign of $\langle \varepsilon \rangle$ from measurements of the longitudinal structure function alone. The hot-film data yield $S_3 > 0$ for $\ell < 10$ cm, which suggests that the inverse energy cascade stops at that point. This length corresponds visually to the scale of the largest vortices for these flow conditions; thus region A corresponds to the inverse cascade. Scales below about 1 cm (the distance between the holes in the inner ring) presumably correspond to the forward enstrophy cascade.

To verify the relationship between the inverse cascade and the value of S_3 , we use the PIV data to compute $S_3(\ell)$ for different pumping rates, plotted (on linear axes) in Fig. 5.6. In the case of $Q = 150 \text{ cm}^3/\text{s}$, the value of S_3 is very small even in the HF data, and it is below the resolution of the PIV. However, note that Fig. 5.6 shows a qualitative difference in the behavior of S_3 around $\ell \simeq 15$ cm, which is consistent with the hot-film measurements. For higher pumping rates, the signal to noise ratio of the PIV improves dramatically, and we see that S_3 is positive for larger ℓ as the pumping rate is increased. This indicates that enough energy is injected into the system at the higher pumping rates to allow for an inverse cascade which goes to larger scales. This idea is consistent with the visual observations of larger vortices present at the higher pumping rates.

The exponent values ζ_p deduced from the plot of $S_p(\ell)$ [region A in Fig. 5.5(a)] and from the ESS plot [Fig. 5.5(b)] are compared in Fig. 5.7 (and Table 5.1) with the

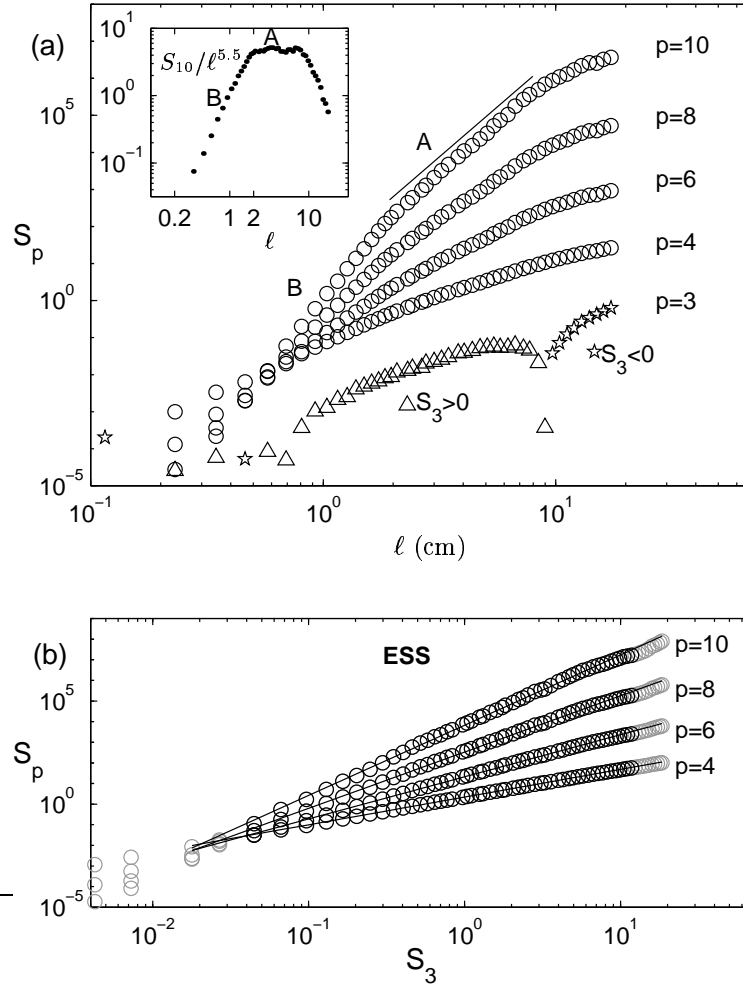


Figure 5.5: Even order structure functions (a) as a function of ℓ and (b) as a function of S_3 (an Extended Self Similarity plot), for the hot-film data at $Re = 20,000$. The graph of $S_{10}/\ell^{5.5}$ in the inset in (a) emphasizes the sharpness of the bend in S_{10} at $\ell \simeq 2$ cm. In (b) the dark symbols indicate the region from which the values of ζ_p were extracted.

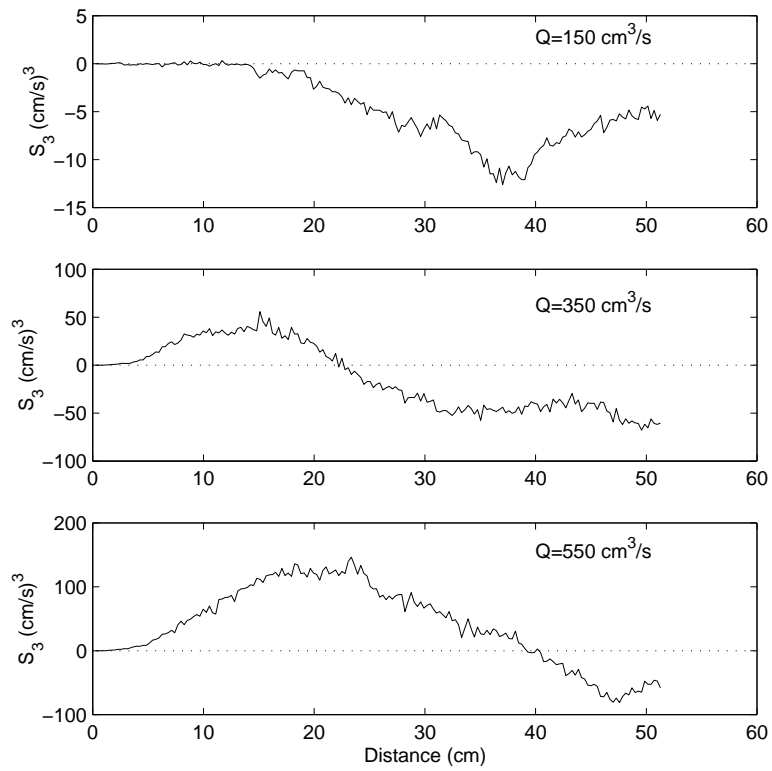


Figure 5.6: S_3 vs. ℓ for three pumping rates (linear axes), using PIV data.

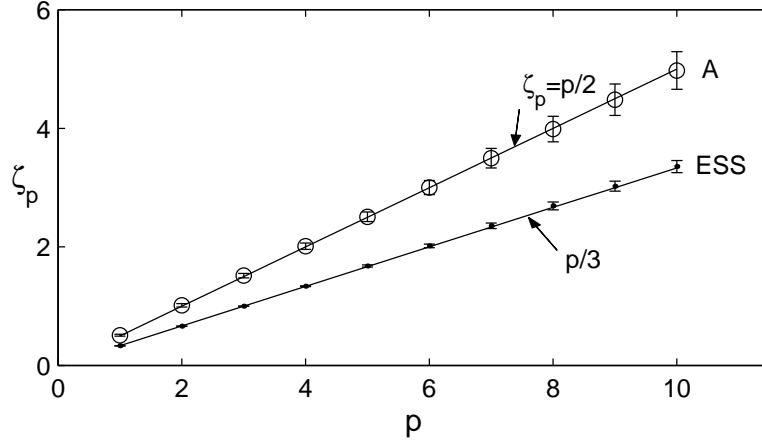


Figure 5.7: Scaling exponents ζ_p as a function of p for region A of Fig. 5.5(a), and from the Extended Self Similarity analysis, Fig. 5.5(b). Region A, the inverse energy cascade region, yields $\zeta_p = (0.50 \pm 0.03)p$, while the ESS scaling shows the expected $\zeta_p = (0.33 \pm 0.01)p$ scaling over the forward and inverse cascade ranges. The error bars show the standard deviation of the eight separate data sets of 10^6 points.

prediction $\zeta_p = p/3$. Region A of Fig. 5.5(a) yields a scaling $\zeta_{p,A} = p/2$, in contrast with theory, although $\zeta_{p,ESS} = p/3$, as it must for a self-similar flow. The error bars correspond to the standard deviation of the spread from the different experimental runs (eight runs in this case).

Table 5.1: Values of ζ_p plotted in Fig. 5.7.

p	ESS	S_p vs. ℓ (region A)
4	1.34 ± 0.0065	2.01 ± 0.054
6	2.02 ± 0.031	3.00 ± 0.12
8	2.69 ± 0.065	3.99 ± 0.21
10	3.36 ± 0.10	4.97 ± 0.32

5.4 Summary

In this chapter, we combine real space and wavenumber space analysis of the 2D flow. In doing so, we find a scaling of the energy spectrum that scales as $E(k) \sim k^{-2}$, instead of Kraichnan's prediction of $k^{-5/3}$. This scaling is further supported by behavior of the structure functions which display a region, corresponding to the inverse cascade, where $S_p \sim \zeta_p$ and $\zeta_p = p/2$. This scaling of the structure functions is unexpected, but it is consistent with the predictions of $E(k) \sim k^{-2}$ for the energy spectrum, made by Gilbert [35], and also by Zhou [105] and Canuto and Dubovikov [18]. Another fact which had not been expected in the turbulence literature is that the scaling of S_p vs. ℓ might give a remarkably different value from the ESS scaling S_p vs. S_3 .

The $p/2$ scaling obtained for ζ_p in our flow may be a consequence of an inverse cascade driven by a radial velocity shear. We have seen that the background shear in the flow can force the vortices to eject radially across the jet. Since the radial velocity could be independent of the azimuthal velocity, this process would yield an energy flux $\langle \varepsilon \rangle \sim \delta v_s (\delta v_{\parallel})^2 / \ell$, where v_s would be a radial velocity due to the interaction of the vortices with the mean shear, v_{\parallel} the azimuthal velocity and ℓ the azimuthal separation. For a scale-invariant $\langle \varepsilon \rangle$, the resulting p^{th} order velocity structure function would have the scaling exponent $p/2$.

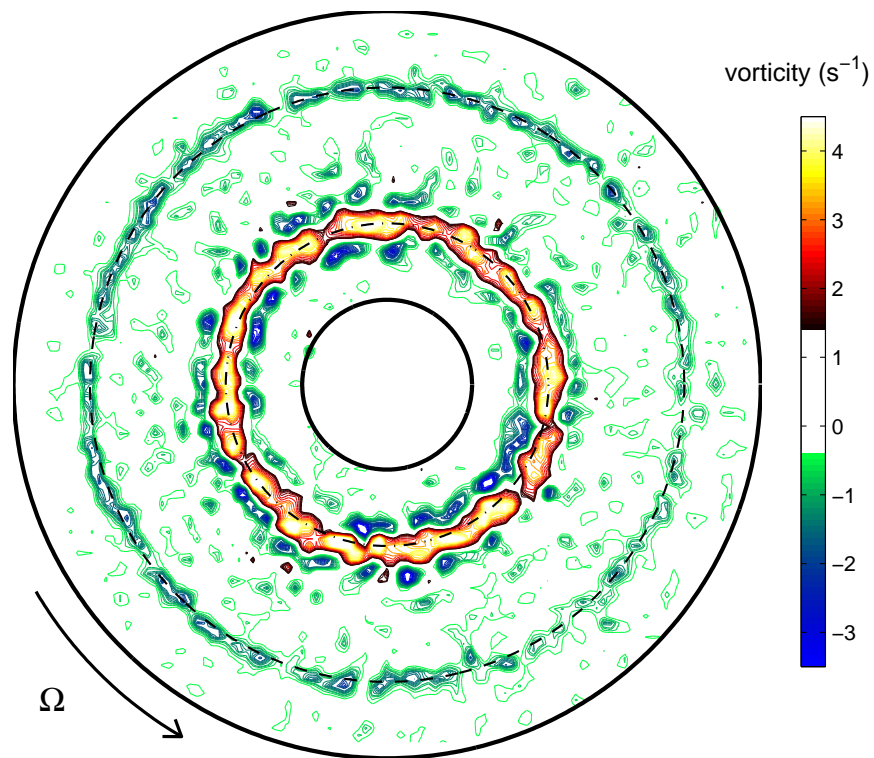
This result is significant in two ways. First it underscores the fact, stated in Chapter 2, that rotating turbulence is a different flow from the limit of two-dimensional Navier-Stokes. The disagreement with Kraichnan's theory is a sign that the limit of quasi-2D turbulence is not a universal one encompassing all flows, but might well be system dependent. Not only is our scaling significantly different from the ones observed by Paret and Tabeling (see figures in Chapter 2), the vortex dynamics are also different. We see vortices merging and growing in size, whereas Paret and Tabeling [70], supported by the numerical simulations of Boffetta *et al.* [12]

observe vortices orbiting each other and forming clusters.

The second area of significance is in the context of shear flows. A particularly interesting trend in turbulence research recently has been to look at scaling in more realistic flows than homogeneous isotropic turbulence. Structure functions have been measured in flows with high shear such as boundary layers, and the scaling of the structure functions is found to depart from the standard 3D scaling. These results are best summarized by Toschi *et al.* [94], who note that the effect of shear seems to be universal across very different systems; the departure from the $p/3$ scaling is significantly more pronounced than in the more homogeneous isotropic cases. The new exponents that have been measured in different experiments and simulations seem to match each other quite well, although the details of the systems are different. In our case, we also study a flow with a strong shear, but where the rotation forces the statistics to remain self-similar. The scaling of ζ_p with p remains linear due to the 2D nature of the flow, but the slope of the scaling changes in an unexpected way. This indicates that the shear can play a very significant role even in self-similar flows. The energy transfer in rotating flows might therefore scale differently from what was previously predicted, and the “classical” expectations might not apply.

Chapter 6

Nonequilibrium statistical mechanics



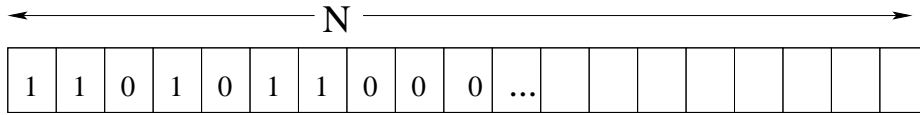


Figure 6.1: 1D vector of binary values has 2^N possible combinations.

As discussed in previous chapters, the statistical approach has dominated turbulence research since Kolmogorov. For this reason, it seems natural to look at the methods of statistical physics and to use the techniques developed there in exploring turbulence. However, turbulence is a nonequilibrium problem, or a system constantly driven far away from thermodynamic equilibrium, making the application of typical statistical mechanics tools (energy, entropy, etc...) complicated. In the last decade, significant advances have been made to generalize the concepts of statistical mechanics to encompass a much larger set of problems, of which turbulence is one. Below we explore this avenue.

In statistical mechanics, one quantity of particular interest is the entropy. A closed system's entropy (σ) is defined as the natural log of the number of states that are possible [48]. For example, consider the 1-dimensional binary vector of Fig. 6.1, in which every box can have the value 1 or 0, giving a total number of combinations of $g = 2^N$. Therefore, the “entropy” of the 1D vector is

$$\sigma \equiv \ln(g(N)). \tag{6.1}$$

Usually, not all the states of a physical system are accessible, due to the limited amount of energy (U) available. Therefore, g and σ depend not only on the number of states, but also on the energy of the system. The entropy then becomes the log of all the *accessible* states, given the available energy. With many possible states to choose from, a physical system will settle in the state that maximizes its entropy in the long time limit. Therefore writing the entropy in functional form can

be very useful, since we can extremize it and predict the final state of the system. Related to entropy and energy is the temperature of the system, which is defined as $1/T = \partial\sigma/\partial U$ (to within a multiplicative constant).

The situation for nonequilibrium systems is complicated by the fact that one often cannot write down a formula for entropy, due to the ability of the temperature and energy dissipation rates to fluctuate in time [7]. A system developed by Tsallis extends the ideas of statistical mechanics to the nonequilibrium realm by introducing a nonextensive entropy [99]:

Given probability p_i for a given state i , the Tsallis entropy is defined as

$$S_q = \frac{1}{q-1} \left(1 - \sum_i p_i^q \right), \quad (6.2)$$

which reduces to the standard (Boltzmann-Gibbs) entropy, $\sigma = -\sum p_i \ln p_i$ in the notation of Eq. (6.2), for $q \rightarrow 1$. The parameter q is called the *nonextensivity* parameter. The Tsallis entropy is in general nonextensive, meaning that if $S_q(A)$ and $S_q(B)$ are the entropies of two probabilistically independent systems, then $S_q(A+B) = S_q(A) + S_q(B) + (1-q)S_q(A)S_q(B)$ [63]. Hence, $q = 1, > 1$ and < 1 correspond to the “extensive, subextensive, and superextensive systems respectively” [63], and in general the entropies cannot be added for separate subsystems.

Tsallis entropies have been used to describe many nonequilibrium systems, as compiled in Ref. [98]. However, the vast majority of the (hundreds of) works cited are theoretical, and very few measurements have been made in experiments to test the validity of this description. Turbulence offers a natural application to this theory, as seen below.

6.1 Application to turbulent flows

The aim of this work is to state the statistical results of the velocity differences in terms of statistical mechanics quantities, in the hope of developing predictive tools for turbulence. By starting with the definition of nonequilibrium entropy of Eq. (6.2), one can extremize (maximize) S_q to find the final state of the system. Two constraints need to be satisfied; they are the norm constraint, which insures that the probabilities add to one, and the energy constraint [7].

Two separate approaches to the application of Tsallis entropy to turbulence have been suggested. Arimitsu and Arimitsu (see e.g. [2]) attempt mainly to recover the structure function exponents as a function of the parameter q . They obtained a relation for q as a function of the intermittency parameter μ , where $\mu = 2 - \zeta_6$, where q can be computed as

$$q = 1 - \frac{1 + \mu + (\log_2(1 + \sqrt{1 - 2^{-\mu}}))(\log_2(1 - \sqrt{1 - 2^{-\mu}}))}{\log_2(1 + \sqrt{1 - 2^{-\mu}}) - \log_2(1 - \sqrt{1 - 2^{-\mu}})}. \quad (6.3)$$

The authors compute a value of $q = 0.237$ by using the value of $\mu = 0.235$ [2]. From this value of q , they are able to calculate scaling exponents ζ_p which are in agreement with the ones observed in experiments and simulations. However, the formula above cannot be implemented for our data. In the case of a Kolmogorov-type self-similar flow, $\mu = 0$ and the Eq. (6.3) gives $q \rightarrow -\infty$. In the case of our 2D flow, characterized by the values plotted in Fig. 5.7, we would have $\mu = -1$ which would lead to $q = 1 + 0.68i$, a complex number. Therefore the formalism of Arimitsu and Arimitsu is not applicable to our data, and we will not pursue this line further.

Beck [7], on the other hand, concentrates on the form of the velocity difference PDFs. As seen in chapter 2, the statistics of the velocity differences in turbulence contain all the statistical information about the flow, so knowing their probability distribution can be a useful measure of the flow.

Beck *et al.* derived a functional form for the velocity difference PDFs [8], and the equations are the following:

$$p(\delta v) = \frac{1}{Z_q} [1 + \beta(q-1)\epsilon(\delta v)]^{-1/(q-1)}, \quad (6.4)$$

$$\epsilon(\delta v) = \frac{1}{2}\delta v^2 - c\sqrt{\gamma\tau}(\delta v - \frac{1}{3}\delta v^3) + O(\gamma\tau), \quad (6.5)$$

$$\beta = \frac{2}{5 - 3q}. \quad (6.6)$$

Here, $p(\delta v(\ell))$ is the probability of finding a given velocity difference δv at scale ℓ . ϵ is an energy associated with the velocity difference δv , which depends on the velocity difference squared plus a small term which depends on the skewness of the statistics through c , γ , and τ . β describes the temperature in the nonequilibrium sense (where $\beta = 1/k_b T$ for an equilibrium system). Z_q is the partition function; it can be thought of simply as a scaling constant [8]. The nonextensivity parameter q is the only fitting parameter, and knowing it will define the functional form of the PDFs completely, as well as defining the entropy S_q .

Note that the experimental PDFs need to be normalized both in the abscissa and in the ordinate (by their standard deviation), since the formulae above do not contain information about the actual velocity differences, but only about the shape of the function. Therefore some information is lost in the process of fitting the statistics in this way.

Beck *et al.* [8] generalize Eq. (6.5) for ϵ by the introduction of a new variable α into the equation for energy,

$$\epsilon(\delta v) = \frac{1}{2}|\delta v|^{2\alpha} - c\sqrt{\gamma\tau}(|\delta v|^\alpha - \frac{1}{3}|\delta v|^{3\alpha}). \quad (6.7)$$

They apply this formulation to time series data from a turbulent Couette-Taylor flow. For $\alpha = 1$, Eq. (6.5) is recovered, and the PDFs of the velocity differences were fit with some accuracy. However, taking $\alpha = 1 - (q - 1) = 2 - q$ yielded very good fits of both the peaks and the tails of the experimental PDFs. The authors relate α to the intermittency parameter of the log-normal theory [33], $\mu = 2 - \zeta_6$, such that a smaller α (larger q) corresponds to more intermittent flow.

6.2 Results

In this chapter, we apply the ideas developed above to our flow statistics to explore whether the signature of a 3D-2D transition is visible in the Beck-Tsallis analysis. We concentrate on the most 2D and most 3D flows for which time-series data is available, namely flows I ($\Omega = 11$ rad/s, $Q = 150$ cm³/s) and IV ($\Omega = 1.57$ rad/s, $Q = 450$ cm³/s) in Table 4.3 above. We start with Eqs. (6.4), (6.6), and (6.7) above, to obtain the values of q which best fit the velocity difference PDFs. A few changes were done to the equations above, as described next.

6.2.1 Fitting parameters

Beck *et al.* make certain assumptions about the dependence of the different parameters on q [8]. For instance, we have seen above that the form for $\alpha(q)$ is empirically chosen. If we use $\alpha = 2 - q$ as in Ref. [8], we obtain fits which are reasonable, but not quite satisfactory. Instead, we try to use

$$\alpha = 1 - (q - 1)^\kappa \tag{6.8}$$

where κ is a positive integer. This form was tested for different values of κ , and the results are shown in Figs. 6.2 and 6.3. In these figures, the top plots show the value of q (for different separation distance, ℓ) as the power (κ) is varied from 1 to

10. The computed value of q shows a strong dependence on κ for small κ , but then becomes almost fixed as κ grows.

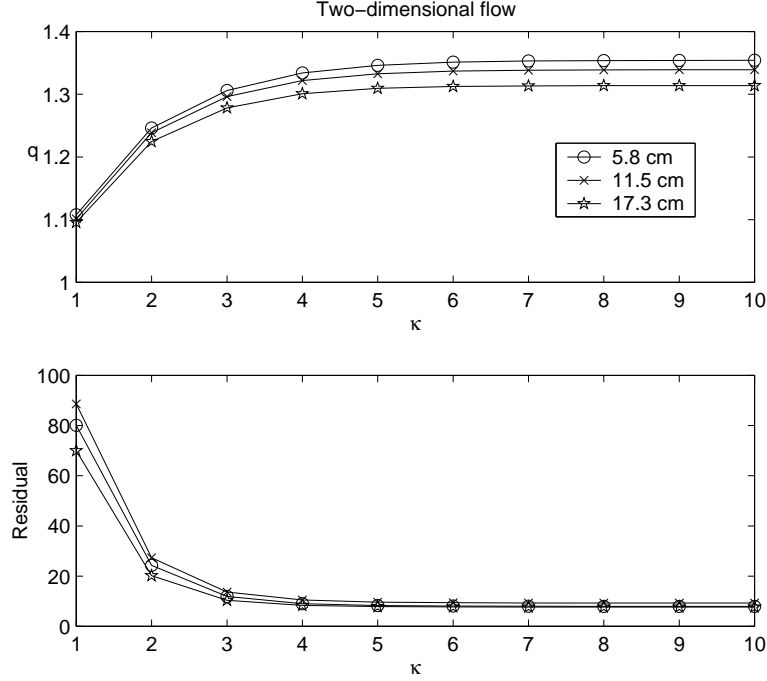


Figure 6.2: Suitability of the fits with κ in the 2D case. The top figure shows the value of q , while the bottom figure shows the residual norm.

The bottom plots show the error in the fits, through the norm of the residual, or the sum of the squared error. The reduction in the residual shows that the fits are improved with higher κ , especially in the case of the 2D flows. In the case of the 3D flows, the residuals are relatively fixed for $\kappa > 2$, consistent with the fixed value of q . In the fits below, we will use $\kappa = 7$ for all the data.

Note however that the residual for the 3D flows at large separation is large, indicating poor fits. At these conditions, the fits can be vastly improved by changing the dependence on the skewness in Eq. (6.5) above. The skewness is defined as

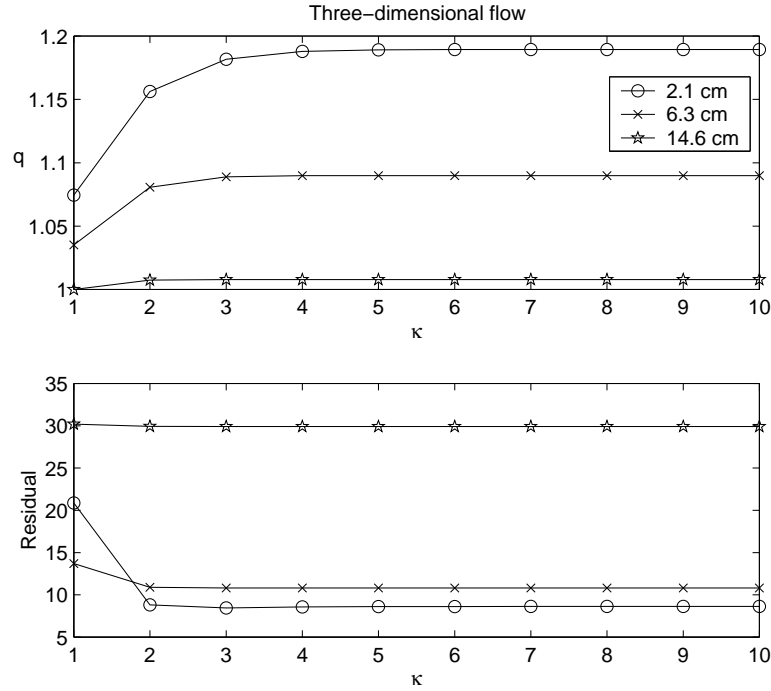


Figure 6.3: Same as Fig. 6.2, for the 3D case.

$$\xi = \frac{S_3}{S_2^{3/2}}. \quad (6.9)$$

In “typical” 3D flows, it is always small and negative, since S_3 does not change sign and $S_2 \geq 0$ by definition. Beck *et al.* make this argument to use $c\sqrt{\gamma\tau} \simeq 0.124(q-1)$ in their fits of experimental Couette-Taylor data [8]. Since S_3 changes sign in 2D flows (see chapter 5), it is no surprise that the results should take the skewness into account.

In our experiments, the skewness changes sign for both the 2D and 3D flows, as shown in Fig. 6.4. This is probably due to the anisotropy or inhomogeneity of the flow. Furthermore, the values of ξ , while small, do not seem to converge to an asymptotic value for large separations. For these reasons, we find that a fixed form for $c\sqrt{\gamma\tau}$ does not produce very good results.

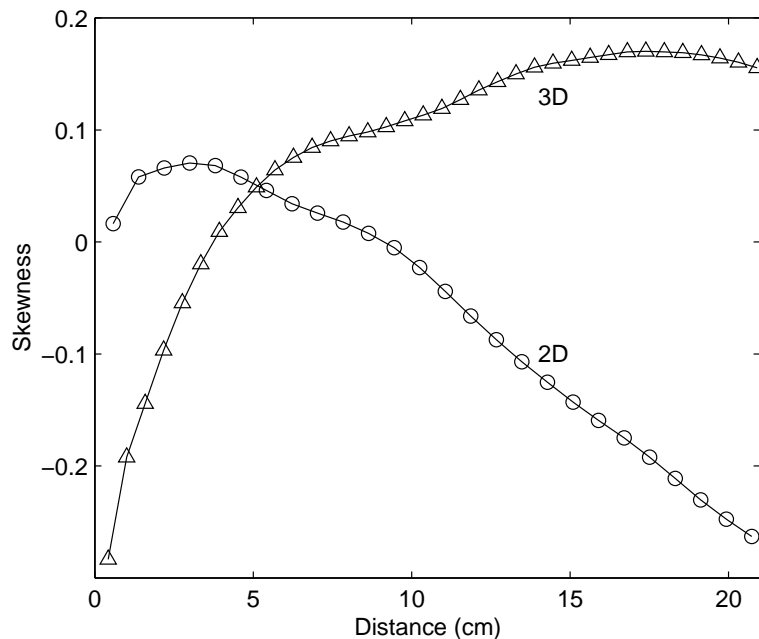


Figure 6.4: Skewness ($S_3/S_2^{2/3}$) of the velocity differences as a function of separation ℓ . In our experiments, effects of the strong shear lead to a change of the sign of S_3 in both the 2D and 3D cases.

In our fits, we measure the skewness (ξ) and we use $c\sqrt{\gamma\tau} = -\xi(q-1)/2$ in Eq. 6.5. This form of the dependence was found to produce excellent fits in the 2D case (see below), and very good fits in the 3D case at small separations. In the 3D case however, the quality of the fits was found to depend more strongly on the skewness than the 2D case. As the separations in the 3D case become larger than about 13 cm, the fits do not capture the large positive velocity increments. However, this approach has the advantage of keeping the number of free parameters to a minimum, instead of adding another parameter which would vary for different flows.

6.2.2 Probability Distribution Functions

Sample fits for the 2D data are shown on linear and log-lin axes in Fig. 6.5. The log-lin axes show the details of the tails of the distributions, while the linear axes show the details of the peaks. We see from these figures that both the tails and the peaks are fit quite well over the whole range of length scales in the inertial range. The data suffer from some noise, as seen in the tails of the distributions, and also near the peak of the 1.2 cm curve in Fig. 6.5, but the fit is largely insensitive to the noise.

The same curves for the 3D flow are shown in Fig. 6.6. Here, we find that we are still able to fit the PDFs, as they change shape from having exponential tails to a Gaussian shape. The fits for the small separation case are not as good as the ones shown in the 2D case; the peaks are not fit correctly, although the behavior in the tails of the distributions is well captured. However, the results are still reasonable for an analysis with only one fitting parameter.

6.2.3 Nonextensivity parameter

From the fits above, we can extract the value of q that provides the best fits for the PDFs as a function of separation distance ℓ . The distinction between the 2D and 3D flows can be seen in Fig. 6.7. Consistently with the results of Chapter 4, we see that the 2D PDFs preserve their shape and produce values of q that are relatively stable. These values are far from $q = 1$, which would correspond to Gaussian statistics; the parameter q can therefore be used as a measure of how far the statistics are from Gaussian. The 3D flows produce values of q that start around 1.25, indicating a large departure from Gaussianity, and then decrease until they reach the value for Gaussian flow at $q = 1$. These 3D results are similar to the results for a turbulent Couette-Taylor flow [8].

The physical significance of the nonextensivity parameter q is not solidly es-

tablished in the literature. It is believed to be related to the space filling of the vortices at a scale ℓ , where $q = 1$ indicates space-filling Kolmogorov-type flow [8]. Large departures from $q = 1$ indicate a flow that is highly intermittent at those scales. Therefore the values of q_{2D} for our 2D experiment are consistent with the small value of β_{2D} that we obtained in Chapter 4, indicating an intermittent flow at all the scales of the inertial range. As already argued in numerical simulations [79, 28], coherent vortices cause a strong departure from Gaussian statistics in a turbulent flow. In this chapter, we show actual experimental data which quantify this departure with one parameter.

In the case of the 3D flow, the value of β_{3D} is similar to β_{2D} . However, q_{3D} decays to one for large separations, consistent with our observation that the intermittent coherent structures are only present at small scales in the 3D case. It is common for 3D turbulence to display coherent vortices (and hence departures from Gaussianity) at small scales, but these coherent vortices do not grow since no inverse cascade is present. This behavior is captured by the trend in q , and a large difference between the value for large and small scales indicates a flow which is strongly scale-dependent.

The significance of these results has yet to be fully explored, since this is a relatively new field of research. However, there is mounting evidence that the Tsallis nonextensive statistical mechanics are applicable to a variety of nonequilibrium systems; The hope is that a common approach might allow one to understand problems that are different in their dynamics through a common statistical approach. We present results here as motivation for further theoretical and experimental work on the applicability of nonextensive, nonequilibrium statistical mechanics in turbulent flows.

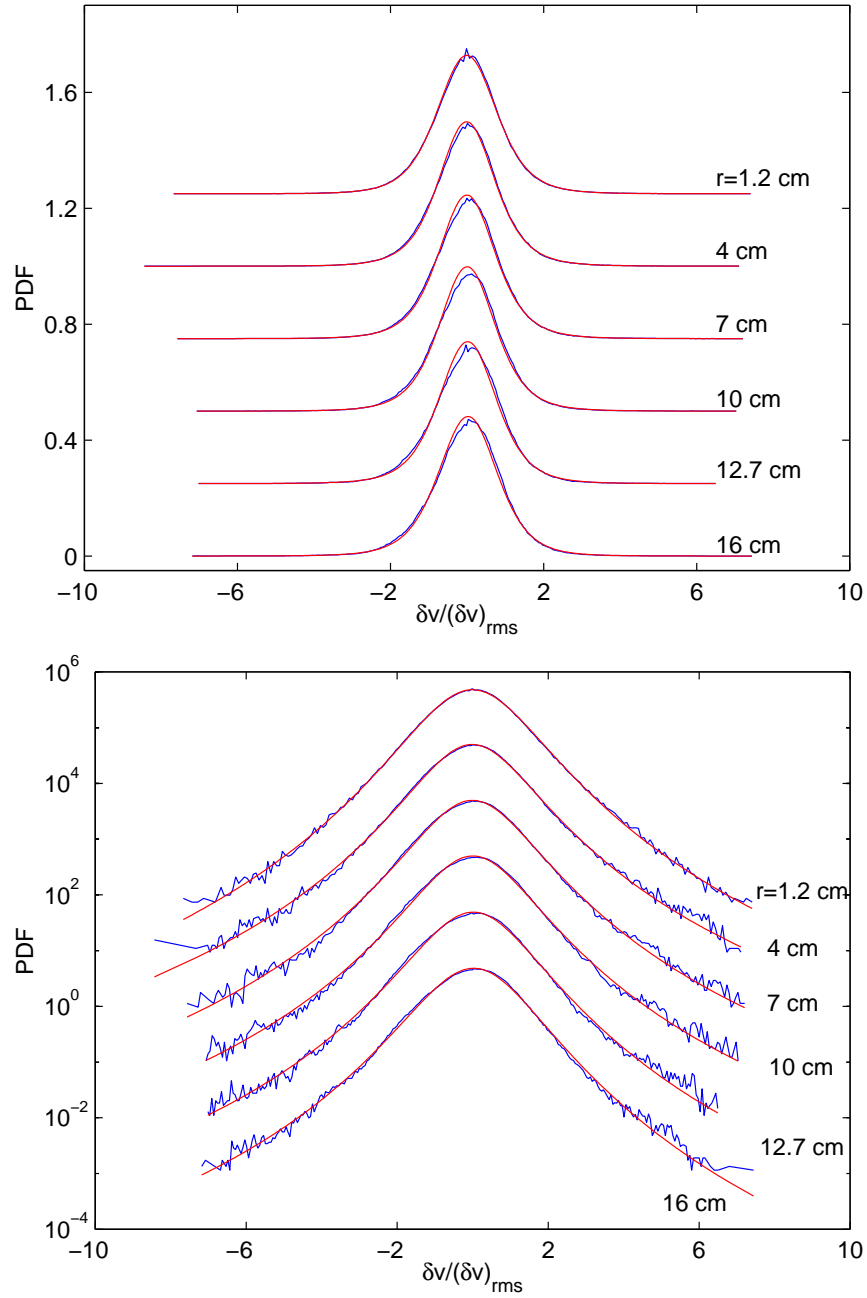


Figure 6.5: Fit for 2D (case I in Table 4.3 flow on linear axes (top) and log-linear axes (bottom), $\ell = 1.2$ cm to 16 cm, using $\alpha = 1 - (q - 1)^7$. See corresponding values of q in Fig. 6.7.

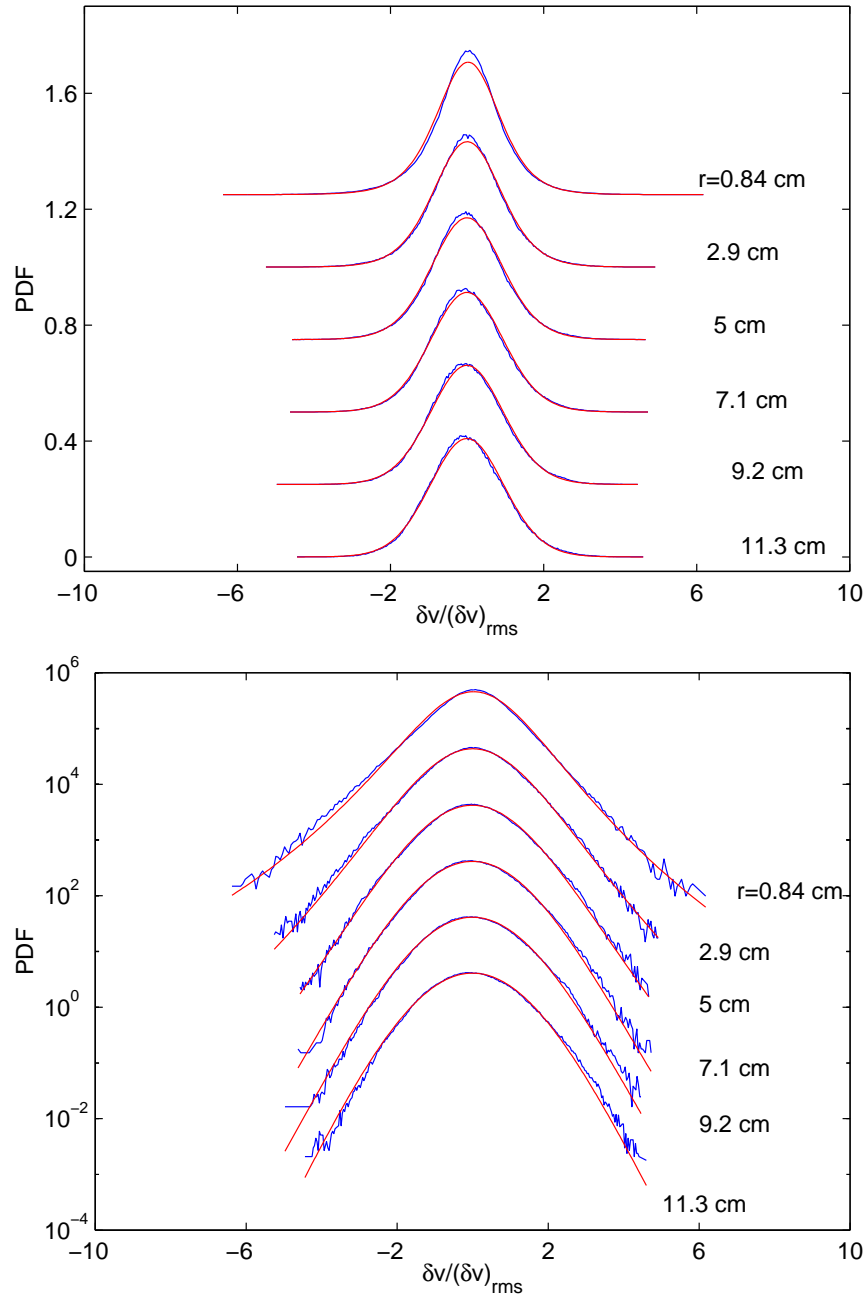


Figure 6.6: Fit for 3D (case IV in Table 4.3 flow on linear axes and log-linear, $\ell = 0.8$ cm to 11.3 cm.

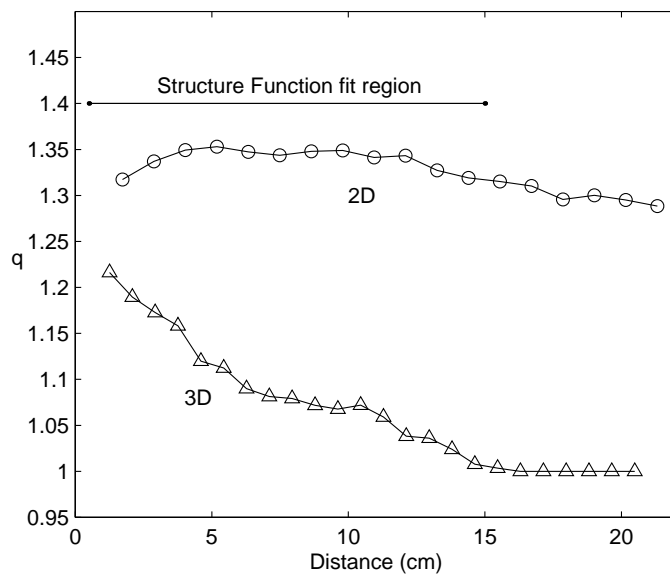


Figure 6.7: Nonextensivity parameter q as a function of separation ℓ . The 2D curve preserves the value of q while the 3D case is similar to other 3D experiments and approaches Gaussian statistics at large ℓ .

Chapter 7

Discussion



This thesis describes measurements made on the transition between two- and three-dimensional turbulence in a rotating system, as a function of the rotation rate. Below are some of the main contributions of this work, followed by some of the many interesting avenues that might be pursued in the future.

7.1 Contributions

In this thesis, The signature of the transition between 3D and 2D turbulence as a function of rotation rate was shown from different viewpoints. First through the shape of the velocity difference PDFs (Fig. 4.17); in the 3D case, the behavior was similar to other 3D flows, where the PDFs switch from having exponential tails at short separations to nearly Gaussian at large separations. In the 2D case, the PDFs preserve their shape at all the length scales explored here.

Next, the structure function relative (ESS) scaling gradually varied from the typical 3D behavior to a linear dependence on the order p , shown in Fig. 4.19. This behavior was not unexpected, since 2D turbulence was expected to be self-similar, and the scaling of 3D turbulence is well known. We have confirmed however that the statistics of rotating flows approach those for 2D turbulence as the rotation rate is increased. Furthermore, the ability to switch between the 2D and 3D flows is unique to this study and has not been shown in any previous experiments.

This switching was explored by using the tests of the Hierarchical Structure model. The model makes certain assumptions about the internal structure of the turbulent flow, and the relation between structures of different intensities. The β - and γ - tests were applied and confirm that the model is applicable to our flow.

The value of β remained fixed across all the flows explored in our tank (Fig 4.20), at a value significantly lower than those obtained for other turbulent flows. This indicates that our flows are more intermittent than the Couette-Taylor flow and free jets. In other words, the structures that cause the intermittent fluc-

tuations in the time series are more coherent in our flows than in other situations. This result was supported by the visualization of the experiment where coherent vortices were omnipresent over the whole parameter space.

The results of the γ test supported the observations of a gradual transition to a self-similar flow observed in the structure functions, as the rotation rate was increased (Fig 4.21). Moreover, the γ test showed that the mechanism that caused this transition was the generation of coherent/intermittent vortices at a wide range of scales in the cascade. In the 2D case, the width of the tails of the PDFs, corresponding to the rare events, changed in the same way as the typical width of the PDF, corresponding to the less intense, more common events.

This route to self-similarity is a new one. Previously, the only flows found to be self-similar were ones where large coherent vortices didn't exist at all. The 2D simulations and stratified experiments which reported self-similarity had near Gaussian statistics at all scales; flows that had non-Gaussian statistics at small scales invariably showed scale-dependence, such as soap films. In the present case, the statistics of the flow were found to be far from Gaussian at all scales in the inertial range, yet still led to self-similar flow when vortex stretching was excluded by rapid rotation. This is significant since flows occurring in Nature might display scale-invariance even when strong structures are present.

We also explored the high-rotation 2D flows in detail. The classical theory of 2D turbulence starts with the Navier-Stokes equations in two-dimensions and ignores the third dimension altogether. In physically realizable quasi-2D flows, the third dimension is always present though its effects are small. In rotating turbulent flows for instance, the equations to describe the flow are the full 3D Navier-Stokes equations with the addition a strong Coriolis force term. Therefore the exact scaling might well be different from the predictions for strictly 2D turbulence.

Indeed, we found in our case a turbulent flow where the energy scaled as

$E(k) \sim k^{-2}$, in contrast with standard Kolmogorov theory, and also different from the Kraichnan scaling predicted for 2D flows. This anomalous scaling was consistent with the scaling of the moments of the velocity difference (structure functions), which also scaled with a slope of $1/2$ ($\zeta_p = p/2$). This anomalous scaling is likely related to the strong shear that exists in the flow, and which causes the energy transfer between scales to be driven by both radial and longitudinal effects.

Similarly to previously reported shear flows, the shear seemed to increase the intermittency of the flow (the value of β was low). However, this was the first study of a shear flow where the statistics remained self-similar. Therefore the structure function exponents still scaled linearly with the order p , but the effect of the shear was to change the coefficient from $1/3$ to $1/2$. This was a completely unexpected result which will hopefully find theoretical validation as part of a more general theory of turbulent shear flows.

Finally, we motivated further theoretical work by measuring the nonextensivity parameter q of the Tsallis entropy. This work is related to the extension of standard statistical mechanics to the non-equilibrium realm, where the turbulence problem lives. We extend the theoretical work which describes turbulence in terms of nonextensive entropy and we find that our statistics are well represented by the Beck-Tsallis analysis. The significance of this result lies in the validation of a highly abstract concept in experimental measurements. The ability to relate the values of q to the existing theories of turbulence can be a very important contribution to the understanding of the implications of non-equilibrium statistical mechanics.

One goal of our study was to isolate certain effects in turbulent flows which contribute to the complexity of the problem. In this case, we attempted to isolate the effects of vortex stretching by switching from a fully 3D regime to a 2D flow with all other parameters fixed. Much was learned from this by testing existing theories of turbulence as they apply in the 3D and 2D regimes. A useful theory should apply

in both cases, and should capture the presence or lack of vortex stretching in a conclusive way. That is what we found in the scaling of the structure functions and from the β and γ tests. In the process, we learned about the effects of shear and the presence of coherent structures. By analyzing the data in different ways, we hope to gain even more insight on the nature of the transition from 3D to 2D, and about the dynamical changes as vortex stretching is added or removed.

7.2 Future work

Many questions are left unanswered by the work in this thesis. The technical aspects of building the apparatus and writing the analysis routines took up too much time. However, given the current state of the experiment (working) and of the analysis software, one can now use the system to further probe some of the following questions.

First, it would be very interesting to test the effect of the sloped bottom on the flow. Would we still obtain the anomalous scaling for a flat bottom? How about for the co-rotating jet, which has traditionally been viewed as being more orderly and less turbulent? The shear in the co-rotating jet is inherently different from that in the counter-rotating flow. Therefore, both the dynamics and the statistics of the flow might be different. Repeating our study in the co-rotating case should provide great insights on the problem.

The second question would be to test the effects of the forcing mechanism. We have found a change in behavior of the structure functions at 2 cm, or the separation of the holes in the forcing ring. While a connection between the length scales seems likely, it is also possible that the matching is purely coincidental. One can test for the relation would be to add a false bottom on the tank with slits rather than holes forcing the flow. This might change the flow significantly if indeed the separation between the individual forcing holes is important, which would also be

an interesting result.

A subject that we had approached but never really fully entered was the relation between our flows and plasma flows in tokamaks. Flows in a magnetically confined plasma can be modeled by the same equations of motion as fluid flows under rotation, within certain regimes. Recent numerical simulations [11] and experiments [72] show the existence of radial ejections in plasma flows which are very similar to our vortex ejections. The role of these vortices in the transport of passive tracers (heat or particles) is of major importance for fusion experiments. Our setup has the great advantage of visualization, compared with the plasma experiments where measurements are extremely difficult. Therefore an experiment like ours might contribute qualitative (if not quantitative) insights into the behavior of plasmas.

A related question that was also raised in the plasma community is whether shear flows can suppress turbulence in the context of geostrophy. Several extensive numerical and theoretical studies have been made on the effect of strong shear on the generation or suppression of turbulence (see review article by Terry [93]). Our experiment is uniquely positioned to study these questions with no modifications necessary. Here also, the effect of the beta plane and the asymmetry between the co-rotating and counter-rotating jets would be important to study.

The list of possible problems can be extended to include many more questions, but we will stop here.

Bibliography

- [1] R.J. Adrian. Particle-imaging techniques for experimental fluid mechanics. *Annual Review of Fluid Mechanics*, 23:261–304, 1991.
- [2] T. Arimitsu and N. Arimitsu. Tsallis statistics and fully developed turbulence. *J. Phys. A: Math. Gen.*, 33:L235–L241, 2000.
- [3] A. Arneodo, C. Baudet, F. Belin, B. Castaing, B. Chabaud, R. Chavariia, S. Ciliberto, R. Camussi, F. Chillà, B. Dubrulle, Y. Gagne, B. Hebral, J. Herweijer, M. Marchand, J. Maurer, J.F. Muzy, A. Naert, A. Noullez, J. Peinke, F. Roux, P. Tabeling, W. Vand de Water, and H. Willaime. Structure functions in turbulence, in various flow configurations, at reynolds number between 30 and 5000, using extended self-similarity. *Europhys. Lett.*, 34(6):411–416, May 1996.
- [4] P. Bartello, O. Métais, and M. Lesieur. Coherent structures in rotating three-dimensional turbulence. *J. Fluid Mech.*, 273:1–29, 1994.
- [5] G.K. Batchelor. *The theory of homogeneous turbulence*. Cambridge monographs on mechanics and applied mathematics. Cambridge University Press, 1953.
- [6] G.K. Batchelor. Computation of the energy spectrum in homogeneous two-

- dimensional turbulence. *High-Speed Computing in Fluid Dynamics*, pages 233–239, 1969.
- [7] C. Beck. Application of generalized thermostatics to fully developed turbulence. *Physica A*, 277:115–123, 2000.
- [8] C. Beck, G.S. Lewis, and H.L. Swinney. Measuring nonextensivity parameters in a turbulent Couette-Taylor flow. *Phys. Rev. E*, 63(3):035303/1–4, 2001.
- [9] R. Benzi, S. Ciliberto, R. Tripicciono, C. Baudet, F. Massaioli, and S. Succi. Extended self-similarity in turbulent flows. *Phys. Rev. E*, 48(1):R29–R32, July 1993.
- [10] D. Bernard. Three point velocity correlation functions in two-dimensional forced turbulence. *Phys. Rev. E*, 60(5):6184–6187, Nov. 1999.
- [11] P. Beyer, S. Benkadda, X. Garbet, and P.H. Diamond. Non-diffusive transport in tokamaks: Three dimensional structure of bursts and role of zonal flows. *preprint*, 2000.
- [12] G. Boffetta, A. Celani, and M. Vergassola. Inverse energy cascade in two-dimensional turbulence: Deviations from Gaussian behavior. *Phys. Rev. E*, 61(1):R29–R32, Jan 2000.
- [13] O.N. Boratav and R.B. Pelz. Structures and structure functions in the inertial range of turbulence. *Phys. Fluids*, 9:1400–1415, 1997.
- [14] J.M. Burgess, C. Bizon, W.D. McCormick, J.B. Swift, and H.L. Swinney. Instability of the kolmogorov flow in a soap film. *Phys. Rev. E*, 60:715–721, 1999.
- [15] C. Cambon, N. N. Mansour, and F. S. Godeferd. Energy transfer in rotating turbulence. *J. Fluid Mech.*, 337:303–332, 1997.

- [16] V.M. Canuto and M.S. Dubovikov. A dynamical model for turbulence. I. general formalism. *Phys. Fluids*, 8(2):571–586, February 1996.
- [17] V.M. Canuto and M.S. Dubovikov. A dynamical model for turbulence. V. the effect of rotation. *Phys. Fluids*, 9(7):2132–2140, July 1997.
- [18] V.M. Canuto and M.S. Dubovikov. Physical regimes and dimensional structure of rotating turbulence. *Phys. Rev. Lett.*, 78(4):666, Jan 1997.
- [19] V.M. Canuto and M.S. Dubovikov. Response to “some remarks concerning recent work on rotating turbulence.” *Phys. Fluids*, 10(12):3245–3246, 1998.
- [20] G.F. Carnevale, J.C. McWilliams, Y. Pomeau, J.B. Weiss, and W.R. Young. Evolution of vortex statistics in two-dimensional turbulence. *Phys. Rev. Lett.*, 66(21):2735–2737, May 1991.
- [21] K. T. Christensen and R. J. Adrian. Statistical evidence of hairpin vortex packets in wall turbulence. *J. Fluid Mech.*, 431:433–443, March 2001.
- [22] H.J.H. Clercx and G.J.F. Van Heijst. Energy spectra for decaying 2d turbulence in a bounded domain. *Phys. Rev. Lett.*, 85(2):306–309, July 2000.
- [23] A. Colin De Verdière. Quasi-geostrophic turbulence in a rotating homogeneous fluid. *Geophys. Astrophys. Fluid Dynamics*, 15:213–251, 1980.
- [24] Y Couder, J.M. Chomaz, and M. Rabaud. On the hydrodynamics of soap films. *Physica*, 37 D:384–405, July 1989.
- [25] W. B. Daniel and M.A. Rutgers. Intermittency in forced two-dimensional turbulence. *preprint*, 2000.
- [26] S.C. Dickinson and R.L. Long. Oscillating grid turbulence including effects of rotation. *J. Fluid Mech.*, 126:315–333, 1983.

- [27] S. Douady, Y Couder, and M. E. Brachet. Direct observation of the intermittency of intense vorticity filaments in turbulence. *Phys. Rev. Lett.*, 67:983–986, 1991.
- [28] M. Farge, K Schneider, and N. Kevlahan. Non-gaussianity and coherent vortex simulation for two-dimensional turbulence using an adaptive orthogonal wavelet basis. *Phys. Fluids*, 11(8):2187–2201, 1999.
- [29] A. Fincham and G. Delerce. Advanced optimization of correlation imaging velocimetry algorithms. *proceedings of PIV99*, 1999.
- [30] A. Fincham, T. Maxworthy, and G.R. Spedding. Energy dissipation and vortex structure in freely decaying, stratified grid turbulence. *Dynamics of atmospheres and oceans*, 23:155–169, 1996.
- [31] A. Fincham and G.R. Spedding. Low cost, high resolution DPIV for measurement of turbulent fluid flow. *Exp. Fluids*, 23(6):449–462, 1997.
- [32] R. Fjortoft. On the changes in the spectral distribution of kinetic energy for two dimensional, non-divergent flow. *Tellus*, 5:225–230, 1953.
- [33] U. Frisch. *Turbulence, the legacy of A.N. Kolmogorov*. Cambridge University Press, 1995.
- [34] M. Ghil and S. Childress. *Topics in geophysical fluid dynamics: Atmospheric dynamics, dynamo theory, and climate dynamics*, volume 60 of *Applied mathematical sciences*. Springer-Verlag, 1987.
- [35] Andrew Gilbert. A cascade interpretation of Lundgren’s stretched spiral vortex model for turbulent fine structure. *Phys. Fluids A*, 5(11):2831–2834, November 1993.

- [36] Andrew D. Gilbert. Spiral structures and spectra in two-dimensional turbulence. *J. Fluid Mech.*, 193:475–497, 1988.
- [37] F.S. Godeferd and L. Lollini. Direct numerical simulations of turbulence with confinement and rotation. *J. Fluid Mech.*, 393:257–308, 1999.
- [38] H.P. Greenspan. *The theory of rotating fluids*. Cambridge monographs on mechanics and applied mathematics. Cambridge U.P., London, 1968.
- [39] E.J. Hopfinger. Turbulence and vortices in rotating fluids. In P. Germain, M. Piau, and D. Caillerie, editors, *17th International Congress on Theoretical and Applied Mechanics*, pages 117–138, Grenoble (France), 1989. IUTAM, Elsevier Science Publishers B.V.
- [40] E.J. Hopfinger and F.K. Browand. Vortex solitary waves in a rotating, turbulent flow. *Nature*, 295:393–395, February 1982.
- [41] E.J. Hopfinger, F.K. Browand, and Y. Gagne. Turbulence and waves in a rotating tank. *J. Fluid. Mech.*, 125:505–534, 1982.
- [42] E.J. Hopfinger and J.-A. Toly. Spatially decaying turbulence and its relation to mixing across density interfaces. *J. Fluid Mech.*, 78:155–175, 1976.
- [43] Murshed Hossain. Reduction in the dimensionality of turbulence due to a strong rotation. *Phys. Fluids*, 6(3):1077–1079, March 1994.
- [44] A. Ibbetson and D. Tritton. Decay of turbulence in a rotating fluid. *J Fluid Mech*, 67:639–671, 1975.
- [45] L. Jacquin. *Etude theorique et experimentale de la turbulence homogène en rotation*. PhD thesis, Université Claude Bernard, Lyon, France, 1989.
- [46] L. Jacquin, O. Leuchter, C. Cambon, and J. Mathieu. Homogeneous turbulence in the presence of rotation. *J. Fluid. Mech.*, 220:1–52, November 1990.

- [47] N. K.-R. Kevlahan and M. Farge. Vorticity filaments in two-dimensional turbulence: creation, stability and effect. *J. Fluid Mech.*, 346:49–76, 1997.
- [48] C. Kittel and H. Kroemer. *Thermal physics*. Freeman, second edition, 1980.
- [49] R.H. Kraichnan. Inertial ranges in two-dimensional turbulence. *Phys. Fluids*, 10(7):1417–1423, July 1967.
- [50] Kurien, S. and Sreenivasan, K.R. Anisotropic scaling contributions to high-order structure functions in high-reynolds-number turbulence. *Phys. Rev. E*, 62:2206–2212, 2000.
- [51] J-P. Laval, B. Dubrulle, and S. Nazarenko. Nonlocality of interaction of scales in the dynamics of 2D incompressible fluids. *Phys. Rev. Lett.*, 83(20):4061–4064, 1999.
- [52] J-P. Laval, B. Dubrulle, and S. Nazarenko. Nonlocality and intermittency in three-dimensional turbulence. *Phys. Fluids*, 13(13):1995–2012, July 2001.
- [53] M. Lesieur. *Turbulence in Fluids*. Fluid mechanics and its applications. Kluwer Academic Publishers, third edition, 1997.
- [54] G.S. Lewis and H.L. Swinney. Velocity structure functions, scaling, and transitions in high-reynolds-number couette-taylor flow. *Phys. Rev. E*, 59(5):5457–5467, May 1999.
- [55] P.A. Libby. *Introduction to turbulence*. Combustion: An international series. Taylor and Francis, Washington, D.C., 1996.
- [56] L. Liu and Z.-S. She. *Phys. Rev. E*, preprint.
- [57] T.S. Lundgren. A small-scale turbulence model. *Phys. Fluids A*, 5(6):1472–1483, 1993.

- [58] P. S. Marcus. Vortex dynamics in a shearing zonal flow. *J. Fluid Mech.*, 215:393–430, 1990.
- [59] A.D. McEwan. Angular momentum diffusion and the initiation of cyclones. *Nature*, page 126, 1976.
- [60] J.C. McWilliams. The emergence of isolated coherent vortices in turbulent flow. *J. Fluid Mech.*, 146:21–43, 1984.
- [61] J.C. McWilliams, J.B. Weiss, and I. Yavneh. The vortices of homogeneous geostrophic turbulence. *J. Fluid Mech.*, 401:1–26, 1999.
- [62] R. Mei. Velocity fidelity of flow tracer particles. *Experiments in Fluids*, 22(1):1, 1996.
- [63] R.S. Mendes and C. Tsallis. Renormalization group approach to nonextensive statistical mechanics. *Phys. Lett. A*, 285:273–278, 2001.
- [64] S.D. Meyers. *Laboratory Studies of Coherent Structures in Quasi-Geostrophic Flows*. PhD thesis, University of Texas, Austin, 1991.
- [65] A.S. Monin and A.M. Yaglom. *Statistical fluid mechanics*, volume II. MIT press, 1975.
- [66] M. Nelkin. Universality and scaling in fully developed turbulence. *Advances in Physics*, 43(2):143–181, 1994.
- [67] R. Panton. *Incompressible flow*. Wiley-Interscience, second edition, 1996.
- [68] J Paret, M.C. Jullien, and P. Tabeling. Vorticity statistics in the two-dimensional enstrophy cascade. *Phys. Rev. Lett.*, 83(17):3418–3421, October 1999.

- [69] J. Paret and P. Tabeling. Experimental observation of the two-dimensional inverse energy cascade. *Phys. Rev. Lett.*, 79(21):4162–4165, 1997.
- [70] J. Paret and P. Tabeling. Intermittency in the two-dimensional inverse cascade of energy: Experimental observations. *Phys. Fluids*, 10(12):3126–3136, December 1998.
- [71] J. Pedlosky. *Geophysical fluid dynamics*. Springer Verlag, New York, 1979.
- [72] P.A. Politzer. Observation of avalanchelike phenomena in a magnetically confined plasma. *Phys. Rev. Lett.*, 84(6):1192–1195, 2000.
- [73] M. Raffel, C. Willert, and J. Kompenhans. *Particle Image Velocimetry: a practical guide*. Experimental Fluid Mechanics. Springer, 1998.
- [74] P.B. Rhines. Geostrophic turbulence and geophysical circulations. In Robert L. Dewar and Ross W. Griffiths, editors, *Two-dimensional turbulence in plasmas and fluids*, pages 91–112, Canberra, Australia, 1997. AIP.
- [75] Maarten A. Rutgers. Forced 2D turbulence: Experimental evidence of simultaneous inverse energy and forward enstrophy cascades. *Phys. Rev. Lett.*, 81(11):2244, September 1998.
- [76] P.G. Saffman. On the spectrum and decay of random two-dimensional vorticity distributions at large Reynolds number. *Studies in Applied Mathematics*, L(4):377–383, December 1971.
- [77] P. Santangelo, R. Benzi, and B. Legras. The generation of vortices in high-resolution, two-dimensional decaying turbulence and the influence of initial conditions on the breaking of self-similarity. *Phys. Fluids A*, 6:1027–1034, 1989.

- [78] K.W. Schwarz. Evidence for organized small-scale structure in fully developed turbulence. *Phys. Rev. Lett.*, 64(4):415–418, 1990.
- [79] Z.-S. She, E. Jackson, and S.A. Orszag. Structure and dynamics of homogeneous turbulence: models and simulations. *Proc. Roy. Soc. London A*, 434:101, 1991.
- [80] Z.-S. She and E. Lévêque. Universal scaling laws in fully developed turbulence. *Phys. Rev. Lett.*, 72:336–339, 1994.
- [81] Z.-S. She, K. Ren, G.S. Lewis, and H.L. Swinney. Scalings and structures in turbulent Couette-Taylor flow. *Phys. Rev. E*, 64:016308/1–7, July 2001.
- [82] T.G. Shepherd. Rossby waves and two-dimensional turbulence in a large-scale zonal jet. *J. Fluid Mech.*, 183:467–509, 1987.
- [83] E.D. Siggia and H Aref. Point-vortex simulation of the inverse energy cascade in two-dimensional turbulence. *Phys. Fluids*, 24(1):171–173, January 1981.
- [84] L.M. Smith, J. Chasnov, and F. Waleffe. Crossover from two- to three-dimensional turbulence. *Phys. Rev. Lett.*, 77(12):2467–2470, September 1996.
- [85] L.M. Smith and F. Waleffe. Transfer of energy to two-dimensional large scales in forced, rotating three-dimensional turbulence. *Phys. Fluids*, 11(6):1608–1622, June 1999.
- [86] L.M. Smith and V. Yakhot. Bose condensation and small-scale structure generation in a random force driven 2D turbulence. *Phys. Rev. Lett.*, 71(3):352–355, July 1993.
- [87] L.M. Smith and V. Yakhot. Onset of intermittency in two-dimensional decaying turbulence. *Phys. Rev. E*, 55(5):5458–5464, May 1997.

- [88] J. Somméria. Experimental study of the two-dimensional inverse energy cascade in a square box. *J. Fluid Mech.*, 170:139–168, 1986.
- [89] J. Somméria, S.D. Meyers, and H.L. Swinney. Experiments on vortices and rossby waves in eastward and westward jets. In A. Osborne, editor, *Nonlinear Topics in Ocean Physics*, pages 227–269, 1988.
- [90] J. Sommeria, S.D. Meyers, and H.L. Swinney. Laboratory simulation of jupiter’s great red spot. *Nature*, 331(6158):689–693, February 1988.
- [91] K.R. Sreenivasan. On the universality of the kolmogorov constant. *Phys. Fluids*, 7:2778–2784, 1995.
- [92] K.R. Sreenivasan and B. Dhruva. Is there scaling at high-reynolds-number turbulence? In Michio Yamada, editor, *Progress of Theoretical Physics Supplement No 130*, pages 103–120. AIP, 1998.
- [93] P.W. Terry. Suppression of turbulence and transport by sheared flow. *Reviews of Modern Physics*, 72(1):109–165, 2000.
- [94] F. Toschi, E. Lévêque, and G. Ruiz-Chavarria. Shear effects in nonhomogeneous turbulence. *Phys. Rev. Lett.*, 85:1436–1439, 2000.
- [95] D.J. Tritton. Experiments on turbulence in geophysical fluid dynamics. I. - turbulence in rotating fluid. In *Turbulence and Predictability in Geophysical Fluid Dynamics and Climate Dynamics*, pages 172–192. Soc. Italiana di Fisica, 1985.
- [96] D.J. Tritton. *Physical Fluid Dynamics*. Oxford Science Publications, second edition, 1993.
- [97] S.M. Trujillo. *An investigation of the effects of spanwise wall oscillation on*

the structure of a turbulent boundary layer. PhD thesis, University of Texas at Austin, 1999.

- [98] C. Tsallis. <http://tsallis.cat.cbpf.br/biblio.htm>.
- [99] C. Tsallis. Possible generalization of boltzmann-gibbs statistics. *J. Stat. Phys.*, 52:479, 1988.
- [100] P. Vorobieff, M. Rivera, and R.E. Ecke. Soap film flows: Statistics of two-dimensional turbulence. *Phys. Fluids*, 11(8):2167–2177, August 1999.
- [101] Eric R. Weeks. *Experimental Studies of Anomalous Diffusion, Blocking Phenomena, and Two Dimensional Turbulence*. PhD thesis, University of Texas, Austin, 1997.
- [102] J. Westerweel. Fundamentals of digital particle image velocimetry. *Meas. Sci. Technol.*, 8:1379–1392, 1997.
- [103] J. Westerweel, D. Dabiri, and M. Gharib. The effect of a discrete window offset on the accuracy of cross-correlation analysis of digital PIV recordings. *Exp. Fluids*, 23(1):20–28, 1997.
- [104] P.K. Yeung and Ye Zhou. Numerical study of rotating turbulence with external forcing. *Phys. Fluids*, 10(11):2895–2909, 1998.
- [105] Ye Zhou. A phenomenological treatment of rotating turbulence. *Phys. Fluids*, 7(8):2092–2094, August 1995.
- [106] Ye Zhou, C.G. Speziale, and R. Rubinstein. Some remarks concerning recent work on rotating turbulence. *Phys. Fluids*, pages 3242–3244, 1998.

Vita

Charles Baroud was born in Lebanon on November 23rd 1972, to Marie and Naim Baroud. He dropped out of high school from Champville in 1989, due to the events in Lebanon at the time. He *did* however graduate with a Bachelor of Science from the Massachusetts Institute of Technology in January 1994, with a degree combining physics and mechanical engineering. In 1994-1995, he worked at Sun Microsystems, and joined the graduate school at the University of Texas in Sept. 1995. He received a Masters of Science in Mechanical Engineering in 1997 with a thesis on smart hydrodynamic bearings.

Permanent Address: Charles Baroud

Center for Nonlinear Dynamics
University of Texas at Austin,
Austin, TX 78712

This dissertation was typeset with $\text{\LaTeX} 2_{\epsilon}$ ¹ by the author.

¹ $\text{\LaTeX} 2_{\epsilon}$ is an extension of \LaTeX . \LaTeX is a collection of macros for \TeX . \TeX is a trademark of the American Mathematical Society. The macros used in formatting this dissertation were written by Dinesh Das, Department of Computer Sciences, The University of Texas at Austin.